LINEAR AND NONLINEAR OPTICS IN A SYSTEM OF MASSLESS DIRAC FERMIONS

A Dissertation

by

XIANGHAN YAO

Submitted to the Office of Graduate and Professional Studies of
Texas A&M University
in partial fulfillment of the requirements for the degree of

DOCTOR OF PHILOSOPHY

Chair of Committee,	Alexey Belyanin
Committee Members,	Artem G. Abanov
	Raytcho Lazarov
	Joseph H. Ross
Head of Department,	George R. Welch

August 2014

Major Subject: Physics

ABSTRACT

Graphene electrons possess linear energy dispersion relation, and thus behave as two-dimensional (2D) Dirac fermions. Consequently, compared with the conventional 2D electron gas systems (2DEG) found in MOSFETs and quantum wells, graphene exhibits a variety of electronic and optoelectronic properties that are characteristic of 2D Dirac fermions. Similar 2D Dirac fermions are found at the surface layer of 3D topological insulator, and they are topological protected from backscattering due to spin-orbital coupling and time reversal symmetry.

We here calculate the linear and nonlinear optical response of graphene in strong magnetic and optical fields, using a quantum-mechanical density-matrix formalism. We show that graphene in a magnetic field possesses a giant mid- or far-infrared optical nonlinearity, perhaps the highest among known materials. The high nonlinearity originates from the unique electronic properties and selection rules near the Dirac point. As a result, even one monolayer of graphene gives rise to an appreciable nonlinear frequency conversion efficiency for incident infrared radiation.

Inspired by the highly efficient four-wave mixing process in the 2D Dirac fermion systems, we further propose a new mechanism of generating polarization-entangled photons based on the parametric generation process in the third section of this dissertation. Unique properties of quantized electron states in a magnetized graphene and optical selection rules near the Dirac point give rise to a giant optical nonlinearity and a high rate of photon production in the mid- or far-infrared range. A similar mechanism of photon entanglement may exist in topological insulators where the surface states have a Dirac-cone dispersion and demonstrate similar properties of magneto-optical absorption.

In the absence of a magnetic field, the surface plasmon resonance provides an alternative method to enhance nonlinear frequency conversion efficiency. In the forth section of this dissertation, a graphene-based difference frequency generation (DFG) of terahertz plasmons is proposed as an example to study nonlinear photon-plasmon interaction in 2D Dirac fermion systems. Our results demonstrate strong enhancement of the DFG efficiency near the plasmon resonance and the feasibility of phase-matched nonlinear generation of plasmons over a broad range of frequencies. Considering graphene plasmonics' superiorities in wave confinement, dissipation and tunability, a graphene-based nonlinear terahertz plasmon generation process promises applications in terahertz sources and sensors, as well as integrated photonic circuits.

DEDICATION

To my parents, Aping Wang and Duoquan Yao, and to my dear grandfather, Ziqiang Wang.

ACKNOWLEDGEMENTS

I would like to thank my committee chair, Dr. Alexey Belyanin, and my committee members, Dr. Artem Abanov, Dr. Raytcho Lazarov, and Dr. Joseph Ross, for their guidance and support throughout the course of my research. I also would like to thank Dr. Daren Cline for attending my dissertation defense.

I would like to express my sincere gratitude to my advisor, Dr. Alexey Belyanin, for his continuous support of my Ph.D study and research, for his patience, motivation, enthusiasm, and immense knowledge. He gave me the best guidance I ever had in my physics research as well as my career development.

Thanks also go to our collaboration from Dr. Mikhail Tokman in Russian Academy of Sciences, for his great ideas and the insightful discussions in the research projects about quantum entanglement generation, graphene plasmonics and polarization optics of topological insulators. I also would like to thank Mr. Fuxiang Li and Mr. Jianpin Liu, for the valuable discussions on Dirac fermions and topological insulators.

At last, I want to say thank you to my girlfriend Wenjie Zhao, who makes my life in Texas A&M University full of happiness. Thanks also go to my colleagues, my friends, and the department faculties and staffs for making the past four years an enjoyable experience of mine.

NOMENCLATURE

TI	Topological Insulator
DLG	Double Layer Graphene
2D	Two-dimensional
3D	Three-dimensional
2DEG	Two-dimensional Electron Gas
MOSFET	Metal-oxide-semiconductor Field-effect Transistor
DFG	Difference-frequency Generation
SPDC	Spontaneous Parametric Down-conversion

TABLE OF CONTENTS

Page

ABSTRACT ii

DEDICATION iv

ACKNOWLEDGEMENTS v

NOMENCLATURE vi

TABLE OF CONTENTS vii

LIST OF FIGURES ix

1. INTRODUCTION AND BACKGROUND 1

   1.1 Band structure of monolayer graphene 3
   1.2 Surface state of topological insulators 7
   1.3 Landau levels of 2D Dirac fermion systems 11
   1.4 Surface plasmon mode in 2D Dirac fermion systems 15

2. LINEAR AND NONLINEAR OPTICS OF MONOLAYER GRAPHENE . 23

   2.1 Density matrix formalism in Schrödinger picture 24
   2.2 Linear optical response 28
   2.3 Nonlinear optical response 34

3. GENERATION OF ENTANGLED PHOTONS IN GRAPHENE 48

   3.1 Heisenberg density operator 49
   3.2 Equations for the field operators 53
   3.3 Parametric generation of entangled photons 56

4. DIFFERENCE FREQUENCY GENERATION OF TERAHERTZ SURFACE PLASMONS 67

   4.1 Surface plasmon resonance in 2D Dirac fermion systems 68
   4.2 Difference frequency generation (DFG) process 73
   4.3 DFG in graphene/silicon-heterostructure waveguide 79
   4.4 DFG in double layer graphene and topological insulator 84

5. OPTICAL RESPONSE OF TOPOLOGICAL INSULATORS 87

   5.1 Linear optical response 89
   5.2 Polarization optics of topological insulators 95

5.3 Nonlinear optical properties 105
6. SUMMARY 110
REFERENCES 112

LIST OF FIGURES

FIGURE Page

1.1 Left: lattice structure of graphene. a_1 and a_2 are the lattice unit vectors, and δ_1, δ_2 and δ_3 are the nearest-neighbor vectors. Right: the corresponding Brillouin zone. (Figure from Castro Neto et al., *Rev. Mod. Phys.*, Vol.81, No.1, Jan.-Mar. 2009) 3

1.2 Electronic dispersion in the honeycomb lattice. Left: energy spectrum for finite values of t and t', with t = 2.7 eV and t' = -0.2 t. Right: zoom in of the energy bands close to one of the Dirac points. The Fermi level lies at the center. (Figure from Castro Neto et al., *Rev. Mod. Phys.*, Vol.81, No.1, Jan.-Mar. 2009) 5

1.3 In an external magnetic field perpendicular to the plane of graphene, the continuous energy bands near the Dirac point split into discrete Landau levels. (figure attached from A. J. Leggett's lecture notes.) . . 12

1.4 Dispersion curve of a surface plasmon mode in monolayer graphene for Fermi level $E_F = 50$ meV. The dielectric constant $\epsilon_2 = 4$ corresponds to SiO_2 in the THz region. Shaded area is the Landau damping region. 19

1.5 Dispersion curves for symmetric (ω_+) and antisymmetric (ω_-) plasmon modes in a thin TI film forming a double layer with a spacer thickness $d = 10, 20$ nm; $E_F = 100$ meV. Electric field of the symmetric plasmon mode is shown in the inset. The value of $\epsilon_2 = 10$ typical for semiconductors was assumed. Shaded area is the Landau damping region. 21

2.1 Allowed inter-LL transitions in graphene, $\hat{e}_{LHS}$ photon is absorbed for $|n| \to |n| + 1$, while $\hat{e}_{RHS}$ photon is absorbed when $|n| \to |n| - 1$. . . 31

2.2 Landau levels near the Dirac point superimposed on the electron dispersion without the magnetic field $E = \pm v_F|p|$. (b): A scheme of the four-wave mixing process in the four-level system of Landau levels with energy quantum numbers $n = -1, 0, +1, +2$ that are renamed to states 1 through 4 for convenience. 35

2.3 Transition frequencies in the 4-level graphene system shown in Fig. 1(b). ω_{mn} indicates the transition frequency between levels m and n. . . . 37

2.4 Contour plot of $f(x, y)$ as a function of normalized pump fields x and y. 41

2.5 (a) Intensity of the 4-wave mixing signal as a function of the intensity of the pump field E_2 normalized by $I_0 = c|E_{\rm sat}|^2/8\pi \simeq 2.2 \times 10^5$ W/cm^2. The value of I_0 is the saturation intensity of the transition 1-2 calculated at $B = 1$ T and assuming that $1/T = \gamma = 3 \times 10^{13}$ s^{-1}. I_1 is set to satisfy $y = 0.6x$. (b) Enlargement of (a) near the origin, which shows the intensity of the 4-wave mixing signal for a weak pump field. 43

2.6 Raman Stokes scattering of the incident field E_1 into the signal E_3. . 44

2.7 (a) Population differences as functions of the normalized pump field. (b) Gain $g\Delta z$ for one monolayer of graphene as a function of the normalized pump field in the magnetic field $B = 1$ T. Solid line: the total gain, dashed line: only the Raman part assuming $n_{43} = 0$. . . . 46

3.1 Geometry of the proposed experiment. Two pump fields at frequencies ω_{HF} and ω_{LF} normally incident on a sheet of graphene placed in a magnetic field B generate entangled photons with opposite sense of the circular polarization. 56

3.2 Energy levels and optical transitions involved in resonant parametric generation of entangled photons in graphene. Left: Landau levels near the Dirac point superimposed on the linear electron dispersion without the magnetic field. Right: A scheme of the entangled photon generation process in the four-level system of LLs with energy quantum numbers n = -2, -1, 0, 1 that were renamed as states 1,2,3, and 4 for convenience of notation. Right-hand side (RHS) or left-hand side (LHS) circular polarization of light indicated on the figure corresponds to the allowed transitions. 57

3.3 Parametric gain τ per monolayer of graphene as a function of normalized detuning of the signal fields $\Delta/\langle\gamma\rangle$ for the pump field intensity $|\Omega_p| = 0.1\langle\gamma\rangle$. 64

3.4 Parametric gain τ per monolayer of graphene as a function of normalized strength of the pump field $|\Omega_p|/\langle\gamma\rangle$ for the detuning $\Delta = 10\langle\gamma\rangle$. 65

4.1 Interband transition and intraband transition in doped monolayer graphene. 69

4.2 (a): Geometry of the DFG process. Two pump fields at frequencies ω_a and ω_b incident at angles θ_a and θ_b on graphene/TI placed on a substrate generate a highly confined surface plasmon field E_{pl} at their difference frequency and in-plane wave vector $q = q_b - q_a$. (b): Elementary three-wave-mixing processes involving two photons and a plasmon coupled to interband and intraband transitions, respectively. Grey shading indicates filled electron states. 73

4.3 Magnitude of the 2D $\chi^{(2)}_{xxx}$ as a function of Fermi energy for a fixed incidence angle $\theta_a = \theta_b = \theta = 60°$ and fixed sum of the incident pump frequencies $\omega_a + \omega_b = 400$ meV. Red line is the generated plasmon frequency which satisfies the phase-matching condition and energy conservation at each E_f. 77

4.4 The DFG efficiency $\eta = \frac{I_{pl}}{I_a I_b}$ and incidence angle θ as a function of the plasmon frequency under the conditions of frequency and phase matching. The sum of the incident pump frequencies is fixed to $\omega_a + \omega_b = 400$ meV. 79

4.5 (a) Integrated waveguide geometry of DFG of surface plasmons by counter-propagating TM modes. Profiles of B_y and E_x field components are indicated in blue dashed and red lines, respectively. (b) The relation of in-plane momentum and wavelength of the fundamental mode in $1\mu m$-thick graphene/Si waveguide. 80

4.6 $D(\omega, q)$ for the difference frequency signal, with two given fundamental mode in the Mid-IR range, we set Fermi energy 50meV here. 82

4.7 Difference frequency generation efficiency for two given fundamental mode in the same wavelength range$(5 - 6\mu m)$. We can easily observe the peak on the plasmon resonance points. 83

4.8 (a) Phase-matched plasmon frequency vs. wavelength of the fundamental TM mode for one of the pump fields in a 1-μm thick Si waveguide, for two values of Fermi energy. (b) DFG efficiency of surface plasmons for $E_F = 50$ meV and two values of the relaxation rate. . . 84

4.9 Fix one pump field at $1.55\mu m$, the difference frequency generation efficiency is a function of the tunable pump field, which reaches the peak value at plasmon resonance point. The peak efficiency scales as $1/\gamma^2$. Here Fermi energy in graphene is set as $50meV$. 85

5.1 (a) Energy bands of the surface states near the Γ point at zero magnetic field (with 2nd order correction shown by dashed line), and energies of Landau levels in a magnetic field of 10 T (horizontal lines). (b) Landau level energies as a function of the magnetic field for Bi_2Se_3. . 88

5.2 1T magnetic field, half-filled surface LL n=-1. (a) absorption coefficient. The upper half is $\hat{e}_{RHS}$ photon absorbance, and the other half corresponds to $\hat{e}_{LHS}$ photon absorbance; (b) Faraday rotation angle. Here γ is chosen as $10^{12}s^{-1}$. 94

5.3 (a)A proposed experiment geometry: the incident field is linearly polarized with orientation angle $\frac{\pi}{4}$. (b)The corresponding inter-surface-Landau-level transition scheme for incident frequency $\omega \approx \omega_c$. Here Fermi level is placed between surface Landau levels -1 and 0, so photons are coupled with inter-surface-Landau-level transition $-1 \to 0$. (c)Polarization coefficient(K) of the transmitted optical field, as a function of ξ. The slab thickness is chosen as 0.01λ in the plot. 98

5.4 (a)Multiple reflections between the double-layer geometry(e.g. topological insulator slab, double-layer TI thin-film). (b)The real and imaginary part of the polarization coefficient (K) of the transmitted optical field as a function of topological insulator slab thickness d. (c)Transmittance T as a function of slab thickness d, the dashed line is for a pure dielectric slab. Here $\xi = 4$ in both plots. 101

5.5 Polarization ellipse of the transmitted field. First row: from left to right, $\xi = 0.1, 1, 2, 3, 4$; d is fixed at 0.01λ. Second row: from left to right, $d = 0.1\lambda, 0.2\lambda, 0.3\lambda, 0.4\lambda, 0.5\lambda$; ξ is fixed at 4. 103

5.6 Orientation angle θ and phase-difference δ between E_y^t and E_x^t. 104

5.7 four wave mixing and stimulated raman scattering. 106

5.8 3rd order nonlinear signal intensity and stokes raman gain. B = 1T, $\gamma = 10^{12}s^{-1}$. 108

1. INTRODUCTION AND BACKGROUND

Monolayer graphene - a plane layer of Carbon atoms arranged in a honeycomb lattice - is the 'most two-dimensional' system ever discovered[1]. Such sheets have long been known to exist in disguised forms like graphite, carbon nanotubes and fullerenes (C_{60}). However, until the year of 2004, it was generally believed that it would be impossible to isolate a monolayer pure graphene, and such an extended graphene sheet would not be stable against thermal effects and other fluctuations. In that year, Andre Geim's research group at the University of Manchester in the UK created single graphene sheets by peeling them off a graphite substrate using scotch tape, and observed them as indeed single-sheet by simple optical microscopy[2]. In recent years, many other methods are developed to control the growth of graphene sheets, including segregation by heat treatment of carbon-containing substrates[3][4][5], liquid-phase exfoliation (LPE)[6][7][8][9] and chemical vapour deposition (CVD)[10][11][12][13]. Furthermore, bilayer and multilayer sheets can be prepared and characterized nowadays[13].

The band structure of monolayer graphene was first studied by P. R. Wallace in 1947[14][15], which showed a unusual semimetallic behavior. This work served as a starting point to study graphite because people at that time thought that a purely two-dimensional structure was not reality. A molecular orbital picture for an isolated carbon atom is $(1s)^2(2s)^2(2p)^4$. In monolayer graphene, the $1s$ electrons remain inert, and the $2s$ and $2p$ electrons hybridize and form three sp^2 orbitals, leaving over a pure p-orbital. The lattice thus forms the honeycomb lattice.

One of the most interesting aspects of the graphene problem is that the electrons in the Dirac cone (low-energy excitations) are massless, chiral, Dirac fermions[14].

This particular energy dispersion mimics the quantum electrodynamics for massless fermions except that in graphene the Dirac fermions move with a speed that is 300 times smaller than the speed of light[15][16][17]. The Dirac fermion nature leads to a series of new physical phenomena, such as the anomalous integer quantum Hall effect (IQHE)[18][19], which is a trademark of Dirac fermion behavior. The IQHE in graphene can be experimentally measured at room temperature[20] due to the large cyclotron energy of graphene. Other interesting features of graphene that are the characteristics of Dirac fermions include the Klein paradox[21], which is the insensitivity to external electrostatic potential; a 'minimum' conductivity even when the carrier concentration is almost zero[1]; and a π phase shift of Shubnikov-de Haas oscillations[1].

The richness of the optical properties of graphene also attracts enormous interest. For instance, graphene exhibits constant white light absorbance[22], where the transmittance can be expressed in terms of the fine-structure constant. Hot luminescence is observed as a consequence of non-equilibrium carriers[23][24], and Pauli blocking results in saturable absorption[25][26]. In addition, the linear dispersion of Dirac-like electrons of graphene makes broadband applications possible. People believe these Dirac-like fermions in graphene also exhibit promising applications in photonics and optoelectronics[27]. Graphene possesses low sheet resistance and high transparency[28], making graphene sheet a promising material to build optoelectronic devices such as displays, touch screens and light-emitting diodes[27]. Graphene-based photodetectors are demonstrated to be ultrafast and be able to work over a very broad wavelength range[29][30]. Graphene devices can also be used for terahertz detection and frequency conversion, including modulators, filters, switches and polarizers[27].

1.1 Band structure of monolayer graphene

The electronic band structure of graphene has been extensively studied starting from Wallace in 1947[15]. Graphene is made out of carbon atoms arranged in hexagonal structure. Each carbon atom has four valence electrons, three of which form tight bonds with the three neighbor atoms. As a result, each atom has one conduction electron in $2p_z$ state. As shown in Fig. 1.1, the lattice vectors can be

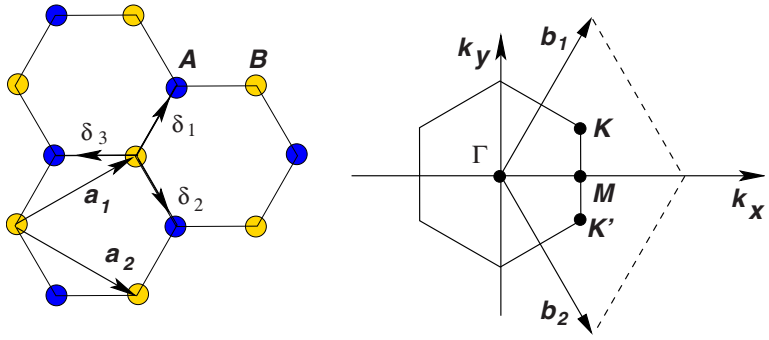

Figure 1.1: Left: lattice structure of graphene. a_1 and a_2 are the lattice unit vectors, and δ_1, δ_2 and δ_3 are the nearest-neighbor vectors. Right: the corresponding first Brillouin zone. (Reprinted figure with permission from Castro Neto et al., *Rev. Mod. Phys.*, Vol.81, No.1, Jan.-Mar. 2009. Copyright (2009) by the American Physical Society. http://journals.aps.org/rmp/abstract/10.1103/RevModPhys.81.109)

written as

$$\mathbf{a}_1 = \frac{a}{2}(3, \sqrt{3}), \mathbf{a}_2 = \frac{a}{2}(3, -\sqrt{3}).$$

Here $a \approx 0.142nm$ is the carbon-carbon distance. There are two different points K and K' at the corners of the graphene Brillouin zone, which are named Dirac points.

The Brillouin zone of graphene is also a hexagonal structure, with reciprocal-lattice vectors given by

$$\mathbf{b}_1 = \frac{2\pi}{3a}(1, \sqrt{3}), \mathbf{b}_2 = \frac{2\pi}{3a}(1, -\sqrt{3}).$$

Considering the nearest- and next-nearest-neighbor interaction, the tight-binding Hamiltonian for electrons in graphene is given by

$$H = -\gamma_0 \sum_{<i,j>,\sigma} (a^\dagger_{\sigma,i} b_{\sigma,j} + H.c.) - \gamma'_0 \sum_{<<i,j>>,\sigma} (a^\dagger_{\sigma,i} a_{\sigma,j} + b^\dagger_{\sigma,i} b_{\sigma,j} + H.c.), \qquad (1.1)$$

where $a_{i,\sigma}(a^\dagger_{i,\sigma})$ annihilates (creates) an electron with spin σ on sublattice A, and $b_{i,\sigma}(b^\dagger_{i,\sigma})$ annihilates (creates) an electron with spin σ on sublattice B. γ_0 and γ'_0 are the nearest- and next-nearest-neighbor hopping energy. The *ab initio* calculations find the relation between γ_0 and γ'_0 by $0.02\gamma_0 \leq \gamma'_0 \leq 0.2\gamma_0$. The energy bands are then given by

$$\begin{aligned} E_s(\mathbf{k}) &= s\gamma_0 \sqrt{3 + 4\cos\frac{\sqrt{3}k_x a}{2}\cos\frac{\sqrt{3}k_y a}{2} + 2\cos\sqrt{3}k_y a} \\ &- \gamma'_0 \sqrt{4\cos\frac{\sqrt{3}k_x a}{2}\cos\frac{\sqrt{3}k_y a}{2} + 2\cos\sqrt{3}k_y a}. \end{aligned}$$

Here the $s = \pm$ applies to the upper and lower band, respectively. As shown in Fig. 1.2, the spectrum is symmetric around zero energy if $\gamma'_0 = 0$, and the electron-hole symmetry is broken when the next-nearest-neighbor hopping becomes finite. In the vicinity of Dirac points, we can obtain the energy dispersion by expanding full band structure close to $\mathbf{K}$ (or $\mathbf{K}$') as $\mathbf{k} = \mathbf{K} + \mathbf{q}$, with $|\mathbf{q}| \ll |\mathbf{K}|$:

$$E_\pm(\mathbf{q}) \approx \pm\hbar v_F |\mathbf{q}| + O[(\frac{\mathbf{q}}{K})^2]. \qquad (1.2)$$

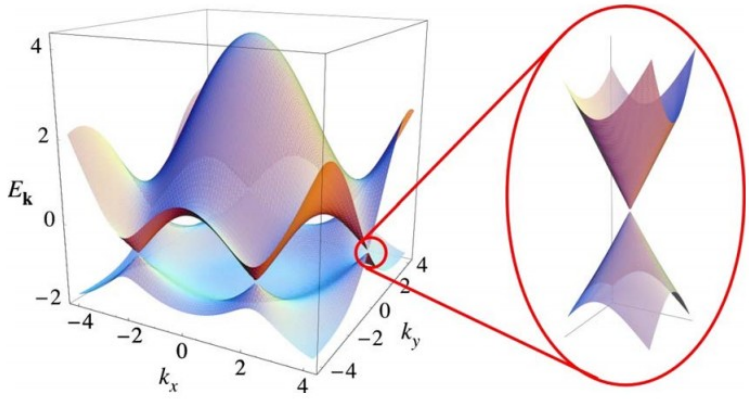

Figure 1.2: Energy spectrum with t = 2.7 eV and t' = -0.2 t, and zoom in of the energy bands close to one of the Dirac points. (Reprinted figure with permission from Castro Neto et al., *Rev. Mod. Phys.*, Vol.81, No.1, Jan.-Mar. 2009. Copyright (2009) by the American Physical Society. http://journals.aps.org/rmp/abstract/10.1103/RevModPhys.81.109)

band structure close to **K** (or **K**') as $\mathbf{k} = \mathbf{K} + \mathbf{q}$, with $|\mathbf{q}| \ll |\mathbf{K}|$:

$$E_{\pm}(\mathbf{q}) \approx \pm\hbar v_F|\mathbf{q}| + O[(\frac{\mathbf{q}}{K})^2]. \tag{1.2}$$

Here $\mathbf{q}$ is the momentum measured relatively to the Dirac points, and v_F is the Fermi velocity given by $v_F = 3\gamma_0/2\hbar a \approx 10^8 cm/s$. The most significant difference between this energy dispersion and the usual case $E(q) = q^2/2m$, where m is the electron mass, is that the fermi velocity of graphene electron near the Dirac point does not depend on the energy or momentum.

To simplify, we neglect the next-nearest-neighbor hopping, electrons near the Dirac points(K and K') can be described by four-component Bloch functions $\Phi = [\phi_{K,A}, \phi_{K',A}, \phi_{K,B}, \phi_{K',B}]$ and the Hamiltonian is written as

$$\hat{H}_0(\vec{q}) = \hbar v_F \Pi_z \otimes \hat{\vec{\sigma}} \cdot \vec{q} \tag{1.3}$$

points:

$$\hat{H}_0(\vec{q}) = \hbar \upsilon_F \begin{pmatrix} 0 & \hat{q}_x - i\hat{q}_y & 0 & 0 \\ \hat{q}_x + i\hat{q}_y & 0 & 0 & 0 \\ 0 & 0 & 0 & \hat{q}_x + i\hat{q}_y \\ 0 & 0 & \hat{q}_x - i\hat{q}_y & 0 \end{pmatrix} \tag{1.4}$$

The corresponding Schrödinger equation

$$\hat{H}_0 \psi = \varepsilon \psi$$

can be solved exactly. The eigenfunctions are given by

$$\begin{aligned} \psi_s^K(\vec{q}, \vec{r}) &= \frac{1}{\sqrt{2L}} \exp(i\vec{q} \cdot \vec{r}) \begin{pmatrix} s \\ e^{i\theta(\vec{q})} \\ 0 \\ 0 \end{pmatrix}; \\ \psi_s^{K'}(\vec{q}, \vec{r}) &= \frac{1}{\sqrt{2L}} \exp(i\vec{q} \cdot \vec{r}) \begin{pmatrix} 0 \\ 0 \\ e^{i\theta(\vec{q})} \\ s \end{pmatrix}, \end{aligned} \tag{1.5}$$

where L^2 is the area of graphene, $\theta(\vec{q})$ is the angle of wave vector $\vec{q}$ with the x-axis, and $s = \pm 1$ denotes the bands (+1 for the conduction band and -1 for the valence band). The corresponding eigenenergy is

$$\varepsilon_{s,q} = s \cdot \hbar \upsilon_F q. \tag{1.6}$$

As we can see, the effective Hamiltonian Eq. (1.3) is block-diagonal. Therefore,

we can also introduce a valley detergency of 2 and write the Hamiltonian and the Schrödinger equation as

$$\hbar \upsilon_F \hat{\vec{\sigma}} \cdot \vec{q} |\psi\rangle = \varepsilon |\psi\rangle, \tag{1.7}$$

which obeys the 2D Dirac equation.

1.2 Surface state of topological insulators

In the past several years a new quantum state, the quantum spin Hall (QSH) states or topological insulator, has been discovered and explored. The three-dimensional (3D) topological insulator supports topologically protected 2D Dirac fermions on its surface due to spin-orbit interaction and time-reversal symmetry[31][32][33][34], which is observed in bulk crystals like Bi_2Se_3, Bi_2Te_3 and Sb_2Te_3[35][36][37][38][39][40]. These surface states exhibit characteristics of 2D Dirac fermions[31] and show promising applications in the terahertz and infrared range[41][42][43]. Recent experiments have demonstrated their longer lifetime as compared to the bulk states, and successfully observed the linear energy dispersion and non-equidistant surface Landau levels in a perpendicular magnetic field[44][45].

We here start from the effective Hamiltonian model of Bi_2Se_3, which exhibits the largest bulk band gap so far. Choosing the hybridized states of Se and Bi orbitals $\{|p1_z^+,\uparrow\rangle, |p2_z^-,\uparrow\rangle, |p1_z^+,\downarrow\rangle, |p2_z^-,\downarrow\rangle\}$, the Hamiltonian of a three-dimensional topological insulator (3DTI) gives

$$H(\mathbf{k}) = \varepsilon_0(\mathbf{k}) I_{4\times 4} + \begin{pmatrix} \mathcal{M}(\mathbf{k}) & -iA_1\partial_z & 0 & A_2 k_- \\ -iA_1\partial_z & -\mathcal{M}(\mathbf{k}) & A_2 k_- & 0 \\ 0 & A_2 k_+ & \mathcal{M}(\mathbf{k}) & iA_1\partial_z \\ A_2 k_+ & 0 & iA_1\partial_z & -\mathcal{M}(\mathbf{k}) \end{pmatrix}, \tag{1.8}$$

where $k_\pm = k_x \pm ik_y$, $\varepsilon_0(k) = C - D_1\partial_z^2 + D_2k^2$, $\mathcal{M}(\mathbf{k}) = M + B_1\partial_z^2 - B_2k^2$, and $A_1, A_2, B_1, B_2, C, D_1, D_2, M$ are the model parameters of the material. Following from Ref.[40], $M = 0.28\mathtt{eV}, A_1 = 2.2\mathtt{eV}\mathring{A}, A_2 = 4.1\mathtt{eV}\mathring{A}, B_1 = 10\mathtt{eV}\mathring{A}^2, B_2 = 56.6\mathtt{eV}\mathring{A}^2, C = -0.0068\mathtt{eV}, D_1 = 1.3\mathtt{eV}\mathring{A}^2, D_2 = 19.6\mathtt{eV}\mathring{A}^2$. This Hamiltonian possesses time-reversal and inversion symmetry. The general solution of the bulk states and surface states can be derived analytically from this Hamiltonian with proper boundary conditions.

However, it is also desirable to establish an effective continuous model to study the properties of topological surface states. The typical way is to expand the 3DTI Hamiltonian using the solutions of the surface states at the Dirac (Γ) point. This is valid when the energy is limited between the conduction bands and valence bands. Thus, the 3DTI Hamiltonian can be rewritten as

$$H(\mathbf{k}) = H_0(\mathbf{k} = 0) + H_1. \tag{1.9}$$

Here

$$H_0 = \begin{pmatrix} h(A_1) & 0 \\ 0 & h(-A_1) \end{pmatrix},$$

with

$$h(A_1) = \begin{pmatrix} -D_-\partial_z^2 + C + M & -iA_1\partial_z \\ -iA_1\partial_z & -D_+\partial_z^2 + C - M \end{pmatrix};$$

and

$$H_1 = \begin{pmatrix} D_2k^2 - B_2k^2\sigma_z & A_2k_-\sigma_x \\ A_2k_+\sigma_x & D_2k^2 - B_2k^2\sigma_z \end{pmatrix}.$$

The basis states at the Γ point are obtained by solving

$$H_0\Psi = \varepsilon\Psi.$$

Since H_0 is block-diagonal, the solution can be found by solving each block separately:

$$h(A_1)\Psi_\uparrow = \varepsilon\Psi_\uparrow; \quad h(-A_1)\Psi_\downarrow = \varepsilon\Psi_\downarrow.$$

The corresponding four eigenstates are in the form of

$$\Psi_1 = \begin{bmatrix} \phi(A_1) \\ 0 \end{bmatrix}; \Psi_2 = \begin{bmatrix} \chi(A_1) \\ 0 \end{bmatrix}; \Psi_3 = \begin{bmatrix} 0 \\ \phi(-A_1) \end{bmatrix}; \Psi_4 = \begin{bmatrix} 0 \\ \chi(-A_1) \end{bmatrix},$$

where the explicit expressions for χ and ϕ can be found in Ref. [46]. Projected onto these four states, the Hamiltonian in the vicinity of the Γ point can be expanded in an effective form:

$$H_{eff} = \begin{pmatrix} h_+ & 0 \\ 0 & h_- \end{pmatrix}, \tag{1.10}$$

with

$$h_+ = E_0 - Dk^2 + \begin{pmatrix} \Delta/2 - Bk^2 & \tilde{A}_2 k_- \\ \tilde{A}_2^* k_+ & -\Delta/2 + Bk^2 \end{pmatrix};$$

$$h_- = E_0 - Dk^2 + \begin{pmatrix} -\Delta/2 + Bk^2 & -\tilde{A}_2^* k_- \\ -\tilde{A}_2 k_+ & \Delta/2 - Bk^2 \end{pmatrix};$$

and

$$B = (\tilde{B}_1 - \tilde{B}_2)/2, D = (\tilde{B}_1 + \tilde{B}_2)/2 - D_2,$$

$$E_0 = (E_+ + E_-)/2, \Delta = E_+ - E_-,$$

$$\tilde{B}_1 = B_2\langle\phi(A_1)|\sigma_z|\phi(A_1)\rangle, \tilde{B}_2 = B_2\langle\chi(A_1)|\sigma_z|\chi(A_1)\rangle,$$
$$\tilde{A}_2 = A_2\langle\phi(A_1)|\sigma_z|\chi(-A_1)\rangle.$$

These parameters are thickness-dependent. In the thickness of our interest (i.e. above 6 QLs), they are nearly constants with $E_0 = 0.0337\text{eV}, D = -12.25\text{eV}\mathring{A}^2, \hbar v_F = 4.07\text{eV}\mathring{A}, \Delta = 0$, and $B = 0$. As a result, the surface states become gapless, and the effective Hamiltonian Eq. 1.10 is further simplified to

$$H_{eff} = E_0 - Dk^2 + \hbar v_F \left(k_y\sigma_x - k_x\sigma_y\right) \tag{1.11}$$

with a surface degeneracy factor of 2. However, when the thickness of topological insulator thin film is small enough (less than 6 QLs), the tunneling effect between upper and lower surfaces becomes strong, and opens an finite energy gap at the Dirac point[46][47].

When the two surface layers are well separated (e.g. a topological insulator slab geometry), the surface states at each surfaces are no longer coherent. One way to simplify the effective Hamiltonian Eq. 1.10 is applying the semi-infinite boundary condition on each surface:

$$H_{eff} = C + \frac{D_1 M}{B_1} + (D_2 - B_2\frac{D_1}{B_1})k^2 + A_2\sqrt{1-(D_1/B_1)^2}(\sigma_x k_y - \sigma_y k_x). \tag{1.12}$$

The effective Hamiltonian of the top and bottom surface states have the same form when the coupling between the two surfaces are neglected[46][47]. In the isotropic case, $D_1 = D_2$ and $B_1 = B_2$, thus the quadratic term vanishes and we get a pure linear energy dispersion relationship in the vicinity of the Dirac point. The Bi_2Se_3 material we are discussing here is not isotropic, so that the 2nd-order correction

remains in the effective Hamiltonian.

As we are more interested in the gapless bandstructure and the optical properties stemming from the 2D Dirac fermion nature of topological surface state, we'll use the effective Hamiltonian

$$H_{eff}(\mathbf{k}) = E_0 - Dk^2 + \hbar\upsilon_F(k_y\sigma_x - k_x\sigma_y) \tag{1.13}$$

in our following calculations to study the optical response of topological surface states.

1.3 Landau levels of 2D Dirac fermion systems

The characteristics of 2D Dirac fermion systems (e.g. monolayer graphene and surface layer of topological insulator) in an external magnetic field show stark contrast to conventional 2D electron systems. In an external magnetic field $B\hat{z}$ perpendicular to the plane of graphene or TI surface layer, the continuous energy bands near the Dirac points split into discrete Landau levels[19]. The effective-mass Hamiltonian Eq. (1.3) for a monolayer graphene is rewritten as a 4×4 matrix using Peierls substitution:

$$\hat{H}_0(\hat{\vec{\pi}}) = \upsilon_F \begin{pmatrix} 0 & \hat{\pi}_x - i\hat{\pi}_y & 0 & 0 \\ \hat{\pi}_x + i\hat{\pi}_y & 0 & 0 & 0 \\ 0 & 0 & 0 & \hat{\pi}_x + i\hat{\pi}_y \\ 0 & 0 & \hat{\pi}_x - i\hat{\pi}_y & 0 \end{pmatrix}, \tag{1.14}$$

where $\hat{\vec{\pi}} = \vec{p} + e\vec{A}/c$. $\vec{p}$ is the electron momentum operator, and $\vec{A}$ is the vector potential, which equals to $(0, Bx)$ for a constant magnetic field in the Landau gauge. In this Hamiltonian the coupling between two different Dirac points is neglected, so

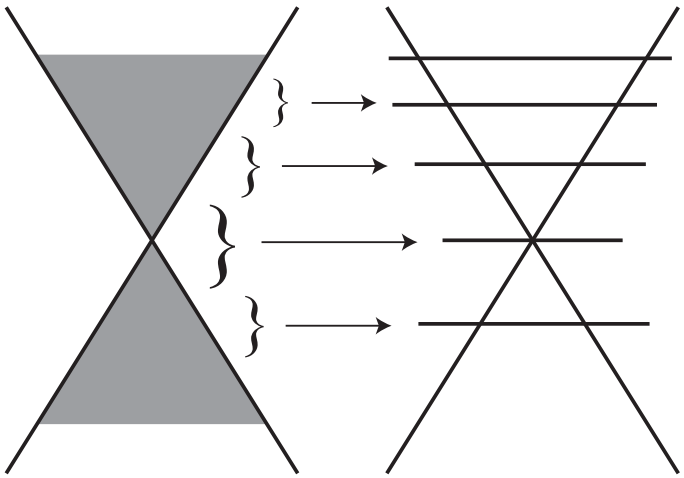

Figure 1.3: In an external magnetic field perpendicular to the plane of graphene, the continuous energy bands near the Dirac point split into discrete Landau levels. (figure attached from A. J. Leggett's lecture notes.)

we can write down the solutions to the Schrödinger equation $\hat{H}_0(\hat{\vec{\pi}})\Psi = \varepsilon\Psi$ separately for each Dirac point. For example, the effective Hamiltonian near the K point is $\hat{H}_K = \upsilon_F \hat{\vec{\sigma}} \cdot \hat{\vec{\pi}}$. The resulting eigenfunction is specified by two quantum numbers n and q_y, where $n = 0, \pm 1, \pm 2, \cdots$, and q_y is the electron wave vector along y direction:

$$\Psi_{n,K}(q_y, r) = \frac{C_n}{\sqrt{L}} \exp(-iq_y y) \begin{pmatrix} \mathrm{sgn}(n) i^{|n|-1} \phi_{|n|-1} \\ i^{|n|} \phi_{|n|} \\ 0 \\ 0 \end{pmatrix};$$

$$\Psi_{n,K'}(q_y,r) = \frac{C_n}{\sqrt{L}}\exp(-iq_y y)\begin{pmatrix} 0 \\ 0 \\ i^{|n|}\phi_{|n|} \\ \mathrm{sgn}(n)i^{|n|-1}\phi_{|n|-1} \end{pmatrix}, \tag{1.15}$$

with

$$C_n = \begin{cases} 1 & (n=0) \\ \frac{1}{\sqrt{2}} & (n\neq 0) \end{cases};$$

$$\mathrm{sgn}(n) = \begin{cases} 1 & (n>0) \\ 0 & (n=0) \\ -1 & (n<0) \end{cases},$$

and

$$\phi_{|n|} = \frac{H_{|n|}\left((x-l_c^2k_y)/l_c\right)}{\sqrt{2^{|n|}|n|!\sqrt{\pi}l_c}}\exp\left[-\frac{1}{2}\left(\frac{x-l_c^2k_y}{l_c}\right)^2\right],$$

where $l_c = \sqrt{c\hbar/eB}$ is the magnetic length, $H_n(x)$ the Hermite polynomial. The corresponding eigenenergy is

$$\varepsilon_n = \mathrm{sgn}(n)\hbar\omega_c\sqrt{|n|}, \quad \text{with} \quad \omega_c = \sqrt{2}v_F/l_c. \tag{1.16}$$

A positive or negative value of n corresponds to electrons or holes. Compared with Landau levels for a conventional 2D electron/hole system with a parabolic dispersion, $E_n = (n+1/2)\hbar eB/m^*$, Landau levels in graphene are unequally spaced: $\propto \sqrt{B}$. As shown in Fig. 1.3, the magnetic field 'condenses' the original states in the Dirac cone into discrete energies, and each Landau level contains the same areal density of states $N_\Phi = 1/(2\pi {l_c}^2)$, not including spin and valley degeneracy factors. Infrared spectroscopy of Landau levels of graphene has already been realized in experiments[76],

and becomes a strong tool to study Quantum Hall Effects as well as graphene's magneto-optical properties[42].

The surface state of a topological insulator possesses similar non-equidistant Landau levels in a magnetic field due to the nature of Dirac fermion[44][45]. After placing topological insulator into a uniform perpendicular magnetic field, the orbital effect is included by Perierls substitution $\pi = k + \frac{e}{\hbar}A$. The previous Hamiltonian (Eq. (1.13)) is rewritten after introducing annihilation and creation operators $a = \frac{l_c}{\sqrt{2}}\pi_-$ and $a^\dagger = \frac{l_c}{\sqrt{2}}\pi_+$. Here l_c is the magnetic length $\sqrt{\frac{\hbar}{eB}}$.

$$H_{ss}(\pi) = E_0 - \frac{2D}{l_c^2}(a^\dagger a + \frac{1}{2}) + \frac{\sqrt{2}\hbar\upsilon_F}{l_c}\begin{pmatrix} 0 & ia \\ -ia^\dagger & 0 \end{pmatrix}. \tag{1.17}$$

Utilizing the relations of

$$a^\dagger\psi_{|n|} = \sqrt{|n|+1}\psi_{|n|+1}, \quad a\psi_{|n|} = \sqrt{|n|}\psi_{|n|-1},$$

the eigenfunctions and eigenvalues can be solved as

$$\begin{aligned} \Psi_n &= \frac{C_n}{\sqrt{L}}e^{-ik_y y}\left(\mathrm{sgn}(n)\cdot \mathrm{i}^{|n|}\psi_{|n|-1},\ \mathrm{i}^{|n|-1}\psi_{|n|}\right)^T, \\ E_n &= E_0 - \frac{2|n|D}{l_c^2} + \mathrm{sgn}(n)\sqrt{2|n|(\frac{\hbar\upsilon_F}{l_c})^2 + (\frac{D}{l_c})^2}. \end{aligned} \tag{1.18}$$

Here $C_0 = 1$, $C_{n\neq 0} = 1/\sqrt{2}$, and $\psi_{|n|}$ is a orthogonal Hermite polynomial. Unlike monolayer graphene, spin is coupled in the Hamiltonian of topological insulator surface state. In each surface Landau level $\Psi_n \sim \left(\mathrm{sgn(n)}\psi_{|n|-1}, \psi_{|n|}\right)^T$, $\psi_{|n|-1}$ denotes the spin-up component and $\psi_{|n|}$ denotes its spin-down component. The spin texture

on each surface Landau level is discussed in more details in Chapter 5. Magnetic field condenses the continuous k-dependent states onto discrete surface Landau states, and brings a k degeneracy of $\frac{1}{2\pi lc^2}$. For a topological insulator slab, surface Landau levels are localized near the surfaces. However, when the thickness is in several QLs, which is comparable to the decay length of surface state, the surface state will fill up the whole film[47]. In addition, when the thickness of the film is below 6QLs, the 0th landau level further splits into 2 spin down energy levels due to the tunneling effects[46].

In the terahertz and mid-infrared range, it is safe to only keep the linear term in the Hamiltonian for each surface layer

$$H_{ss}(\pi) = E_0 - \hbar\upsilon_F(\pi_x\sigma_y - \pi_y\sigma_x), \tag{1.19}$$

Compared with graphene, the surface state in a topological insulator possesses similar linear energy dispersion relation near Dirac point, and follows similar Landau level pattern in a magnetic field. Strong cyclotron resonance features as well as high optical nonlinearities are expected for the topological insulator material in a magnetic field.

1.4 Surface plasmon mode in 2D Dirac fermion systems

A conventional surface plasmon is a collective mode of coupled charge-density and field oscillations at an interface between a free-carrier system and a dielectric or vacuum, which plays a fundamental role in the dynamic responses of electron systems and forms the basis of research in optical metamaterials[48][49][50]. Plasmonics seems to be the only viable path to realize nanophotonics, which aims to control light at scales substantially smaller than the wavelength. Currently, one large obstacle toward achieving this vision is the fact that plasmonic materials have enormous losses in the frequency of interests (such as terahertz and infrared). Stemming from

the unique bandstructure and high electron mobility of graphene, graphene-based plasmons possess high wave confinement, low dissipation and relatively longer propagation distance[51][52][53][54]. Graphene plasmonics also exhibit strong oscillation strengths at room-temperature, while plasmon absorption in a conventional 2D electron gas was observed only at very low temperature[55][56]. In addition, the intrinsic graphene plasmons can be easily tuned by gating or doping, making graphene plasmonics an attractive alternative to noble-metal plasmonics and possesses potential applications in the infrared and terahertz frequency range[53][57][58][59].

Before showing the explicit derivation of the plasmon mode supported by the 2D Dirac fermion systems, I'll first introduce the optical conductivity (or linear electric susceptibility) of the 2D Dirac fermion system in the absence of a magnetic field calculated from Keldysh's Green function(Ref. [60]):

$$\begin{aligned}\sigma_{ij}(\omega,q) &= \frac{ie^2}{\pi^2}\times\left\{\sum_{a=1,2}\int\frac{d^2p v^i v^j f[\epsilon_a(p_-)]-f[\epsilon_a(p_+)]}{[\epsilon_a(p_+)-\epsilon_a(p_-)][\omega-\epsilon_a(p_+)+\epsilon_a(p_-)]}\right.\\ &+ \left.\int\frac{d^2p 2\omega v_{12}^i v_{21}^j f[\epsilon_1(p_-)]-f[\epsilon_2(p_+)]}{[\epsilon_2(p_+)-\epsilon_1(p_-)]\omega^2-[\epsilon_2(p_+)-\epsilon_1(p_-)]^2}\right\}. \qquad (1.20)\end{aligned}$$

In this expression, ω and q are frequency and x-component of the wave vector in a monochromatic wave. The first term counts the contribution from intraband transitions, while the latter term describes the contribution from interband transitions. The velocity operator here is in a very simple form. For graphene fermions, the velocity operator is in the form:

$$\upsilon_F\begin{pmatrix}0 & -\hat{x}+i\hat{y}\\ -\hat{x}-i\hat{y} & 0\end{pmatrix}.$$

For the surface states in topological insulator materials, the velocity operator is:

$$v_F \begin{pmatrix} 0 & -\hat{x} - i\hat{y} \\ -\hat{x} + i\hat{y} & 0 \end{pmatrix}.$$

We here derive the surface plasmon mode in 2D Dirac fermion systems by solving the Maxwell's equations explicitly with appropriate boundary conditions.

$$\begin{aligned} \nabla \times \vec{E} = -\tfrac{1}{c}\tfrac{\partial \vec{B}}{\partial t}, \quad \nabla \times \vec{B} = \frac{4\pi}{c}\vec{j} + \frac{1}{c}\frac{\partial \vec{E}}{\partial t}, \\ \nabla \vec{E} = 4\pi\rho, \qquad \nabla \vec{B} = 0. \end{aligned} \tag{1.21}$$

We seek the solutions for the fields in the form:

$$\vec{E} = \mathbf{E}(z)e^{iqx - i\omega t}, \quad \vec{B} = \mathbf{B}(z)e^{iqx - i\omega t}.$$

In the bulk region, the fields satisfy

$$\nabla \times \nabla \times \mathbf{F} - \frac{\omega^2}{c^2}\mathbf{F} = 0, \tag{1.22}$$

where we denoted $\mathbf{F} = \mathbf{E}, \mathbf{B}$. So each component of the electric and magnetic field satisfies the Helmholtz equation:

$$\left(\frac{\partial^2}{\partial z^2} - q^2 + \frac{\omega^2}{c^2}\right) F_{x,y,z} = 0. \tag{1.23}$$

The Maxwell's equations give the relations between each field component as:

$$\begin{aligned} iqE_x = -\frac{\partial E_z}{\partial z}, \qquad iqB_x = -\frac{\partial B_z}{\partial z}; \\ B_z = \frac{qc}{\omega}E_y, \qquad B_y = -\frac{\omega}{qc}E_z. \end{aligned} \tag{1.24}$$

For a single layer 2D Dirac fermion system (e.g. monolayer graphene) placed on an interface between two dielectric media with dielectric constants ϵ_1 and ϵ_2 (as shown in the inset to Fig. 1.4), the monolayer electron system supports a EM-mode with non-zero field components with the relationships given by

$$E_x = V_\pm e^{\mp p_{1,2} z}, \quad E_z = \pm i \tfrac{q}{p_{1,2}} V_\pm e^{-p_{1,2} z}, \quad B_y = \mp i \frac{\epsilon_{1,2}\omega}{c p_{1,2}} V_\pm e^{-p_{1,2} z}.$$
$$E_y = W_\pm e^{\mp p_{1,2} z}, \quad B_x = \mp i \tfrac{c p_{1,2}}{\omega} W_\pm e^{\mp p_{1,2} z}, \quad B_z = \frac{qc}{\omega} W_\pm e^{\mp p_{1,2} z}.$$

Here $\pm$ denotes the field components in the bulk regions $z > 0$ and $z < 0$, respectively; $p_{1,2} = \sqrt{q^2 - \epsilon_{1,2}\frac{\omega^2}{c^2}}$ determines the inverse confinement length in z-direction. Free electrons are localized on the interface, so we can write the surface current and surface density as $\vec{j} = \vec{j}_\perp \delta(z)$ and $\rho = \rho_\perp \delta(z)$. The fields on both sides satisfy the boundary conditions

$$\begin{cases} \epsilon_1 E_z(+0) - \epsilon_2 E_z(-0) = \frac{4\pi q}{\omega} \left(\sigma_{xx} E_x(0) + \sigma_{xy} E_y(0)\right), \\ \epsilon_1 B_x(+0) - \epsilon_2 B_x(-0) = \frac{4\pi}{c} \left(\sigma_{yy} E_y(0) + \sigma_{yx} E_x(0)\right), \\ E_x(+0) - E_x(-0) = 0, \quad B_z(+0) - B_z(-0) = 0. \end{cases}$$

These simplify to $V_+ = V_- = V$, $W_+ = W_- = W$ and

$$\begin{cases} \left(\frac{\epsilon_1 q}{p_1} + \frac{\epsilon_2 q}{p_2} + i\frac{4\pi q}{\omega}\sigma_{xx}\right) \cdot V + i\frac{4\pi q}{\omega}\sigma_{xy} \cdot W = 0; \\ -i\frac{4\pi}{c}\sigma_{yx} \cdot V + \left(\frac{\epsilon_1 c p_1}{\omega} + \frac{\epsilon_2 c p_2}{\omega} - i\frac{4\pi}{c}\sigma_{yy}\right) \cdot W = 0. \end{cases} \tag{1.25}$$

For monolayer graphene, the optical conductivity gives $\sigma_{xx} = \sigma_{yy} \neq 0$ and $\sigma_{xy} = \sigma_{yx} = 0$. Combine with Eq. (1.25), we are able to conclude the energy dispersion of

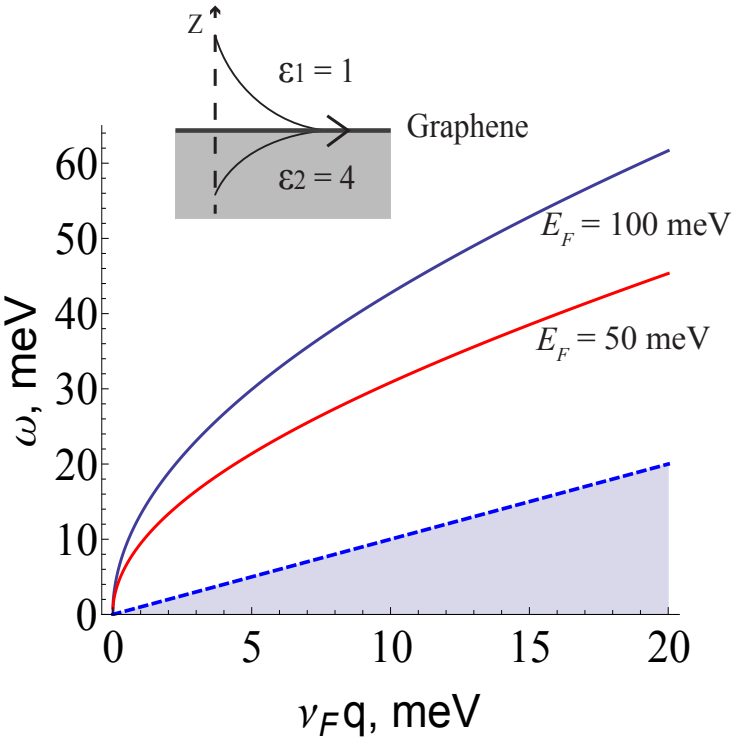

Figure 1.4: Dispersion curve of a surface plasmon mode in monolayer graphene for Fermi level $E_F = 50$ meV. The dielectric constant $\epsilon_2 = 4$ corresponds to SiO_2 in the THz region. Shaded area is the Landau damping region.

surface mode in monolayer graphene:

$$D(\omega,q)=i\frac{4\pi}{\omega}\sigma_{xx}(\omega,q)+\frac{\epsilon_1}{p_1}+\frac{\epsilon_2}{p_2}=0. \tag{1.26}$$

Its solution for the real parts of the frequency and wavenumber is shown in Fig. 1.4. In the limit that Fermi energy is greater than plasmon energy, interband transitions are much less efficient than intraband transitions. We can simplify the calculation by only counting surface polarization resulting from intraband transitions. When $cq \gg \omega \gg \upsilon_F q$, the dispersion relation can be simplified to $i4\pi\sigma(\omega,q)q + (\epsilon_1+\epsilon_2)\omega \approx 0$, and further to the familiar dependence $\omega(q) \propto \sqrt{E_F q}$ if we neglect the q-dependent term in the denominator of Eq. (2.18). With increasing plasmon frequency, the plasmon-phonon coupling and interband transitions need to be taken into account[61].

The double layer geometry shown in the inset to Fig. 1.5 supports two types of surface plasmon modes[62]: symmetric ω_+ and antisymmetric ω_- (only the field of the symmetric mode is shown in the inset). The symmetric EM mode is robust to many-body effects and has the form:

$$\begin{aligned}
|z| \le \frac{d}{2} \quad &: \quad E_x=\mathcal{E}_0\cosh p_2 z;\, E_z=-i\frac{q}{p_2}\mathcal{E}_0\sinh p_2 z;\, B_y=+i\frac{\epsilon_2\omega}{p_2 c}\mathcal{E}_0\sinh p_2 z. \\
|z| > \frac{d}{2} \quad &: \quad E_x=\mathcal{E}_\pm e^{\mp p_1(z\pm\frac{d}{2})},\, E_z=\pm i\frac{q}{p_1}\mathcal{E}_\pm e^{\mp p_1(z\pm\frac{d}{2})},\, B_y=\mp i\frac{\epsilon_1\omega}{cp_1}\mathcal{E}_\pm e^{\mp p_1(z\pm\frac{d}{2})}.
\end{aligned} \tag{1.27}$$

Here $\pm$ denotes the field components in the bulk regions $z > \frac{d}{2}$ and $z < -\frac{d}{2}$; 0 denotes the field inside the two surface layers $|z| \le \frac{d}{2}$. Field components E_y, B_x and B_z are determined by the relations given in Eq. (1.24). Such a geometry appears naturally in thin films of TIs and can be also implemented by separating two graphene layers

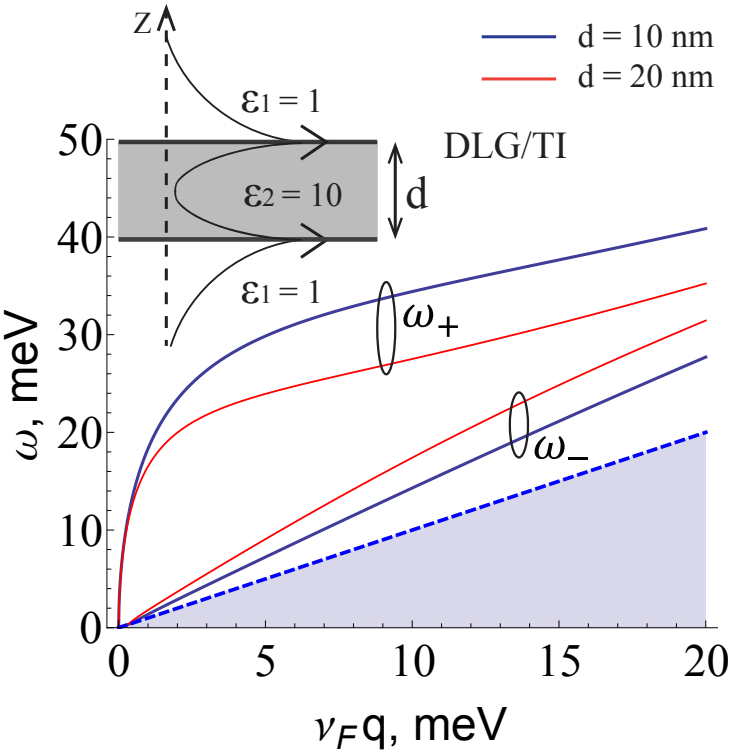

Figure 1.5: Dispersion curves for symmetric (ω_+) and antisymmetric (ω_-) plasmon modes in a thin TI film forming a double layer with a spacer thickness $d = 10, 20$ nm; $E_F = 100$ meV. Electric field of the symmetric plasmon mode is shown in the inset. The value of $\epsilon_2 = 10$ typical for semiconductors was assumed. Shaded area is the Landau damping region.

with a dielectric. The plasmon modes in a double layer were studied theoretically by a different method[63][64][65]. Here, instead of using the static dispersion relation $\epsilon(\omega, q) = 0$, we start from the full Maxwell's equations Eq. (1.21) with $\vec{j} = \vec{j}_\perp \delta(z \pm \frac{d}{2})$ and $\rho = \rho_\perp \delta(z \pm \frac{d}{2})$ and boundary conditions on the two surfaces:

$$\begin{cases} E_x(\frac{-d}{2}+) - E_x(\frac{-d}{2}-) = 0, \\ E_x(\frac{d}{2}+) - E_x(\frac{d}{2}-) = 0, \\ \epsilon_1 E_z(\frac{d}{2}+) - \epsilon_2 E_z(\frac{d}{2}-) = \frac{4\pi q}{\omega}\left(\sigma_{xx} E_x(\frac{d}{2}) + \sigma_{xy} E_y(\frac{d}{2})\right), \\ \epsilon_2 E_z(\frac{-d}{2}+) - \epsilon_1 E_z(\frac{-d}{2}-) = \frac{4\pi q}{\omega}\left(\sigma_{yx} E_x(\frac{d}{2}) + \sigma_{yy} E_y(\frac{d}{2})\right). \end{cases} \tag{1.28}$$

and derive the following dispersion equations for the symmetric (top) and antisymmetric (bottom) modes:

$$D(\omega, q) = \begin{cases} 4\pi \frac{i\sigma_{xx}}{\omega} + \frac{\epsilon_1}{p_1} + \frac{\epsilon_2}{p_2} \tanh(p_2 \frac{d}{2}) = 0; & \text{symmetric} \\ 4\pi \frac{i\sigma_{xx}}{\omega} + \frac{\epsilon_1}{p_1} + \frac{\epsilon_2}{p_2} \coth(p_2 \frac{d}{2}) = 0; & \text{antisymmetric} \end{cases}, \tag{1.29}$$

where d is the distance between two 2D layers of massless Dirac electrons. Generalization to the case when the top and bottom media have different dielectric constants is straightforward, but makes the equations more cumbersome. The solution to the dispersion equations is shown in Fig. 1.5. We consider the limit when d is thicker than about 7 nm so that the electron hybridization and tunneling can be neglected[46], but on the other hand, d is thin enough to satisfy $p_2 d \ll 1$ which ensures strong electromagnetic coupling. For the plasmon frequency of 1 THz the latter means $d \ll 1$ μm. In the limit of a thick spacer $p_2 d \to \infty$, the ω_+ and ω_- modes merge and turn into uncoupled monolayer plasmon modes supported by each surface.

2. LINEAR AND NONLINEAR OPTICS OF MONOLAYER GRAPHENE*

Graphene has unique electronic and optical properties stemming from linear, massless dispersion of electrons near the Dirac point and the chiral character of electron states[14, 22]. Magnetooptical properties of graphene and thin graphite layers are particularly interesting, showing multiple absorption peaks and unique selection rules for transitions between Landau levels [60, 66, 67, 68, 69]. Recent progress in growing high-quality epitaxial graphene and graphite with high room-temperature mobility and strong magnetooptical response attracted a lot of interest and showed the promise of new applications in the infrared optics and photonics [70, 71, 72]. The time is ripe to explore the nonlinear optical properties of a magnetized graphene and their applications. We have recently shown that graphene placed in a magnetic field possesses perhaps the highest infrared optical nonlinearity among known materials [67]. Here we present detailed derivation of the linear and nonlinear response of magnetized graphene based on a rigorous density-matrix formalism. We apply this approach to calculate the terahertz radiation power generated by third-order nonlinear optical processes: four-wave mixing[67]and stimulated Raman scattering[68]. We argue that an extremely strong nonlinearity of graphene in combination with its unique selection rules makes graphene a promising material for the next generation of compact optoelectronic devices.

*Reprinted with permissions from Giant Optical Nonlinearity of Graphene in a Strong Magnetic Field by Xianghan Yao and Alexey Belyanin, 2012. Phys. Rev. Lett., vol. 108, pp. 255503, Copyright [2012] by the American Physical Society, and Nonlinear Optics of Graphene in a Strong Magnetic Field by Xianghan Yao and Alexey Belyanin, 2013. J. Phys.: Condens. Matter, vol. 25, pp. 054203, Copyright [2013] by IOP Science.

2.1 Density matrix formalism in Schrödinger picture

In quantum mechanics, a density matrix is a Hermitian matrix that describe the statistical state of a quantum system, and is widely used to describe and perform calculations with mixed states because any state, pure or mixed, can be characterized by a single density matrix. If we know the density matrix of a system, we can calculate the mean value of any physical quantities of the system. It is a very useful quantum mechanical method to study optical properties of a material, which is capable to deal with effects such as collision broadening, disorder and many-body carrier-carrier interactions. If a quantum-mechanical system is in a particular state denoted as s, we can describe the physical properties of the system in terms of state wavefunction $\psi_s(\vec{r},t)$, which obeys the Schrödinger equation

$$i\hbar\frac{\partial\psi(\vec{r},t)}{\partial t}=\hat{H}\psi(\vec{r},t);\qquad \hat{H}=\hat{H}_0+\hat{V}(t), \tag{2.1}$$

Where $\hat{H}_0$ is the Hamiltonian of a free atom, and V_0 is the interaction term. Choosing the eigenfunction $u_n(\vec{r})$ of $\hat{H}_0$ as basis, the wave function of state s can be represented as $\psi_s(\vec{r},t)=\sum_n {C_n}^s(t)u_n(\vec{r})$. And the mean value of a Hermitian operator $\hat{A}$ is

$$\langle A\rangle=\int {\psi_s}^*\hat{A}\psi_s d^3r=\sum_{n,m}C_n^{s*}(t)C_m^s(t)A_{nm},\qquad A_{nm}=\int {u_n}^*(\vec{r})\hat{A}u_m(\vec{r})d^3r. \tag{2.2}$$

However, it is difficult to specify the precise state of the system due to relaxation processes, so we can describe the system using a statistical way by defining density matrix elements

$$\rho_{nm}=\sum_s p(s)C_m^{s*}C_n^s, \tag{2.3}$$

where $p(s)$ is the probability of the system staying in state s, which reflects our uncertainty to the system. The physical interpretation of density matrix elements is that the diagonal element ρ_{nn} gives the probability that the system is in energy eigenstate n; and off-diagonal element ρ_{mn} is the correlation between states n and m.

Then we can use the density matrix to calculate the expectation value of any observable quantity. From Eq. (2.2) and the definition of ρ_{mn} above, the expectation value of A is :

$$\overline{\langle A \rangle} = \sum_s p(s) \sum_{n,m} C_n^{s*}(t) C_m^s(t) A_{nm} = \sum_{m,n} \rho_{mn} A_{nm} = \sum_n (\hat{\rho}\hat{A})_{nn} = tr(\hat{\rho}\hat{A}), \qquad (2.4)$$

which is the trace of the product of density operator $\hat{\rho}$ and $\hat{A}$. Thus, the evolution of the expectation value goes to the time evolution of the density matrix. The time derivative of the density operator $\hat{\rho}$ is

$$\dot{\rho}_{nm} = \sum_s \frac{dp(s)}{dt} C_m^{s*} C_n^s + \sum_s p(s) \left(C_m^{s*} \frac{dC_n^s}{dt} + \frac{dC_m^{s*}}{dt} C_n^s \right). \qquad (2.5)$$

In addition, from the Schrödinger equation above, we can obtain

$$C_m^{s*} \frac{dC_n^s}{dt} = \frac{-i}{\hbar} C_m^{s*} \sum_\upsilon H_{n\upsilon} C_\upsilon^s;$$

$$\frac{dC_m^{s*}}{dt} C_n^s = \frac{i}{\hbar} C_n^s \sum_\upsilon H_{\upsilon m} C_\upsilon^{s*}.$$

As a result, the time evolution relation of the density matrix element resulting from interaction with Hamiltonian is :

$$\dot{\rho}_{nm} = \frac{i}{\hbar} \sum_\upsilon (\rho_{n\upsilon} H_{\upsilon m} - H_{n\upsilon} \rho_{\upsilon m}) = \frac{i}{\hbar} \left(\hat{\rho}\hat{H} - \hat{H}\hat{\rho} \right)_{nm} = \frac{-i}{\hbar} [\hat{H}, \hat{\rho}]_{nm}. \qquad (2.6)$$

However, many other effects such as collisions between different atoms, disorder effects and many-body interactions will have influence on density matrix element, which is characterized by the non-vanishing 1st term in Eq. (2.5) $\frac{dp(s)}{dt}$. One way to include these effects is introducing phenomenological relaxation terms into the time-evolution equation to describe the decay process:

$$\dot{\rho}_{nm} = \frac{-i}{\hbar}[\hat{H}, \hat{\rho}]_{nm} - \gamma_{nm}(\rho_{nm} - \rho_{nm}^{(eq)}), \tag{2.7}$$

The 2nd term on the right-hand side indicates ρ_{nm} decays to its equilibrium value $\rho_{nm}^{(eq)}$ in a rate γ_{nm}. From the physical point of view, $\gamma_{nm} = \gamma_{mn}$ and the equilibrium value of the off-diagonal element $\rho_{nm}^{(eq)}$ should be zero. For the diagonal matrix element ρ_{nn} which stands for the population of energy state n, the relaxation process can also be characterized by the population decay between higher energy level to lower level:

$$\dot{\rho}_{nn} = \frac{-i}{\hbar}[\hat{H}, \hat{\rho}]_{nn} + \sum_{E_m > E_n} \Gamma_{nm}\rho_{mm} - \sum_{E_m < E_n} \Gamma_{mn}\rho_{nn}, \tag{2.8}$$

where Γ_{nm} is the decay rate per atom between energy level n and m. Usually, the coherent relaxation term is very difficult to express due to many relaxation effects in the material, therefore relaxation term or the corresponding decay rate is usually measured from experiment. For example, for monolayer graphene in a magnetic field, optical transitions occur between the Landau levels. The coherent relaxation results from collision, disorder effects (ripples, topological lattice defects, impurity and self-doping), phonon interactions, many body carrier-carrier interactions, short-range interactions and so on. All of these effects will contribute to the decay rate γ_{nm} in the relaxation term. In order to measure the decay rate between different Landau energy states γ_{nm}, the infrared (IR) spectroscopy technique is used. We can measure

the transition half-width in the IR absorption spectra to calculate the corresponding damping rate, which will be discussed in the following paragraph.

In most cases, the time evolution equation of density matrix cannot be exactly solved, so the perturbation technique is always used. For the above Hamiltonian $\hat{H} = \hat{H}_0 + \hat{V}(t)$, $\hat{V}(t)$ describes the interaction, for example, the interaction between the material and incident optical field, which can be treated as a perturbation term. Then the phenomenological equation for the density matrix element ρ_{nm} goes to

$$\dot{\rho}_{nm} = \frac{-i}{\hbar}[\hat{H}_0, \hat{\rho}]_{nm} + \frac{-i}{\hbar}[\hat{V}(t), \hat{\rho}]_{nm} - \gamma_{nm}(\rho_{nm} - \rho_{nm}^{(eq)}),$$

where

$$[\hat{H}_0, \hat{\rho}]_{nm} = (\hat{H}_0\hat{\rho} - \hat{\rho}\hat{H}_0)_{nm} = \sum_{\mu} \left(H_{n\mu}^0 \rho_{\mu m} - \rho_{n\mu} H_{\mu m}^0 \right) = (E_n - E_m)\rho_{nm}.$$

As a result, the density motion equation is represented by:

$$\dot{\rho}_{nm} = \frac{-i}{\hbar}(E_n - E_m)\rho_{nm} + \frac{-i}{\hbar}[\hat{V}(t), \hat{\rho}]_{nm} - \gamma_{nm}(\rho_{nm} - \rho_{nm}^{(eq)}). \tag{2.9}$$

Using the formal perturbation method, define $V(t) = sV(t)$ and

$$\rho_{nm} = \rho_{nm}^{(0)} + s\rho_{nm}^{(1)} + s^2\rho_{nm}^{(2)} + \ldots,$$

where $\rho_{nm}^{(N)}$ denotes the Nth order correction to the density matrix element. So we can reconstruct the time evolution equation of ρ_{nm} as follows:

$$\begin{aligned} \dot{\rho}_{nm}^{(0)} &= -i\omega_{nm}\rho_{nm}^{(0)} - \gamma_{nm}(\rho_{nm}^{(0)} - \rho_{nm}^{(eq)}) \quad ; \\ \dot{\rho}_{nm}^{(1)} &= -(i\omega_{nm} + \gamma_{nm})\rho_{nm}^{(1)} - \frac{i}{\hbar}[\hat{V}, \hat{\rho}^{(0)}]_{nm} \quad ; \end{aligned}$$

$$\dot{\rho}^{(2)}_{nm} = -(i\omega_{nm} + \gamma_{nm})\rho^{(2)}_{nm} - \frac{i}{\hbar}[\hat{V}, \hat{\rho}^{(1)}]_{nm} \quad ;$$

.....

Choose $\rho^{(0)}_{nm} = \rho^{(eq)}_{nm}$, and we can calculate higher order term step by step. The iteration formula is given:

$$\rho^{(N)}_{nm} = \int^{t} \frac{-i}{\hbar}[\hat{V}(t'), \hat{\rho}^{(N-1)}]_{nm} \exp\left[(i\omega_{nm} + \gamma_{nm}) \cdot (t' - t)\right] dt'. \tag{2.10}$$

As an application of the perturbation solution of density matrix elements, we can calculate the material's optical response in different orders. For example, $\rho^{(1)}$ describe its linear response, and the higher order corrections characterize the nonlinear optical response of the material. These expressions are valid in discrete energy systems (e.g. Landau level system) as well as continuous energy systems, which play important role in calculating linear and nonlinear optical response of graphene material in and without magnetic field.

2.2 Linear optical response

Linear optical response of graphene in a magnetic field exhibits strong cyclotron resonance features, which mainly come from the inter-Landau-level transitions. Transitions between adjacent Landau levels in graphene fall into the mid-infrared to terahertz (THz) range for a magnetic field in the range 0.01-10 Tesla: $\hbar\omega_c \simeq 36\sqrt{B(\text{Tesla})}$ meV. Consider an incident classical optical field

$$\vec{E} = E(\omega) \exp(-i\omega t)\hat{e}$$

polarized in the x-y plane along vector $\hat{e}$. Let us define the left-hand circular polarization vector as $\hat{e}_{LHS} = [\hat{x} - i\hat{y}]/\sqrt{2}$ and the right-hand circular polarization vector

$\hat{e}_{RHS} = [\hat{x} + i\hat{y}]/\sqrt{2}$. To include the interaction with the optical field, we add its vector potential , $\vec{A}_{opt} = ic\vec{E}/\omega$, to the vector potential of the magnetic field in the generalized momentum operator $\hat{\vec{\pi}}$ in the Hamiltonian. This results in adding the interaction Hamiltonian $\hat{H}_{int}$ to $\hat{H}_0$(Eq. (1.14)), where

$$\hat{H}_{int} = \upsilon_F \hat{\vec{\sigma}} \cdot \frac{e}{c} \vec{A}_{opt} \tag{2.11}$$

Unlike the interaction Hamiltonian H_{int} for an electron with a parabolic dispersion, there are no higher order terms such as π^2 near the Dirac point in graphene, so that even for a relatively strong optical field the interaction Hamiltonian is still linear with respect to $\vec{A}_{opt}$. Furthermore, H_{int} does not contain the momentum operator; it is simply determined by the Pauli matrix vector $\hat{\vec{\sigma}}$. The matrix element of the optical transition between Landau levels is given by

$$\langle m|\hat{H}_{int}|n\rangle = \frac{i\upsilon_F}{\omega} \langle m|\sigma_x\hat{x} + \sigma_y\hat{y}|n\rangle \cdot \vec{E},$$

where $|m\rangle, |n\rangle$ denote Landau level with energy index m and n (Eq. (1.15)). $\langle m|\sigma_x\hat{x} + \sigma_y\hat{y}|n\rangle$ is

$$\sqrt{2}C_m C_n (-i)^{|m|+|n|-1} \left\{ \mathrm{sgn}(m)\langle\phi_{|m|-1}|\phi_{|n|}\rangle \cdot \hat{e}_{LHS} + \mathrm{sgn}(n)\langle\phi_{|m|}|\phi_{|n|-1}\rangle \cdot \hat{e}_{RHS} \right\}.$$

Since ϕ_n are orthogonal, the above expression is nonzero only when

$$|m| - 1 = |n| \quad or \quad |m| = |n| - 1.$$

As a result, the selection rule for the allowed transitions turns out to be

$$\Delta|n| = \pm 1, \tag{2.12}$$

where n is the energy quantum number. Denoting f and i as the quantum numbers of the final and initial state, we conclude that $\hat{e}_{RHS}$ photons are absorbed when $|f| = |i| - 1$ while an absorption of a $\hat{e}_{LHS}$ photon leads to the transition $|f| = |i| + 1$ (as shown in Fig. 2.1). Comparing with a typical selection rule for inter-Landau level transitions in a traditional 2D system, $\Delta n = \pm 1$, the transitions with Δn greater than 1 are allowed in graphene, for example, from $i = -1$ to $f = 2$, which leads to an efficient resonant nonlinear mixing. Mid/far-infrared optical absorption between Landau levels in monolayer and multilayer graphene has been extensively studied theoretically and in experiments[60][70][71][73][74][75][76].

In order to calculate the 2D optical polarization using density-matrix formalism, we need to know the dipole moment matrix associated with inter-Landau level transitions. To calculate this, we first evaluate the commutator

$$[\vec{r}, \hat{H}] = [\vec{r}, \upsilon_F \hat{\vec{\sigma}} \cdot \hat{\vec{p}}] + [\vec{r}, \upsilon_F \hat{\sigma} \cdot \frac{e}{c} \vec{A}].$$

The second term on the right-hand side is zero because $\vec{A}$ is a function of $\vec{r}$. So the commutator of $\hat{\vec{r}}$ and the Hamiltonian is

$$[\vec{r}, \hat{H}] = \upsilon_F \hat{\vec{\sigma}} \cdot [\vec{r}, \hat{\vec{p}}] = i\hbar \upsilon_F \hat{\vec{\sigma}}.$$

Choosing the eigenstates of $\hat{H}$ as the basis, we obtain

$$\langle m|[\vec{r}, \hat{H}]|n\rangle = \langle m|\vec{r}\hat{H}|n\rangle - \langle m|\hat{H}\vec{r}|n\rangle = (\varepsilon_n - \varepsilon_m)\langle m|\vec{r}|n\rangle,$$

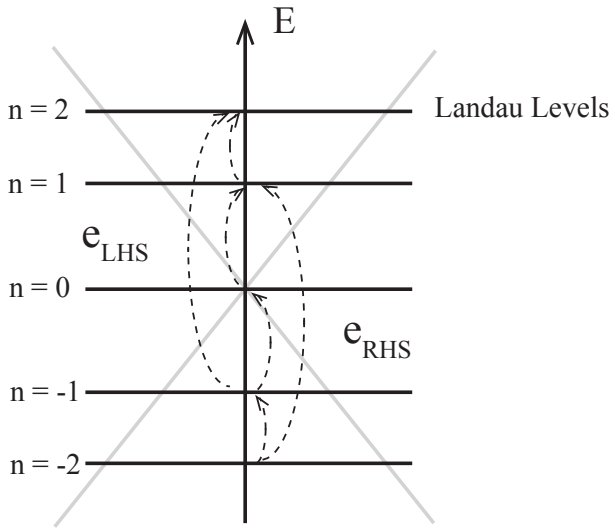

Figure 2.1: Allowed inter-LL transitions in graphene, $\hat{e}_{LHS}$ photon is absorbed for $|n| \to |n|+1$, while $\hat{e}_{RHS}$ photon is absorbed when $|n| \to |n|-1$.

where ε_n and ε_m are the eigen energies of states $|n\rangle$ and $|m\rangle$. So the dipole matrix element of a closed system is defined as

$$\vec{\mu}_{mn} = e \cdot \langle m|\vec{r}|n\rangle = \frac{i\hbar e}{\varepsilon_n - \varepsilon_m}\langle m|\upsilon_F\hat{\vec{\sigma}}|n\rangle. \tag{2.13}$$

Similarly to the matrix elements of the interaction Hamiltonian $\langle m|\hat{H}_{int}|n\rangle$, the dipole matrix elements are determined by elements of the Pauli matrix $\langle m|\hat{\sigma}|n\rangle$. In particular, $\vec{\mu}_{mn}$ is nonzero when $|m| = |n| \pm 1$. Using the wavefunction in Eq. (1.15), the analytic expression for the dipole moment element is derived:

$$\vec{\mu}_{mn} = \frac{i\sqrt{2}\hbar e\upsilon_F C_m^* C_n (-1)^{|m|-1} i^{|m|+|n|-1}}{\varepsilon_n - \varepsilon_m} \times$$

$$\left\{\mathrm{sgn(m)}\delta_{|m|-1,|n|}\hat{e}_{LHS} - \mathrm{sgn(n)}\delta_{|m|,|n|-1}\hat{e}_{RHS}\right\} \tag{2.14}$$

Recall the first-order (linear) solution of the density matrix element can be calculated from the iteration formula Eq. (2.10) and Eq. (2.11):

$$\rho^{(1)}_{nm} = \int_0^t \frac{-i}{\hbar}[\hat{H}_{int}(t'), \hat{\rho}^{(eq)}]_{nm} \exp\left[(i\omega_{nm} + \gamma_{nm}) \cdot (t' - t)\right] dt', \tag{2.15}$$

where

$$\begin{aligned}
[\hat{H}_{int}(t'), \hat{\rho}^{(eq)}]_{nm} &= \sum_{\upsilon} \left(\tilde{\vec{\mu}}_{n\upsilon}\rho^{(eq)}_{\upsilon m} - \rho^{(eq)}_{n\upsilon}\tilde{\vec{\mu}}_{\upsilon m}\right) \cdot \tilde{E}(t') \\
&= \left(\rho^{(eq)}_{mm} - \rho^{(eq)}_{nn}\right) \tilde{\vec{\mu}}_{nm} \cdot \tilde{E}(t').
\end{aligned}$$

This yields the 2D first-order polarization in the form

$$\begin{aligned}
&\tilde{P}^{(1)}(\omega) = N \cdot \mathrm{tr}\left(\hat{\rho}^{(1)}\hat{\mu}\right) \\
= \quad & N \sum_{nm} \frac{\rho^{(eq)}_{mm} - \rho^{(eq)}_{nn}}{\hbar} \cdot \frac{\left(\tilde{\vec{\mu}}_{nm} \cdot \hat{e}\right) \vec{\mu}_{mn}}{(\omega_{nm} - \omega) - i\gamma_{nm}} E(\omega) \exp\left(-i\omega t\right).
\end{aligned} \tag{2.16}$$

Here we have defined

$$\tilde{\vec{\mu}} \equiv \frac{iev_F}{\omega}\vec{\sigma}, \quad \langle m|\tilde{\vec{\mu}}|n\rangle \equiv \frac{iev_F}{\omega}\langle m|\vec{\sigma}|n\rangle;$$

N is the 2D (sheet) electron density of graphene, which is $n_s n_\upsilon N_\Phi = 2/(\pi l_c^2)$ where $n_s = 2$ and $n_\upsilon = 2$ are spin and valley degeneracy. The corresponding linear susceptibility tensor is then given by:

$$\chi^{(1)}_{ij}(\omega) = N \sum_{nm} \frac{\rho^{(eq)}_{mm} - \rho^{(eq)}_{nn}}{\hbar} \frac{\tilde{\vec{\mu}}^{j}_{nm}\vec{\mu}^{i}_{mn}}{(\omega_{nm} - \omega) - i\gamma_{nm}} \tag{2.17}$$

For a left-hand circularly polarized optical field, the circular polarization vector $\hat{e}$ is $\hat{e}_{LHS} = [\hat{x} - i\hat{y}]/\sqrt{2}$, and the term $\left(\tilde{\vec{\mu}}_{nm} \cdot \hat{e}\right)$ in the above expression is nonzero only when $|n|=|m|-1$. On the other hand, for a right-hand circularly polarized optical field the term is nonzero only when $|m|=|n|-1$. This corresponds to the polarization selection rules that were already derived above. We here explicitly give the linear optical susceptibility for left/right-hand circularly polarized optical field:

$$\begin{aligned}
\chi^{(1)}(\omega, \hat{e}_{LHS}) &= \sum_{|n|=|m|-1} \frac{-4C_m^2 C_n^2 e^2 \upsilon_F^2}{\pi l_c^2 \hbar \omega \omega_{nm}} \cdot \frac{\rho_{mm}^{(eq)} - \rho_{nn}^{(eq)}}{\omega_{nm} - \omega - i\gamma_{nm}} \\
\chi^{(1)}(\omega, \hat{e}_{RHS}) &= \sum_{|m|=|n|-1} \frac{-4C_m^2 C_n^2 e^2 \upsilon_F^2}{\pi l_c^2 \hbar \omega \omega_{nm}} \cdot \frac{\rho_{mm}^{(eq)} - \rho_{nn}^{(eq)}}{\omega_{nm} - \omega - i\gamma_{nm}}
\end{aligned} \tag{2.18}$$

Different from the constant high-frequency absorbance of monolayer graphene at zero magnetic field, the absorption coefficient in a high magnetic field shows a series of peaks due to inter-Landau-level transitions. From the standard expression for a weak absorption,

$$\alpha \simeq \frac{4\pi\omega}{c} \mathrm{Im}[\chi^{(1)}(\omega)]. \tag{2.19}$$

Combining with Eq. (2.18), we can write the absorption coefficient of monolayer graphene for left/right-hand circularly polarized optical field separately:

$$\begin{aligned}
\alpha(\omega, \hat{e}_{LHS}) &= \sum_{|n|=|m|-1} \frac{-16C_m^2 C_n^2 e^2 \upsilon_F^2 \gamma_{nm}}{l_c^2 \hbar c \omega_{nm}} \cdot \frac{\rho_{mm}^{(eq)} - \rho_{nn}^{(eq)}}{(\omega_{nm} - \omega)^2 + \gamma_{nm}^2} \\
\alpha(\omega, \hat{e}_{RHS}) &= \sum_{|m|=|n|-1} \frac{-16C_m^2 C_n^2 e^2 \upsilon_F^2 \gamma_{nm}}{l_c^2 \hbar c \omega_{nm}} \cdot \frac{\rho_{mm}^{(eq)} - \rho_{nn}^{(eq)}}{(\omega_{nm} - \omega)^2 + \gamma_{nm}^2}
\end{aligned} \tag{2.20}$$

The above results agree with the absorption coefficient calculated using the Keldysh's Green function approach[60]. The Faraday rotation angle can be calculated in a

similar way. In the limit $\frac{\omega_c e^2}{\gamma \hbar c} \ll 1$, the standard formula for Faraday rotation is:

$$\Delta\theta \simeq \frac{4\pi\omega}{c}\mathrm{Re}[\chi^{(1)}(\omega)]. \tag{2.21}$$

The Faraday rotation angle for left/right-hand circularly polarized optical incidence is then given by:

$$\begin{aligned}
\Delta\theta(\omega, \hat{e}_{LHS}) &= \sum_{|n|=|m|-1} \frac{-16C_m^2 C_n^2 e^2 \upsilon_F^2}{l_c^2 \hbar c \omega_{nm}} \cdot \frac{(\rho_{mm}^{(eq)} - \rho_{nn}^{(eq)})(\omega_{nm} - \omega)}{(\omega_{nm} - \omega)^2 + \gamma_{nm}^2} \\
\Delta\theta(\omega, \hat{e}_{RHS}) &= \sum_{|m|=|n|-1} \frac{-16C_m^2 C_n^2 e^2 \upsilon_F^2}{l_c^2 \hbar c \omega_{nm}} \cdot \frac{(\rho_{mm}^{(eq)} - \rho_{nn}^{(eq)})(\omega_{nm} - \omega)}{(\omega_{nm} - \omega)^2 + \gamma_{nm}^2}
\end{aligned} \tag{2.22}$$

Note that the standard formula for weak absorption and Faraday rotation is accurate in the limit $\frac{\omega_c e^2}{\gamma \hbar c} \ll 1$, which is valid in monolayer graphene situation. In other 2D electron systems like the surface state of a topological insulator, we have to solve Maxwell's equations strictly together with polarization-induced surface current, because the relaxation rate γ is observed to be much smaller than that in graphene in recent experiments[36][37].

2.3 Nonlinear optical response

The classical and semi-classical approach[77][78][79] for graphene nonlinear optics can be applied only to electrons in a low magnetic field that occupy highly excited Landau levels $n \gg 1$, where energy and momentum quantization can be neglected. Compared with the classical treatment, quantum-mechanical density-matrix description presents a more convenient way to characterize the nonlinear response of graphene in quantizing magnetic fields and strong optical fields. Due to unique optical selection rules for massless electrons near the Dirac point, one can implement a nonlinear interaction in which all optical fields are resonant to allowed optical

transitions. The resulting magnitude of $\chi^{(3)}$ turns out to be extremely large, of the order of 0.1 esu at mid/far-infrared wavelengths in the field of several tesla. A similar strategy of a completely resonant nonlinear wave mixing has been implemented in asymmetric coupled quantum well systems, where one can increase the dipole moment of an intersubband transition involving a large change in the energy quantum number n by an appropriate band structure design[80][81][82][83][84][85]. However, the resulting third-order nonlinearity was still several orders of magnitude lower than in graphene for the same spectral range. We here study a specific example of

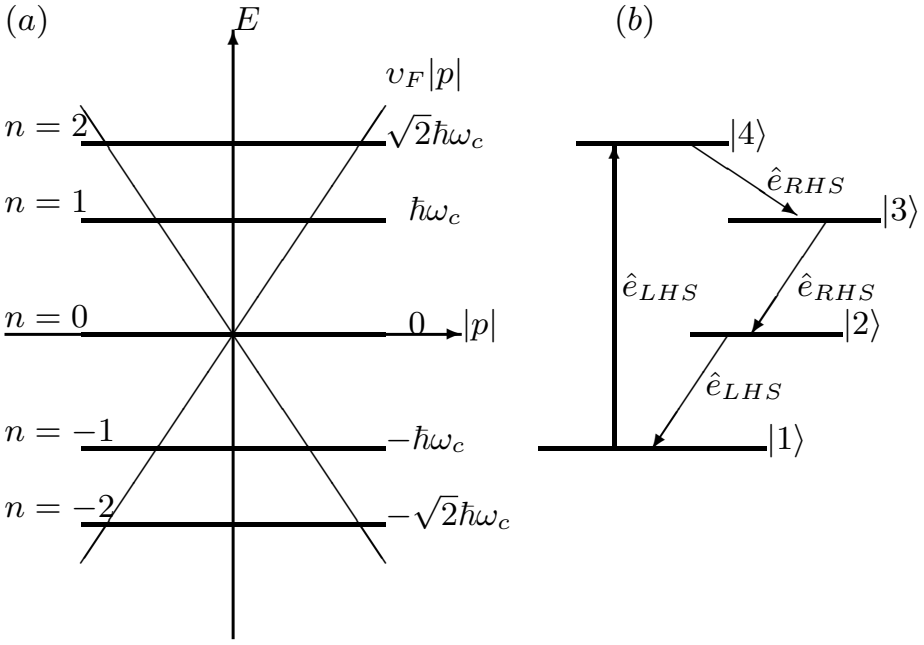

Figure 2.2: Landau levels near the Dirac point superimposed on the electron dispersion without the magnetic field $E = \pm v_F|p|$. (b): A scheme of the four-wave mixing process in the four-level system of Landau levels with energy quantum numbers $n = -1, 0, +1, +2$ that are renamed to states 1 through 4 for convenience.

the nonlinear optical interaction, namely the four-wave mixing. Consider a strong bichromatic field

$$\vec{E} = \vec{E}_1 \exp(-i\omega_1 t) + \vec{E}_2 \exp(-i\omega_2 t) + \text{c.c.}$$

normally incident on the graphene layer. Here ω_1 is nearly resonant with the transition from $n = -1$ to $n = 2$ and $\vec{E}_1$ has left circular polarization. The frequency ω_2 is nearly resonant with the transition from $n = 0$ to $n = \pm 1$ and $\vec{E}_2$ has linear polarization, so that it couples both to transition $-1 \to 0$ and $0 \to 1$, as shown in Fig. 2.2. As a result of the four-wave mixing interaction, the right-circularly polarized field $\vec{E}_3$ at frequency $\omega_3 = \omega_1 - 2\omega_2$ nearly resonant with the transition from $n = 2$ to $n = 1$ is generated. The frequencies involved in the four-wave mixing fall into the mid-infrared and THz region in the magnetic field of a few Tesla, For example, at $B = 3\text{T}$, the nonlinear signal is generated at a wavelength of 48 μm in the presence of pump fields at wavelengths 8 and 20 μm.

The eigenfunctions of these four energy levels are

$$\begin{aligned}
|1\rangle &= \frac{1}{\sqrt{2L}} \exp(-ik_{y_1} y) \begin{pmatrix} -\phi_0 \\ i\phi_1 \end{pmatrix}; \\
|2\rangle &= \frac{1}{\sqrt{L}} \exp(-ik_{y_2} y) \begin{pmatrix} 0 \\ \phi_0 \end{pmatrix}; \\
|3\rangle &= \frac{1}{\sqrt{2L}} \exp(-ik_{y_3} y) \begin{pmatrix} \phi_0 \\ i\phi_1 \end{pmatrix}; \\
|4\rangle &= \frac{1}{\sqrt{2L}} \exp(-ik_{y_4} y) \begin{pmatrix} i\phi_1 \\ -\phi_2 \end{pmatrix}.
\end{aligned} \tag{2.23}$$

From Eq. (2.14), we can directly calculate the dipole moment matrix of this 4-level system

$$\vec{\mu} = \frac{e\upsilon_F}{\sqrt{2}\omega_c} \begin{pmatrix} 0 & -i\hat{x} - \hat{y} & 0 & \frac{i\hat{x}-\hat{y}}{2+\sqrt{2}} \\ i\hat{x} - \hat{y} & 0 & i\hat{x} - \hat{y} & 0 \\ 0 & -i\hat{x} - \hat{y} & 0 & \frac{i\hat{x}-\hat{y}}{2-\sqrt{2}} \\ \frac{-i\hat{x}-\hat{y}}{2+\sqrt{2}} & 0 & \frac{-i\hat{x}-\hat{y}}{2-\sqrt{2}} & 0 \end{pmatrix} \tag{2.24}$$

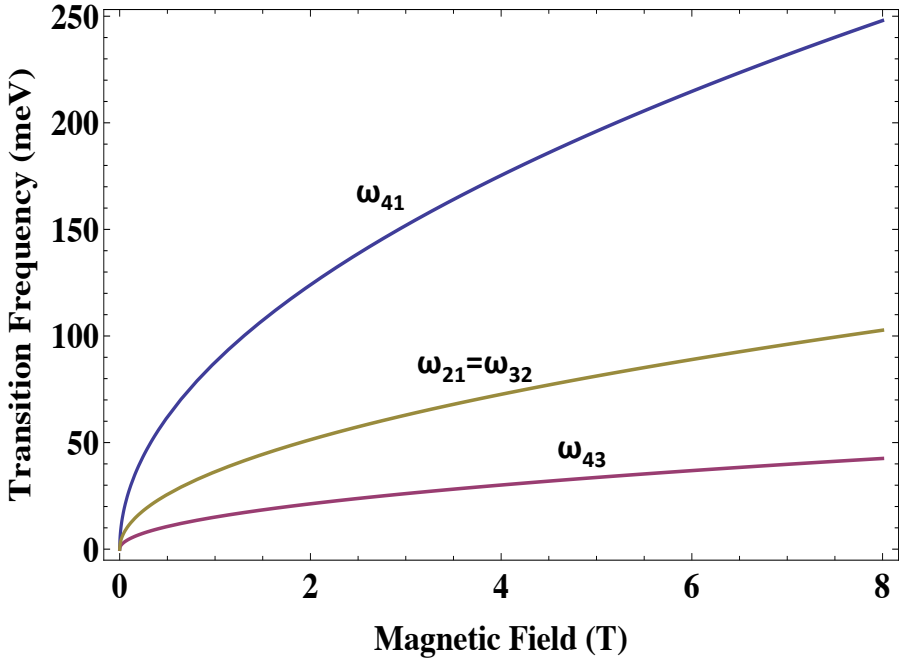

Figure 2.3: Transition frequencies in the 4-level graphene system shown in Fig. 1(b). ω_{mn} indicates the transition frequency between levels m and n.

Truncating the master equation Eq. (2.9) into the 4-level system shown above, and introducing slowly varying off-diagonal elements of the density matrix as $\rho_{41} = \sigma_{41}e^{-i\omega_1 t}$, $\rho_{41} = \sigma_{43}e^{-i\omega_3 t}$, $\rho_{32} = \sigma_{32}e^{-i\omega_2 t}$, and $\rho_{21} = \sigma_{21}e^{-i\omega_2 t}$ one can obtain the

following set of equations for the amplitudes σ_{nm} in the steady state and in the rotating wave approximation:

$$\begin{aligned}
i\Gamma_{21}\sigma_{21} &= \Omega_{21}n_{21} - \Omega_{32}^{*}\sigma_{31} + \Omega_{41}\sigma_{24} \\
i\Gamma_{32}\sigma_{32} &= \Omega_{32}n_{32} - \Omega_{43}^{*}\sigma_{42} + \Omega_{21}^{*}\sigma_{31} \\
i\Gamma_{43}\sigma_{43} &= \Omega_{43}n_{43} - \Omega_{41}\sigma_{13} + \Omega_{32}^{*}\sigma_{42} \\
i\Gamma_{31}\sigma_{31} &= \Omega_{21}\sigma_{32} + \Omega_{41}\sigma_{34} - \Omega_{32}\sigma_{21} - \Omega_{43}^{*}\sigma_{41} \\
i\Gamma_{42}\sigma_{42} &= \Omega_{21}^{*}\sigma_{41} + \Omega_{32}\sigma_{43} - \Omega_{43}\sigma_{32} - \Omega_{41}\sigma_{12} \\
i\Gamma_{41}\sigma_{41} &= \Omega_{41}n_{41} + \Omega_{21}\sigma_{42} - \Omega_{43}\sigma_{31}.
\end{aligned} \tag{2.25}$$

Here the Rabi frequencies are defined as $\Omega_{ij} = \vec{E}_{ij} \cdot \tilde{\vec{\mu}}_{ij}/\hbar$ and the population differences are $n_{ij} = \rho_{ii} - \rho_{jj}$. The notation for the field amplitudes is as follows: $\vec{E}_{41} = \vec{E}_1$, $\vec{E}_{21}$ is the right circularly polarized component of $\vec{E}_2$, and $\vec{E}_{32}$ is the left circularly polarized component of $\vec{E}_2$. The complex dephasing $\Gamma_{41} = \gamma_{41} + i(\omega_{41} - \omega_1)$ and similarly for other transitions; all detunings from resonance are small. If the incident field is not strong enough to perturb the populations, the population differences n_{mn} are constant in Eqs. (2.25). As a result, the off-diagonal density matrix elements such as σ_{43} can be solved analytically and written as an expansion in powers of the pump fields:

$$\begin{aligned}
\sigma_{43} &= \frac{\Omega_{43}}{i\Gamma_{43}}n_{43} - \frac{\Omega_{41}\Omega_{21}^{*}\Omega_{32}^{*}}{i^3\Gamma_{43}\Gamma_{31}^{*}\Gamma_{32}^{*}}n_{32} + \frac{\Omega_{41}\Omega_{21}^{*}\Omega_{32}^{*}}{i^3\Gamma_{43}\Gamma_{31}^{*}\Gamma_{21}^{*}}n_{21} + \frac{\Omega_{41}\Omega_{21}^{*}\Omega_{32}^{*}}{i^3\Gamma_{43}\Gamma_{42}\Gamma_{41}}n_{41} \\
&+ \frac{\Omega_{41}\Omega_{21}^{*}\Omega_{32}^{*}}{i^3\Gamma_{43}\Gamma_{42}\Gamma_{21}^{*}}n_{21} + \frac{|\Omega_{41}|^2\Omega_{43}}{i^3\Gamma_{43}\Gamma_{31}^{*}\Gamma_{41}^{*}}n_{41} + ...
\end{aligned} \tag{2.26}$$

The first term on the right-hand side describes the linear absorption and the next four

terms describe the 3rd order nonlinear optical response; the higher-order terms are dropped. Note that the last term on the right-hand side corresponds to a stimulated Raman scattering of the pump field E_{41} into the signal field E_{43}, which we will consider later.

The optical polarization at the frequency ω_3 of the nonlinear signal in the rotating wave approximation is given by

$$\vec{P}(\omega_3) = N \cdot \sigma_{43}\vec{\mu}_{43}e^{-i\omega_3 t} + c.c.$$

Below we investigate different nonlinear effects contained in Eq. (2.26). Consider first the four-wave mixing interaction $\omega_1 - 2\omega_2 \Rightarrow \omega_3$, described by the second through fourth terms on the right hand side of Eq. (2.26). Substituting the expression for σ_{43} into $\vec{P}(\omega_3)$, and keeping only these three terms will lead to the third-order nonlinear susceptibility corresponding to the four-wave mixing:

$$\chi^{(3)}(\omega_3) = \frac{N\mu_{43}\tilde{\mu}_{41}\tilde{\mu}^*_{32}\tilde{\mu}^*_{21}}{(i\hbar)^3\Gamma_{43}}\left(\frac{\rho_{22}-\rho_{33}}{\Gamma^*_{31}\Gamma^*_{32}} + \frac{\rho_{22}-\rho_{11}}{\Gamma^*_{31}\Gamma^*_{21}} - \frac{\rho_{11}-\rho_{44}}{\Gamma_{42}\Gamma_{41}} + \frac{\rho_{22}-\rho_{11}}{\Gamma_{42}\Gamma^*_{21}}\right) \quad (2.27)$$

A numerical estimate of the order of magnitude of $\chi^{(3)}$ is obtained by assuming that all incident fields are in exact resonance, so that the detuning factors $\Gamma_{ij} = \gamma_{ij} = \gamma$ are real numbers and all dephasing rates are the same. We also assume for definiteness that state 1 is fully occupied while states 2, 3 and 4 are empty, which means $\rho_{11} = 1, \rho_{22} = \rho_{33} = \rho_{44} = 0$. Then the expression for $\chi^{(3)}$ is further simplified into

$$\chi^{(3)}(\omega_3) \sim \frac{3N\mu_{43}\tilde{\mu}_{41}\tilde{\mu}_{32}\tilde{\mu}_{21}}{(\hbar\gamma)^3}. \quad (2.28)$$

This expression contains a 2D electron density N and is a 2D (surface) susceptibility. To convert it into the bulk susceptibility for comparison with other materials, we can

divide it by the thickness of one monolayer $\Delta z \sim 3$ Å. Taking a reasonable value for the dephasing rate, $\gamma = 3 \times 10^{13}$ s^{-1}[76], the bulk weak-field susceptibility $\chi^{(3)}_{3D} \sim 0.37\,(1/B(T))$ esu $= 5 \times 10^{-9}\,(1/B(T))$ m^2/V^2. Here the magnetic field is measured in tesla. This is by far the strongest nonlinearity as compared to any material we know. Of course for a monolayer graphene the notion of bulk susceptibilities does not make much sense and we use it only for comparison with bulk materials. All results below contain only the 2D (surface) susceptibilities.

When the incident fields increase in intensity, they start affecting populations on each level. In this case Eqs. (2.25) have to be solved together with the equations for diagonal components of the density matrix. Introducing phenomenological transition times T_{ij} between levels i and j, we can write these equations as

$$\begin{aligned}
\frac{dn_1}{dt} &= \frac{n_2}{T_{21}} + \frac{n_3}{T_{31}} + \frac{n_4}{T_{41}} - i\left(\Omega_{21}\sigma_{12} - \Omega_{12}\sigma_{21} + \Omega_{41}\sigma_{14} - \Omega_{14}\sigma_{41}\right) \\
\frac{dn_2}{dt} &= \frac{n_3}{T_{32}} + \frac{n_4}{T_{42}} - \frac{n_2}{T_{21}} - i\left(\Omega_{12}\sigma_{21} - \Omega_{21}\sigma_{12} + \Omega_{32}\sigma_{23} - \Omega_{23}\sigma_{32}\right) \\
\frac{dn_3}{dt} &= \frac{n_4}{T_{43}} - \frac{n_3}{T_{32}} - \frac{n_3}{T_{31}} - i\left(\Omega_{23}\sigma_{32} - \Omega_{32}\sigma_{23} + \Omega_{43}\sigma_{34} - \Omega_{34}\sigma_{43}\right) \\
n_1 &+ n_2 + n_3 + n_4 = 1.
\end{aligned} \tag{2.29}$$

It is convenient to normalize incident fields by their saturation values which determine the field strength at which the population at a given transition becomes significantly perturbed:

$$E^s_{21} = \frac{\hbar\sqrt{\gamma_{21}/T_{21}}}{\mu_{21}}; \quad E^s_{32} = \frac{\hbar\sqrt{\gamma_{32}/T_{32}}}{\mu_{32}}; \quad E^s_{41} = \frac{\hbar\sqrt{\gamma_{41}/T_{41}}}{\mu_{41}}. \tag{2.30}$$

Then the corresponding saturation Rabi frequencies are given by $\Omega^s_{nm} = \sqrt{\gamma_{nm}/T_{nm}}$.

We then introduce the dimensionless fields x, x', and y as

$$x = \Omega_{21}/\Omega_{21}^{s}; \quad x' = \Omega_{32}/\Omega_{32}^{s}; \quad y = \Omega_{41}/\Omega_{41}^{s}. \tag{2.31}$$

For estimation, we can simply assume that the relaxation times T_{nm} are the same, $T_{nm} \sim T$. Then the solution to the density matrix equation of motion depends on the fields through only two dimensionless factors x and y. In particular, the scaling Eq. (2.28) for $\chi^{(3)}(\omega_3)$ becomes

$$\chi^{(3)}(\omega_3) \sim \frac{N\mu_{43}\tilde{\mu}_{41}\tilde{\mu}_{32}\tilde{\mu}_{21}}{(\hbar\gamma)^3} \times f(x,y), \tag{2.32}$$

where $f(x,y)$ is a function of x and y shown in Fig. 2.4. It equals to 3 when incident fields are weak ($x, y \ll 1$), and quickly decreases as x and y become greater than one. The electric field of the generated signal is determined by the nonlinear polarization

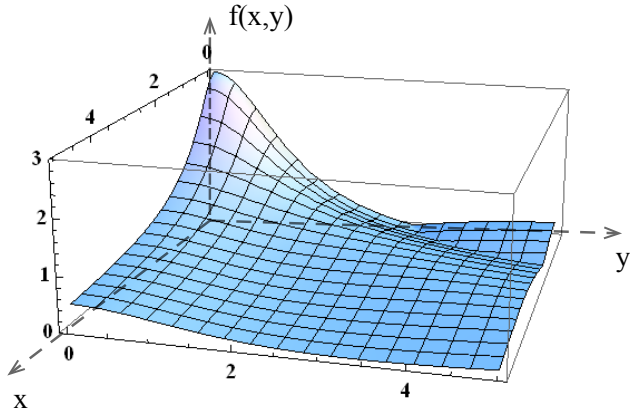

Figure 2.4: Contour plot of $f(x,y)$ as a function of normalized pump fields x and y.

$\vec{P}^{(3)}(\omega_3)$. From Maxwell's equations and neglecting the depletion of the pump fields, one can obtain

$$\frac{\partial \vec{E}}{\partial z} = i\frac{2\pi\omega}{c}\vec{P}^{(3)}_{3D}, \tag{2.33}$$

where $\vec{P}^{(3)}_{3D}$ is the 3D polarization(an average dipole moment per unit volume). For a thin layer of graphene one can integrate Eq. (2.33) over the thickness of the layer and obtain

$$E_3(\omega_3) = i \cdot \frac{2\pi\omega_3}{c}\chi^{(3)}(\omega_3)E_1(E_2^*)^2, \tag{2.34}$$

where $\chi^{(3)}$ is a 2D susceptibility. The magnitude of $|\vec{E}_3|$ grows with the pump at small pump intensities and decays at high intensities because of the decrease in $\chi^{(3)}$. It reaches a maximum at $x = 2.6$, $y = 1.56$. Of course, these particular numbers depend on the relative values of the relaxation times between the Landau levels. However, the general conclusion that the maximum nonlinear signal is reached when the pump fields are of the order of the saturation values remains true. For fixed $x, y \sim 1$, $\chi^{(3)}$ scales with the magnetic field as B^{-1}, whereas $E \sim E_{sat} \sim \sqrt{B}$. As a result, from Eq. (2.34), the maximum nonlinear signal scales with the magnetic field as

$$|E_3^{max}| \sim \omega_3\chi^{(3)}(\omega_3)|E_{sat}|^3 \sim \sqrt{B}\frac{1}{B} \cdot (\sqrt{B})^3 \sim B. \tag{2.35}$$

If we define intensity as $I = c|E|^2/8\pi$, the intensity of the generated signal is related to the incident field intensities as

$$I_3(\omega_3) = \left(\frac{16\pi^2\omega_3}{c^2}\right)^2 |\chi^{(3)}|^2 I_1(\omega_1)(I_2(\omega_2))^2. \tag{2.36}$$

Fig. 2.5(a) shows the plot of I_3 as a function of the pump intensity I_2 when the second pump intensity I_1 is tied to I_2 by the optimal condition $y = (1.56/2.6)x = 0.6x$. The conversion efficiency in the magnetic field of 1-10 T is $I_3/I_2 \sim 10^{-5} - 10^{-6}$. This

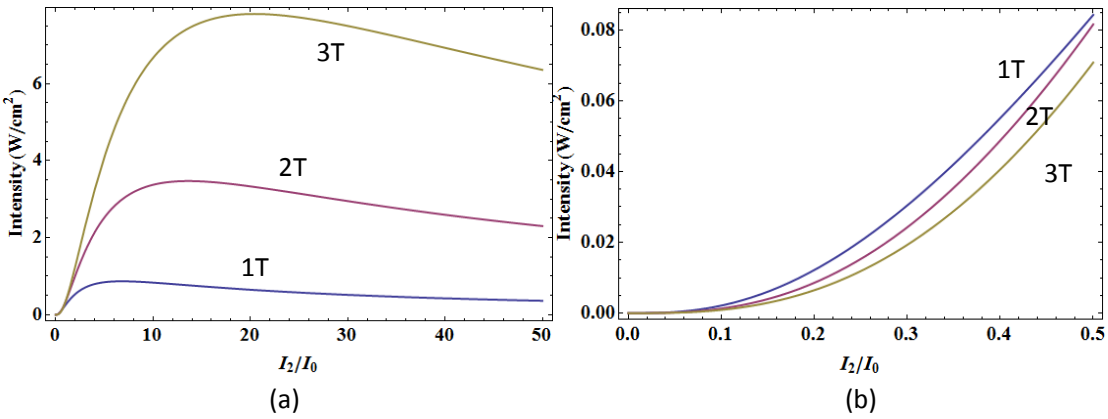

Figure 2.5: (a) Intensity of the 4-wave mixing signal as a function of the intensity of the pump field E_2 normalized by $I_0 = c|E_{\rm sat}|^2/8\pi \simeq 2.2 \times 10^5$ W/cm^2. The value of I_0 is the saturation intensity of the transition 1-2 calculated at $B = 1$ T and assuming that $1/T = \gamma = 3 \times 10^{13}$ s^{-1}. I_1 is set to satisfy $y = 0.6x$. (b) Enlargement of (a) near the origin, which shows the intensity of the 4-wave mixing signal for a weak pump field.

trend is reversed for a small incident pump intensity, when $\chi^{(3)} \sim 1/B$ and f(x, y) is nearly a constant. As a result, for weak pumps I_3 is higher in a smaller magnetic field, as illustrated in Fig. 2.5(b), which is the enlargement of Fig. 2.5(a) near the origin.

The very last term on the right-hand side of Eq. (2.26) that we previously omitted describes another interesting nonlinear process: stimulated Raman Stokes scattering of the pump field $E_1(\omega_1)$ into the field $E_3(\omega_3)$; see Fig. 2.6. Note that this term does not depend on the second pump field $E_2(\omega_2)$; therefore for this section we can put $E_2 = 0$. In this case the amplitude of the off-diagonal density matrix element σ_{43}, which determines the optical polarization at the frequency of the nonlinear signal,

becomes

$$\sigma_{43} = \left(\frac{\Omega_{43}}{i\Gamma_{43}} n_{43} + \frac{|\Omega_{41}|^2 \Omega_{43}}{i^3 \Gamma_{43} \Gamma_{31}^* \Gamma_{41}^*} n_{41} \right) / \left(1 + |\Omega_{41}|^2 / (\Gamma_{43} \Gamma_{31}^*) \right). \tag{2.37}$$

Here the complex detuning at the difference frequency is given by $\Gamma_{31} = \gamma_{31} + i(\omega_{31} - \omega_1 + \omega_3)$, whereas other detunings are still $\Gamma_{41} = \gamma_{41} + i(\omega_{41} - \omega_1)$ and $\Gamma_{43} = \gamma_{43} + i(\omega_{43} - \omega_3)$. Since the polarization $P(\omega_3)$ is proportional to the field E_3,

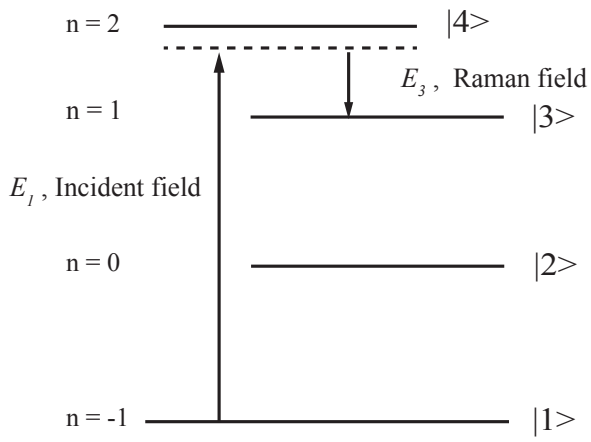

Figure 2.6: Raman Stokes scattering of the incident field E_1 into the signal E_3.

the small-signal solution to the wave equation Eq. (2.33) has an exponential form, $E_3 = E_0 \exp(gz)$, where g is given by

$$g = \frac{2\pi\omega_3 N_{3D} \mu_{43} \tilde{\mu}_{43}}{\hbar c \Gamma_{43}} \left(n_{43} - \frac{|\Omega_{41}|^2}{\Gamma_{31}^* \Gamma_{41}^*} n_{41} \right) \frac{1}{(1 + |\Omega_{41}|^2 / (\Gamma_{43} \Gamma_{31}^*))}, \tag{2.38}$$

and $N_{3D} = 2/(\Delta z \pi l_c^2)$ is the volume density of electrons in a layer of thickness Δz.

The real part of g gives the spectrum of the Raman gain. It is similar to the one derived for resonant Raman lasers in atomic and quantum-well systems [85, 86]. The gain peaks at the frequency of the two-photon resonance $\omega_1 - \omega_3 = \omega_{31}$. Its peak value increases when the pump frequency is tuned closer to the one-photon resonance $\omega_1 = \omega_{41}$.

To estimate the maximum gain, we assume exact resonance for the pump and Stokes fields with corresponding transition frequencies ω_{41} and ω_{43}, and take all dephasing rates to be the same, so that $\Gamma_{ij} \sim \gamma$. Then the gain factor is simplified to

$$g\Delta z \sim \frac{4\omega_3\mu_{43}^2}{\hbar\gamma c l_c^2}\left(n_{43} + \frac{|\Omega_{41}|^2}{\gamma^2}n_{14}\right) / \left(1 + |\Omega_{41}|^2/\gamma^2\right). \tag{2.39}$$

For a weak pumping $|\Omega_{41}|^2 \ll \gamma^2$, all population stays in the ground state of the system, $n_{14} \sim 1$ and $n_{43} \sim 0$. Then the maximum gain becomes

$$g\Delta z \sim \frac{4\omega_3\mu_{43}^2}{\hbar\gamma c l_c^2}\frac{|\Omega_{41}|^2}{\gamma^2}. \tag{2.40}$$

When expressed in usual dimensions cm/W for comparison with other materials, the Raman gain coefficient is really huge: around 20 cm/W in the magnetic field of 1 Tesla, and assuming $\gamma = 3 \times 10^{13}$ s^{-1}. This is many orders of magnitude higher gain than the one reported for resonant intersubband Raman scattering in conventional 2D semiconductor systems: asymmetric coupled quantum well systems or quantum cascade lasers [85, 86, 87, 88, 89].

For a stronger pump field, effects of the optical pumping and saturation become important. From the structure of the gain expression Eq. (2.39), it is clear that the gain reaches a maximum value when the pump field is of the order of the saturation value. This is a generic property of all resonant nonlinearities. For even higher fields,

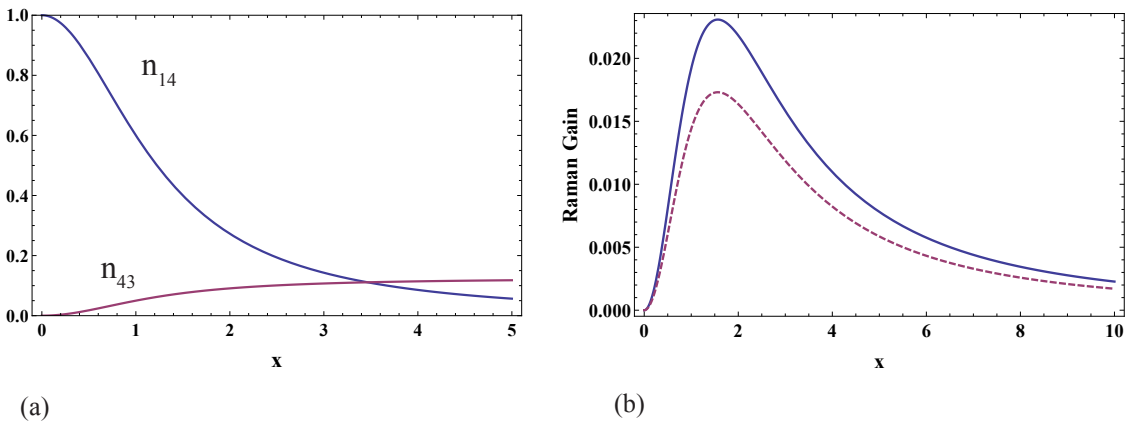

Figure 2.7: (a) Population differences as functions of the normalized pump field. (b) Gain $g\Delta z$ for one monolayer of graphene as a function of the normalized pump field in the magnetic field $B = 1$ T. Solid line: the total gain, dashed line: only the Raman part assuming $n_{43} = 0$.

the gain drops due to a decrease in n_{14} and an additional power-broadening term $1+|\Omega_{41}|^2/\gamma^2$ in the denominator. Using the same notation as in the previous section, we define the saturation field $E^s_{41} = \hbar\sqrt{\gamma_{41}/T_{41}}/\mu_{41}$ and the dimensionless pump field $x = E_1/E^s_{41}$. Taking all relaxation times to be the same, $T_{ij} \sim T$, all population differences and the gain factor can be calculated analytically. They are shown in Fig. 2.7 as functions of the normalized pump field. Note that for our choice of equal relaxation rates, the optical pumping to the upper state 4 results in the population inversion on the signal transition: $n_{43} > 0$. This leads to an additional contribution to the gain, as is clear from comparing the total gain and the Raman contribution. The peak gain of about 2 % is amazingly high for just one monolayer of the material. By stacking several layers and placing the system in a high-Q THz laser cavity one

can achieve a THz Raman laser with emission wavelength tunable by a magnetic field.

3. GENERATION OF ENTANGLED PHOTONS IN GRAPHENE*

To date, the most widely used method of generating entangled photons is based on spontaneous parametric down-conversion (SPDC) in a nonlinear crystal possessing a second-order nonlinearity [90][91]. In this process, a photon from a strong pump field at frequency ω_p splits into two signal photons, $\omega_p = \omega_1 + \omega_2$ which can be entangled in polarization, frequency, and wave vector. Entanglement in the polarization degree of freedom is the most convenient one for applications. Another way to generate quantum-correlated photons through a parametric nonlinear optical process is spontaneous four-wave mixing (SFWM) in the optical fibers, in which two pump photons are converted into two signal photons, $2\omega_p = \omega_1 + \omega_2$, utilizing a third-order nonlinearity of silica [92]. This process is obviously compatible with fiber communication technologies, although it does not directly lead to polarization entanglement. In order to achieve the latter, one needs to use two pumps with crossed polarizations and apply additional signal processing. In both SPDC and SFWM processes, the photon pair production efficiency is very low. An alternative approach utilizing the radiative decay of biexcitons in semiconductor quantum dots [93, 94, 95] allows photon pairs to be generated on demand but requires cooling down to liquid helium temperatures.

Graphene has unique electronic and optical properties stemming from linear, massless dispersion of electrons near the Dirac point and the chiral character of electron states[14, 22]. Magnetooptical properties of graphene and thin graphite layers are particularly unusual, showing multiple absorption peaks and unique selec-

*Reprinted with permission from Generation of Entangled Photons in Graphene in a Strong Magnetic Field by Mikhail Tokman, Xianghan Yao, and Alexey Belyanin, 2013. Phys. Rev. Lett., vol. 110, pp. 077404, Copyright [2013] by the American Physical Society.

tion rules for transitions between Landau levels [66, 60, 67, 69]. Recent progress in growing high-quality epitaxial graphene and graphite with high room-temperature mobility and strong magnetooptical response attracted a lot of interest and paved the way to new applications in the infrared optics and photonics [70, 71, 72]. The time is ripe to explore the nonlinear optical properties of a magnetized graphene and their applications. We have recently shown that graphene placed in a magnetic field posesses perhaps the highest infrared optical nonlinearity among known materials [67]. Here we argue that an extremely strong nonlinearity of graphene in combination with its unique selection rules open new avenues for generation of the nonclassical light states, in particular polarization-entangled photons[96].

3.1 Heisenberg density operator

The density-matrix formalism in the previous chapter is written in the Schrödinger picture. In order to study quantum optics phenomenon in graphene material, it is more convenient to rebuild the formalism in the Heisenberg picture. Consider electrons on discrete energy levels described by stationary states $|m\rangle$ and energy levels W_m. After introducing creation and annihilation operators of electrons

$$\hat{a}_m^\dagger|0\rangle = |m\rangle, \quad \hat{a}_n|n\rangle = |0\rangle, \tag{3.1}$$

one can define the density operator as

$$\hat{\pi}_{mn} = \hat{a}_n^\dagger \hat{a}_m, \tag{3.2}$$

which obeys the commutation relations $[\hat{\pi}_{pq}, \hat{\pi}_{mn}] = (\hat{\pi}_{mp}\delta_{nq} - \delta_{mp}\hat{\pi}_{qn})$. For the problem of the electromagnetic wave propagation in a continuous medium, it is more

convenient to deal with a coordinate-dependent density operator defined as

$$\hat{\rho}_{mn}(\vec{r},t) = \frac{1}{\Delta V_r}\sum_j \hat{a}^{\dagger}_{j,n}(t)\hat{a}_{j,m}(t), \tag{3.3}$$

where the index j numerates individual electrons and the summation is carried over all electrons within a small volume ΔV_r in the vicinity of a point with radius-vector $\vec{r}$. Assuming that the operators in different points of space commute with each other, the commutation relations of the coordinate-dependent density operator becomes obvious:

$$[\hat{\rho}_{qp}(\vec{r}),\hat{\rho}_{mn}(\vec{r}')] = \delta(\vec{r}-\vec{r}')\left(\hat{\rho}_{mp}\delta_{qn} - \delta_{mp}\hat{\rho}_{qn}(\vec{r})\right). \tag{3.4}$$

One can then write down the Heisenberg operator of any physical quantity $x(\vec{r},t)$ as

$$\hat{x} = x_{nm}\hat{\rho}_{mn}(\vec{r},t). \tag{3.5}$$

For example, the optical polarization is then given by $\hat{\mathbf{P}}(\vec{r},t) = \mathbf{d}_{nm}\hat{\rho}_{mn}$ where $\mathbf{d}_{mn}$ is the dipole moment matrix element. The evolution function of Heisenberg density operator is then described by the master equation:

$$\dot{\hat{\rho}}_{mn} = -\frac{i}{\hbar}\left(\hat{h}_{mv}\hat{\rho}_{vn} - \hat{\rho}_{mv}\hat{h}_{vn}\right) + \hat{R}_{mn}(\hat{\rho}_{mn}). \tag{3.6}$$

Here

$$\hat{h}_{nm} = W_n\delta_{nm} - d_{nm}\hat{E}(\vec{r},t)$$

is the matrix element of Hamiltonian operator $\hat{H} = \hat{h}_{nm}\hat{a}^{\dagger}_n\hat{a}_m$, which describes the interaction with electric field in dipole approximation. $\hat{R}_{mn}$ is the relaxation operator, which can be simply defined as $\hat{R}_{m\neq n} = -\gamma_{mn}\hat{\rho}_{mn}$. If we take random noise into consideration, one can simply add the Langevin noise operator $\hat{F}_{mn}$ into the evolution

equation.

$$\dot{\hat{\rho}}_{mn} = -\frac{i}{\hbar}\left(\hat{h}_{mv}\hat{\rho}_{vn} - \hat{\rho}_{mv}\hat{h}_{vn}\right) + \hat{R}_{mn}(\hat{\rho}_{mn}) + \hat{F}_{mn}. \tag{3.7}$$

The random noise operator satisfies $\hat{F}_{mn} = \hat{F}^{\dagger}_{nm}$ and $\langle \hat{F}_{mn} \rangle = 0$. This evolution equation will play important role in studying the mechanics of polarization-entangled photon generation in graphene material.

In order to find commutation and correlation relations for the noise operators, we start from Eq. (2) which can be rewritten as

$$[\hat{\rho}_{mn}(\mathbf{r}), \hat{\rho}_{nm}(\mathbf{r}')] = [\hat{\rho}_{mn}(\mathbf{r}), \hat{\rho}^{\dagger}_{mn}(\mathbf{r}')] = \delta(\mathbf{r} - \mathbf{r}')(\hat{\rho}_{nn}(\mathbf{r}) - \hat{\rho}_{mm}(\mathbf{r})). \tag{3.8}$$

From Eqs. (4) and (5) one can obtain the commutation relation

$$[\hat{F}_{mn}(\mathbf{r}, t), \hat{F}^{\dagger}_{mn}(\mathbf{r}', t')] = 2\gamma_{mn}(\hat{\rho}_{nn} - \hat{\rho}_{mm})\delta(t - t')\delta(\mathbf{r} - \mathbf{r}') \tag{3.9}$$

We will also need a similar relation for the spectral components of the noise operator,

$$\hat{F}_{mn}(t, \mathbf{r}) = \int_{-\infty}^{\infty} \hat{F}_{\omega;mn}(\mathbf{r}) e^{-i\omega t} d\omega, \hat{F}_{-\omega;mn} = \hat{F}^{\dagger}_{\omega;nm}, \tag{3.10}$$

which immediately follows from Eqs. (6) and (7):

$$[\hat{F}_{\omega;mn}(\mathbf{r}), \hat{F}^{\dagger}_{\omega';mn}(\mathbf{r}')] = \frac{\gamma_{mn}}{\pi}(\hat{\rho}_{nn} - \hat{\rho}_{mm})\delta(\omega - \omega')\delta(\mathbf{r} - \mathbf{r}') \tag{3.11}$$

The correlation function of the spectral components of the noise operator can be derived if we recall that for any stationary random delta-correlated process $x(\mathbf{r}, t)$

the spectral components of its Heisenberg operator satisfy the relation [97]

$$\frac{1}{2}\langle \hat{x}^{\dagger}_{\omega'}(\mathbf{r}')\hat{x}_{\omega}(\mathbf{r}) + \hat{x}_{\omega}(\mathbf{r})\hat{x}^{\dagger}_{\omega'}(\mathbf{r}')\rangle = \frac{1}{2}\sum_{n,m}\langle \hat{\rho}_{nn} + \hat{\rho}_{mm}\rangle |x_{mn}|^2 \delta(\omega_{mn} - \omega)\delta(\omega - \omega')\delta(\mathbf{r} - \mathbf{r}') \tag{3.12}$$

where $\omega_{mn} = (W_m - W_n)/\hbar$ and we assumed a negligible level broadening. Using Eqs. (3) and (4), one can obtain

$$\hat{x}_{\omega} = \sum_{m,n} \frac{x_{nm}\hat{F}_{\omega;mn}}{i(\omega_{mn} - \omega) + \gamma_{mn}}. \tag{3.13}$$

Taking into account Eq. (10) and the relationship

$$\left(\frac{\gamma_{mn}}{(\omega_{mn} - \omega)^2 + \gamma_{mn}^2}\right)_{\gamma_{mn}\to 0} \to \pi\delta(\omega_{mn} - \omega) \tag{3.14}$$

we obtain from Eq. (9):

$$\langle \hat{F}^{\dagger}_{\omega;mn}(\mathbf{r}')\hat{F}_{\omega';mn}(\mathbf{r}) + \hat{F}_{\omega';mn}(\mathbf{r})\hat{F}^{\dagger}_{\omega;mn}(\mathbf{r}')\rangle = \frac{\gamma_{mn}}{\pi}\langle \hat{\rho}_{nn} + \hat{\rho}_{mm}\rangle \delta(\omega - \omega')\delta(\mathbf{r} - \mathbf{r}') \tag{3.15}$$

Equations (9) and (12) give the correlation functions for the noise operator:

$$\left.\begin{aligned} \langle \hat{F}^{\dagger}_{\omega;mn}(\mathbf{r}')\hat{F}_{\omega';mn}(\mathbf{r})\rangle &= \frac{\gamma_{mn}}{\pi}\langle \hat{\rho}_{mm}\rangle \delta(\omega - \omega')\delta(\mathbf{r} - \mathbf{r}') \\ \langle \hat{F}_{\omega';mn}(\mathbf{r})\hat{F}^{\dagger}_{\omega;mn}(\mathbf{r}')\rangle &= \frac{\gamma_{mn}}{\pi}\langle \hat{\rho}_{nn}\rangle \delta(\omega - \omega')\delta(\mathbf{r} - \mathbf{r}') \end{aligned}\right\} \tag{3.16}$$

If the system is in thermal equilibrium, i.e.$\langle \hat{\rho}_{nn}\rangle / \langle \hat{\rho}_{mm}\rangle = \exp(\hbar\omega_{mm}/k_B T)$, it follows from Eq. (12) that the fluctuation component of the polarization $\delta\hat{\mathbf{P}}_L$ generated by the Langevin noise satisfies the fluctuation-dissipation theorem [97, 98]:

$$\frac{1}{2}\langle \delta\hat{\mathbf{P}}^{\dagger}_{L;\omega'}(\mathbf{r}')\delta\hat{\mathbf{P}}_{L;\omega}(\mathbf{r}) + \delta\hat{\mathbf{P}}_{L;\omega}(\mathbf{r})\delta\hat{\mathbf{P}}^{\dagger}_{L;\omega'}(\mathbf{r}')\rangle = \frac{\hbar}{\pi}\mathrm{Im}[\chi(\omega)](n_T(\omega) + \frac{1}{2})\delta(\omega - \omega')\delta(\mathbf{r} - \mathbf{r}')$$

where

$$\chi(\omega) = \frac{1}{\hbar} \sum_{m,n} \frac{|\mathbf{d}_{nm}|^2 \langle \hat{\rho}_{nn} - \hat{\rho}_{mm} \rangle}{(\omega_{mn} - \omega) - i\gamma_{mn}}$$

is the linear susceptibility of the medium, $n_T(\omega) = (e^{\hbar\omega/k_B T} - 1)^{-1}$ is the average number of thermal quanta,

$$\delta\hat{\mathbf{P}}_{L;\omega} = \sum_{m,n} \frac{\mathbf{d}_{nm} \hat{F}_{\omega;mn}}{i(\omega_{mn} - \omega) + \gamma_{mn}}$$

is the spectral component of the polarization $\delta\hat{\mathbf{P}}_L$.

3.2 Equations for the field operators

For a quasi-monochromatic electric field of a given field mode propagating in a dispersive medium with refraction index $n(\omega)$,

$$\hat{\mathbf{E}} = \hat{\mathbf{E}}_0(\mathbf{r}, t) e^{-i\omega t + ikz} + \hat{\mathbf{E}}_0^\dagger(\mathbf{r}, t) e^{-i\omega t + ikz},$$

one can introduce an operator of the slowly varying field amplitude $\hat{\mathbf{E}}_0(\mathbf{r}, t)$ which has narrow spectrum, $\Delta\omega \ll \omega$ and $\Delta k \ll k$, and is related to the operators of annihilation and creation of "photons in a medium" [99] $\hat{c}_0$ and $\hat{c}_0^\dagger$ as

$$\hat{\mathbf{E}}_0(\mathbf{r}, t) = \mathbf{e}_0 E_0 \hat{c}_0(\mathbf{r}, t), \hat{\mathbf{E}}_0^\dagger(\mathbf{r}, t) = \mathbf{e}^* E_0 \hat{c}_0^\dagger(\mathbf{r}, t),$$

where $\mathbf{e}$ is a unit vector of the polarization of the field and

$$E_0 = \sqrt{4\pi\hbar\omega^2 / \frac{\partial(\omega^2 n^2)}{\partial\omega}}.$$

With this normalization of the field operators the energy of the classical field $\mathbf{E} = \mathbf{E}_0 e^{-i\omega t+ikz} + c.c.$ in a volume V,

$$W = \frac{V}{4\pi}\left(\frac{\partial(\omega n^2)}{\partial\omega}|\mathbf{E}_0|^2 + |\mathbf{H}_0|^2\right) = \frac{V}{4\pi\omega}\frac{\partial(\omega^2 n^2)}{\partial\omega}|\mathbf{E}_0|^2,$$

is transformed into $\hat{W} = \hbar\omega(V\hat{c}_0^\dagger\hat{c}_0 + \frac{1}{2})$ after the field quantization. The commutation relation for the field operators reads $[\hat{c}_0, \hat{c}_0^\dagger] = \frac{1}{V}$. Therefore, these operators determine the number density of the photons in a certain state $|\Psi_F\rangle$ of the field as $n_{Ph} = \langle\Psi_F|\hat{c}_0^\dagger\hat{c}_0|\Psi_F\rangle$. This normalization is more convenient for field propagation problems than the conventional normalization with $[\hat{c}_0, \hat{c}_0^\dagger] = 1$ and $\hat{c}_0^\dagger\hat{c}_0$ determining the operator of the photon number [99].

The equation of motion for the field amplitude operator has the same form as the wave equation for a classical field amplitude:

$$\left(\frac{\partial}{\partial t} + \upsilon_{gr}\frac{\partial}{\partial z}\right)\hat{c}_0 = \frac{4\pi i\omega^2}{E_0\partial(\omega^2 n^2)/\partial\omega}\hat{\mathbf{P}}_0\mathbf{e}^* \tag{3.17}$$

Here $\upsilon_{gr} = \dfrac{2c^2k}{\partial(\omega^2 n^2)/\partial\omega}$ is a group velocity. Equation (14) includes all the relevant effects: the slowly varying polarization amplitude $\hat{\mathbf{P}}_0$ on the right-hand side includes nonlinearity, dissipation, and fluctuations, whereas the part of the total optical polarization $\hat{\mathbf{P}}(\mathbf{r}, t) = \mathbf{d}_{nm}\hat{\rho}_{mn}$ that describes linear dispersion was separated and gave rise to the group velocity term on the left-hand side. In a medium with a low optical density one can put $\upsilon_{gr} = c$ and $n^2 = 1$ to recover a standard field equation; see e.g. [100] . This approach based on calculating the dynamics of the Heisenberg field envelope operators is better suitable for the field propagation problems than the Schrödinger's approach of finding the evolution of a two-photon wave function. The final photon state can be reconstructed after finding the field operators.

At the boundary z_b between the medium and the vacuum, the boundary condition for the field operator takes the form

$$\hat{c}_0(z_b)|_{vacuum} = \sqrt{\frac{\upsilon_{gr}}{c}}\hat{c}_0(z_b)|_{medium} \tag{3.18}$$

which satisfies the conservation of the Poynting flux.

A more realistic field consists of many modes propagating within a paraxial beam of a cross-sectional area $S_\perp$. If we keep the same notation $\hat{c}_0$ for the field operators describing the field amplitude in the beam, their commutator becomes $[\hat{c}_0, \hat{c}_0^\dagger] = \Delta j/V$ where Δj is the number of modes. The total photon flux density in the beam is then given by

$$Q = \upsilon_{gr} S_\perp \langle \Psi_F | \hat{c}_0^\dagger \hat{c}_0 | \Psi_F \rangle.$$

It is convenient to go from a discrete set of modes to a continuous spectral interval $\Delta\omega \ll \omega$. The density of states in a volume V is equal to $\eta = Vk^2/8\pi^3\upsilon_{gr}$ and the wave vectors of the modes constituting a beam occupy the solid angle $\Delta o \approx 4\pi^2/k^2 S_\perp$. As a result, we arrive at the following commutation relations for the operator of the field amplitude and its spectral harmonics:

$$[\hat{c}_0, \hat{c}_0^\dagger] = \Delta o \Delta\omega\eta = \frac{\Delta\omega}{2\pi S_\perp \upsilon_{gr}} \tag{3.19}$$

$$\left.\begin{aligned} [\hat{c}_{0\omega'}, \hat{c}_{0\omega''}^\dagger] &= \frac{1}{2\pi S_\perp \upsilon_{gr}}\delta(\omega' - \omega'') \\ [\hat{c}_0(t'), \hat{c}_0^\dagger(t'')] &= \frac{\delta(t' - t'')}{S_\perp \upsilon_{gr}} \end{aligned}\right\} \tag{3.20}$$

Here the spectral decomposition of the field amplitude operator is defined as

$$\hat{c}_0 = \int_{\Delta\omega} \hat{c}_{0\omega} e^{-i\omega t} d\omega.$$

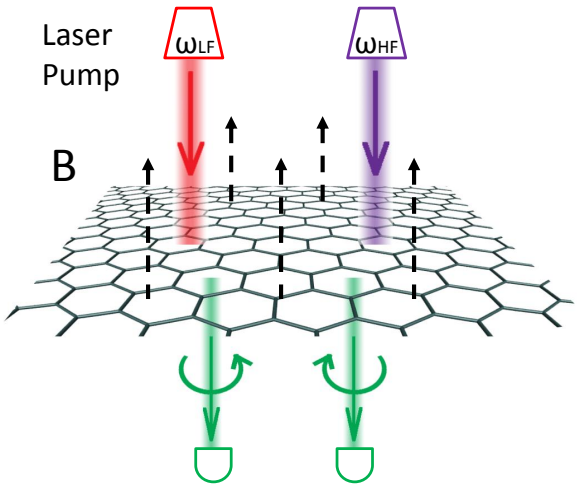

Figure 3.1: Geometry of the proposed experiment. Two pump fields at frequencies ω_{HF} and ω_{LF} normally incident on a sheet of graphene placed in a magnetic field B generate entangled photons with opposite sense of the circular polarization.

The proposed scheme is shown in Figs. 3.1 and 3.2. Here the energies of the Landau levels for electrons near the Dirac point are given by $\varepsilon_n = \mathrm{sgn}(n)\hbar\omega_c\sqrt{|n|}$, where $n = 0, \pm1, \pm2...$, $\omega_c = \sqrt{2}v_F/l_c$, $v_F \approx 10^6$ cm/s the electron Fermi velocity, and $l_c = \sqrt{\hbar c/eB}$ the magnetic length. We assume that the graphene is biased or doped so that the Fermi level is between the states with n = -2 and n = -1, i.e. the state n = -2 is occupied and the states above are empty in the absence of pumping. Two incident strong pump fields at frequencies ω_{HF} and ω_{LF} resonant to the transitions from n = -2 to n = 1 and from n = -2 to n = -1 respectively, generate two signal fields with opposite sense of the circular polarization at frequencies $\omega_{(-)}$ and $\omega_{(+)}$ that are close to resonance with transitions from n = -1 to 0 and from n =

0 to 1. The transition frequencies are easily tunable with a magnetic field.

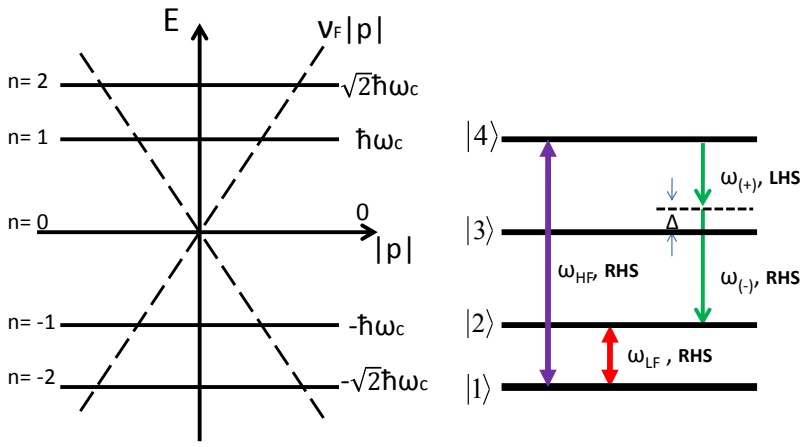

Figure 3.2: Energy levels and optical transitions involved in resonant parametric generation of entangled photons in graphene. Left: Landau levels near the Dirac point superimposed on the linear electron dispersion without the magnetic field. Right: A scheme of the entangled photon generation process in the four-level system of LLs with energy quantum numbers n = -2, -1, 0, 1 that were renamed as states 1,2,3, and 4 for convenience of notation. Right-hand side (RHS) or left-hand side (LHS) circular polarization of light indicated on the figure corresponds to the allowed transitions.

The polarizations for the allowed transitions are indicated in Fig. 3.2. Here LHS and RHS denote left-hand and right-hand circularly polarized light with polarization vectors in the (x,y) plane of the graphene defined as $\mathbf{e}_{(\mp)} = (\mathbf{x_0} \mp i\mathbf{y_0})/\sqrt{2}$, respectively. Peculiar selection rules for graphene, $\Delta|n| = \pm 1$ as opposed to $\Delta n = \pm 1$ for electrons with usual parabolic dispersion, allow transitions with a large change in the principal quantum number n, such as the transition from n = -2 to 1. The dipole matrix elements of the allowed transitions $d_{mn} \sim \hbar e \upsilon_F/(\varepsilon_n - \varepsilon_m)$ grow fast ($\sim \lambda$) with increasing wavelength, and reach a large magnitude of $\sim$ 1-10 nm in the

mid/far-infrared range; e.g. $|d|/e = 5$ nm at $\lambda = 10$ μm. This enables extremely high resonant third-order nonlinearity [67]. Note also that the states n = -1, 0, and 1 have low population when the intensities of the optical pumps are below saturation. These factors lead to a high rate of photon generation and high signal to noise ratio of entangled photons. In the four-wave mixing process depicted in Fig. 3.2, the total field consists of the four waves,

$$\begin{aligned}\hat{\mathbf{E}} &= \left(\mathbf{e}_{(+)}E_{HF}e^{-i\omega_{HF}t+ik_{HF}z} + \mathbf{e}_{(+)}E_{LF}e^{-i\omega_{LF}t+ik_{LF}z} + c.c.\right) \\ &+ \left(\mathbf{e}_{(+)}E_{(+)}e^{-i\omega_{(+)}t+ik_{(+)}z} + \mathbf{e}_{(-)}E_{(-)}e^{-i\omega_{(-)}t+ik_{(-)}z} + h.c.\right) \qquad (3.21)\end{aligned}$$

in which two classical pump fields at high and low frequencies (denoted as HF and LF) are resonant to the corresponding transitions between the Landau levels, $\omega_{HF} = \omega_{41}$ and $\omega_{LF} = \omega_{21}$, whereas two signal fields are described by the operators and their frequencies may have a small detuning, $\omega_{(+,-)} = \omega_{43,32} \mp \Delta, \Delta \ll \omega_{(+,-)}$ satisfying the frequency-matching condition $\omega_{HF} = \omega_{LF} + \omega_{(+)} + \omega_{(-)}$.

The density-matrix equations for the electrons in linear approximation with respect to weak signal fields can be derived as:

$$\begin{aligned}&\frac{\partial\hat{\eta}_{(-)}}{\partial t} + (i\Delta + \gamma_{(-)})\hat{\eta}_{(-)} - i(\hat{\Omega}_{(-)}(\hat{\eta}_{33} - \hat{\eta}_{44}) + \Omega_{HF}\hat{\eta}^{\dagger}_{31} - \hat{\eta}_{42}\hat{\Omega}^{\dagger}_{(+)}) = \hat{F}_{(-)} \equiv \hat{F}_{43} \\ &\frac{\partial\hat{\eta}_{(+)}}{\partial t} + (-i\Delta + \gamma_{(+)})\hat{\eta}_{(+)} - i(\hat{\Omega}_{(-)}(\hat{\eta}_{22} - \hat{\eta}_{33}) + \hat{\Omega}^{\dagger}_{(-)}\hat{\eta}_{42} - \hat{\eta}_{31}\Omega^{*}_{LF}) = \hat{F}_{(+)} \equiv \hat{F}_{32} \\ &\frac{\partial\hat{\eta}_{42}}{\partial t} + \gamma_{42}\hat{\eta}_{42} - i(\Omega_{HF}\hat{\eta}^{\dagger}_{21} - \hat{\eta}_{41}\Omega^{*}_{LF}) = \hat{F}_{42} \\ &\frac{\partial\hat{\eta}_{31}}{\partial t} + (-i\Delta + \gamma_{31})\hat{\eta}_{31} - i(\hat{\Omega}^{\dagger}_{(-)}\hat{\eta}_{41} + \hat{\Omega}_{(+)}\hat{\eta}_{21} - \hat{\eta}_{(+)}\Omega_{LF} - \hat{\eta}^{\dagger}_{(-)}\Omega_{HF}) = \hat{F}_{31} \\ &\frac{\partial\hat{\eta}_{41}}{\partial t} + \gamma_{41}\hat{\eta}_{41} - i\Omega_{HF}(\hat{\eta}_{11} - \hat{\eta}_{44}) = \hat{F}_{41} \\ &\frac{\partial\hat{\eta}_{21}}{\partial t} + \gamma_{21}\hat{\eta}_{21} - i\Omega_{LF}(\hat{\eta}_{11} - \hat{\eta}_{22}) = \hat{F}_{21}. \qquad (3.22)\end{aligned}$$

Here

$$\hat{\rho}_{41,21,42} = \hat{\eta}_{41,21,42} e^{-i\omega_{41,21,42}t}, \hat{\rho}_{32,43} = \hat{\eta}_{(+,-)} e^{-i(\omega_{32,43} \mp \Delta)t}, \hat{\rho}_{31} = \hat{\eta}_{31} e^{-i(\omega_{31}-\Delta)t},$$
$$\Omega_{HF} = \frac{d_{14}^* E_{HF}}{\hbar}, \Omega_{LF} = \frac{d_{12}^* E_{LF}}{\hbar}, \hat{\Omega}_{(+,-)} = \frac{d_{(+,-)}^* \hat{E}_{(+,-)}}{\hbar}.$$

The optimal conditions for the entanglement are realized when the Fermi level is close to the state 1 (n = -2) and the populations for all higher-lying states $m > 1$ are low. This is possible when the thermal excitations are low, $k_B T \ll \hbar\omega_c$ and the Rabi frequencies of the pump fields are below saturation: $|\Omega_{HF,LF}| \ll \langle\gamma\rangle$. Here we assume for simplicity that all scattering rates γ_{mn} are of the same value $\langle\gamma\rangle$. The latter assumption can be easily dropped once the relaxation rates are known for any particular sample. If, in addition, the detuning is sufficiently large, $\langle\gamma\rangle \ll \Delta$, the populations of the excited states with $m > 1$ are mostly due to the Langevin noise terms $\hat{F}_{(+,-)}$ in Eqs. (3.22) and Raman scattering of the pump into the signal photons can be neglected. Solving the density-matrix equations in the steady state and neglecting the terms of the order of $(\langle\gamma\rangle/\Delta)^2$, we arrive at the following expression for the operator of the polarization amplitude at the frequency of the signal fields:

$$\hat{\mathbf{P}}_{(+,-)} = \mathbf{e}_{(+,-)} d_{(+,-)} \hat{\eta}_{(+,-)} \approx \mathbf{e}_{(+,-)} \left(\chi \hat{E}_{(-,+)}^{\dagger} \mp i \frac{d_{(+,-)} \hat{F}_{(+.-)}}{\Delta} \right) \tag{3.23}$$

where

$$\chi = \frac{N d_{(+)} d_{(-)}}{\hbar\Delta} \frac{(\gamma_{21} + \gamma_{41})\Omega_{HF}\Omega_{LF}^*}{\gamma_{21}\gamma_{41}\gamma_{42}} \sim \frac{N d^2}{\hbar\Delta} \frac{\Omega_p^2}{\langle\gamma\rangle^2} \tag{3.24}$$

and we denoted $\Omega_p^2 = \Omega_{HF}\Omega_{LF}^*$ and $d = \hbar e \upsilon_F/\omega_{32}$. Using the polarization (Eq. 3.23) as a source in Eqs. (3.17), we obtain the following coupled equations for the signal

field operators:

$$\left.\begin{aligned}\left(\frac{\partial}{\partial z}+\frac{1}{v_{gr}}\frac{\partial}{\partial t}\right)\hat{c}_{(+)}&=i\kappa\hat{c}^{\dagger}_{(-)}+\hat{G}_{(+)}\\ \left(\frac{\partial}{\partial z}+\frac{1}{v_{gr}}\frac{\partial}{\partial t}\right)\hat{c}^{\dagger}_{(-)}&=-i\kappa^{*}\hat{c}_{(+)}+\hat{G}^{\dagger}_{(-)}\end{aligned}\right\}, \tag{3.25}$$

where the coefficient of the parametric coupling is $\kappa=2\pi\chi\dfrac{\langle\omega\rangle^2}{c^2\langle k\rangle}$ and the noise term

$$\hat{G}_{(+,-)}=\mp 2\pi i\frac{\langle\omega\rangle^2}{c^2\langle k\rangle}\frac{d_{(+,-)}\hat{F}_{(+,-)}}{E_0\Delta};$$

we neglected the small difference between the central frequencies of the signal fields in the pre-factors, assuming $\omega_{(+)}=\omega_{(-)}=\langle\omega\rangle$ and $\langle k\rangle=\langle\omega\rangle/c$.

The noise terms are described by the correlation functions

$$\left.\begin{aligned}\langle\hat{G}^{\dagger}_{\omega'(+,-)}(z')\hat{G}_{\omega(+,-)}(z)\rangle&=\Gamma_{(+,-)}\frac{\gamma_{(+,-)}}{\Delta}\frac{1}{2\pi S_{\perp}v_{gr}}\delta(\omega'-\omega)\delta(z-z')\\ \langle\hat{G}_{\omega(+,-)}(z)\hat{G}^{\dagger}_{\omega'(+,-)}(z')\rangle&=\tilde{\Gamma}_{(+,-)}\frac{\gamma_{(+,-)}}{\Delta}\frac{1}{2\pi S_{\perp}v_{gr}}\delta(\omega'-\omega)\delta(z-z')\end{aligned}\right\} \tag{3.26}$$

where the factors

$$\Gamma_{(+,-)}=2\pi\frac{\langle\omega\rangle^2}{c^2\langle k\rangle}\frac{N_{4,3}|d_{(+,-)}|^2}{\hbar\Delta},\tilde{\Gamma}_{(+,-)}=2\pi\frac{\langle\omega\rangle^2}{c^2\langle k\rangle}\frac{N_{3,2}|d_{(+,-)}|^2}{\hbar\Delta} \tag{3.27}$$

are of the order of the parametric coupling terms:

$$\Gamma_{(+,-)}\sim\tilde{\Gamma}_{(+,-)}\sim\frac{\langle\omega\rangle^2}{c^2\langle k\rangle}\frac{Nd^2}{\hbar\Delta}\frac{\Omega_R^2}{\langle\gamma\rangle^2}\sim|\kappa|. \tag{3.28}$$

Going from Eq. (3.16) to Eq. (3.26), we made the substitution $\delta(\mathbf{r}-\mathbf{r}')\rightarrow\delta(z-z')S_{\perp}^{-1}$ corresponding to a beam of rays with a fixed transverse cross-section.

Equations (3.25) are convenient to solve in terms of the spectral components of

the field amplitude operators:

$$\left.\begin{aligned}\left(\frac{\partial}{\partial z}-i\frac{\omega}{v_{gr}}\right)\hat{c}_{\omega(+)}&=i\kappa\hat{c}^{\dagger}_{\omega(-)}+\hat{G}_{\omega(+)}\\ \left(\frac{\partial}{\partial z}-i\frac{\omega}{v_{gr}}\right)\hat{c}^{\dagger}_{\omega(-)}&=-i\kappa^{*}\hat{c}_{\omega(+)}+\hat{G}^{\dagger}_{\omega(-)}\end{aligned}\right\}. \tag{3.29}$$

Here ω is a small detuning from the central frequency $\omega_{(+)}$ or $\omega_{(-)}$. The solution to Eq. (3.29) can be immediately obtained in the form

$$\begin{aligned}\begin{pmatrix}\hat{c}_{\omega(+)}\\ \hat{c}^{\dagger}_{\omega(-)}\end{pmatrix} &= \begin{pmatrix}1\\ K_x\end{pmatrix}\left(\hat{u}_{\omega,X}e^{iq_X(\omega)z}+\int_0^z e^{-iq_X(\omega)(\xi-z)}\hat{f}_{\omega,X}d\xi\right)\\ &+ \begin{pmatrix}1\\ K_O\end{pmatrix}\left(\hat{u}_{\omega,O}e^{iq_O(\omega)z}+\int_0^z e^{-iq_O(\omega)(\xi-z)}\hat{f}_{\omega,O}d\xi\right)\end{aligned} \tag{3.30}$$

where

$$q_{O,X}=\frac{\omega}{v_{gr}}\pm i|\kappa|, K_{O,X}=\pm ie^{-i\Theta}, \kappa=|\kappa|e^{i\Theta}. \tag{3.31}$$

The expression (3.30) is a sum of two modes denoted by O and X, one of which is unstable. The operators $\hat{u}_{\omega,X}$ and $\hat{u}_{\omega,O}$ are expressed through the operators of the incident field at the boundary of the graphene layer $z=0$. Taking into account the boundary condition (3.18), we obtain

$$\left.\begin{aligned}\hat{u}_{\omega,X}&=\sqrt{\frac{c}{v_{gr}}}\left(\frac{\hat{c}_{\omega(+)}(0)}{2}-\frac{\hat{c}^{\dagger}_{\omega(-)}(0)}{2i}e^{i\Theta}\right)\\ \hat{u}_{\omega,O}&=\sqrt{\frac{c}{v_{gr}}}\left(\frac{\hat{c}_{\omega(+)}(0)}{2}+\frac{\hat{c}^{\dagger}_{\omega(-)}(0)}{2i}e^{i\Theta}\right)\end{aligned}\right\}, \tag{3.32}$$

The Langevin noise source terms for the O and X modes are given by

$$\hat{f}_{\omega,X}=\frac{\hat{G}_{\omega(+)}}{2}-\frac{\hat{G}^{\dagger}_{\omega(-)}}{2i}e^{i\Theta}, \hat{f}_{\omega,O}=\frac{\hat{G}_{\omega(+)}}{2}+\frac{\hat{G}^{\dagger}_{\omega(-)}}{2i}e^{i\Theta} \tag{3.33}$$

The solution for the fields after propagating through a layer of thickness L becomes

$$\begin{aligned}
\hat{c}_{\omega(+)}(L) &= e^{i\omega\frac{z}{\upsilon_{gr}}}(\cosh(|\kappa|L)\hat{c}_{\omega(+)}(0) - ie^{i\Theta}\sinh(|\kappa|L)\hat{c}^{\dagger}_{\omega(-)}(0)) \\
&+ \sqrt{\frac{\upsilon_{gr}}{c}}\int_0^L e^{i\frac{\omega(z-\xi)}{\upsilon_{gr}}}(\cosh(|\kappa|(L-\xi))\hat{G}_{\omega(+)}(\xi) \\
&- ie^{i\Theta}\sinh(\kappa(L-\xi))\hat{G}^{\dagger}_{\omega(-)}(\xi))d\xi, \\
\hat{c}_{\omega(-)}(L) &= e^{-i\omega\frac{z}{\upsilon_{gr}}}(\cosh(|\kappa|L)\hat{c}_{\omega(-)}(0) - ie^{i\Theta}\sinh(|\kappa|L)\hat{c}^{\dagger}_{\omega(+)}(0)) \\
&+ \sqrt{\frac{\upsilon_{gr}}{c}}\int_0^L e^{-i\frac{\omega(z-\xi)}{\upsilon_{gr}}}(\cosh(|\kappa|(L-\xi))\hat{G}_{\omega(-)}(\xi) \\
&- ie^{2i\Theta}\sinh(\kappa(L-\xi))\hat{G}^{\dagger}_{\omega(+)}(\xi))d\xi,
\end{aligned} \tag{3.34}$$

In the optimal limit of $|\Omega_p| \ll \langle\gamma\rangle \ll \Delta$, the terms containing the noise operator $\hat{G}$ can be neglected and the solution for the fields exiting a layer of thickness L takes a particularly simple form after taking an inverse Fourier transformation:

$$\left.\begin{aligned}
\hat{c}_{(+)}(L,t) &= \cosh(\tau)\hat{c}_{(+)}\left(0, t-\frac{L}{\upsilon_{gr}}\right) - ie^{i\theta}\sinh(\tau)\hat{c}^{\dagger}_{(-)}\left(0, t-\frac{L}{\upsilon_{gr}}\right) \\
\hat{c}_{(-)}(L,t) &= \cosh(\tau)\hat{c}_{(-)}\left(0, t-\frac{L}{\upsilon_{gr}}\right) - ie^{i\theta}\sinh(\tau)\hat{c}^{\dagger}_{(+)}\left(0, t-\frac{L}{\upsilon_{gr}}\right)
\end{aligned}\right\}. \tag{3.35}$$

where $\tau = |\kappa|L$.

Equations (3.34) and (3.35) clearly show the emergence of quantum correlations between the signal photons. In particular, consider the boundary condition at $z = 0$ corresponding to a completely uncorrelated state of vacuum fluctuations within the spectral bandwidth $\Delta\omega$. It is convenient to define it through the relation

$$\hat{c}^{\dagger}_{0\omega''}\hat{c}_{0\omega'} = \hat{c}^{\dagger}_{S}\hat{c}_{S}[\hat{c}_{0\omega'}, \hat{c}^{\dagger}_{0\omega''}] \tag{3.36}$$

where $\hat{c}_S, \hat{c}_S^\dagger$ are Schroedinger operators acting on the initial state $|0\rangle$ and normalized according to $[\hat{c}_S, \hat{c}_S^\dagger] = 1$. Using Eq. (3.36) together with Eq. (3.20) one can obtain from Eq. (3.35) that the photon fluxes in two signal fields exiting the layer at $z = L$ are completely correlated:

$$\left.\begin{array}{c} \langle 0|\hat{Q}_{(+)}(L)|0\rangle = \langle|\hat{Q}_{(-)}(L)|0\rangle = \dfrac{\Delta\omega}{2\pi}\sinh^2\tau \\ \langle 0|(\hat{Q}_{(+)}(L) - \hat{Q}_{(-)}(L))^2|0\rangle = 0 \end{array}\right\} \tag{3.37}$$

Here $\hat{Q}_{(+,-)}(L) = cS_\perp \hat{c}^\dagger_{(+,-)}(L)\hat{c}_{(+,-)}(L)$ are operators of the photon fluxes. The second equation in (3.37) corresponds to the Manley-Rowe relations for the parametric process. It also follows from Eq. (3.35) that the system could be used to amplify the light with nonclassical statistics of exchange the statistical properties between (+) and (−) photons.

If noise is taken into account, the result in Eq. (3.37) gets modified to

$$\begin{aligned} &\langle 0|\hat{Q}_{(+)}(L)|0\rangle \approx \frac{\Delta\omega}{2\pi} \times \\ &\left(\sinh^2\tau + \frac{\frac{\gamma_{(+)}}{\Delta}\Gamma_{(+)}(\sinh 2\tau + 2\tau) + \frac{\gamma_{(-)}}{\Delta}\tilde{\Gamma}_{(-)}(\sinh 2\tau - 2\tau)}{4|\kappa|}\right), \\ &\langle 0|\hat{Q}_{(-)}(L)|0\rangle \approx \frac{\Delta\omega}{2\pi} \times \\ &\left(\sinh^2\tau + \frac{\frac{\gamma_{(-)}}{\Delta}\Gamma_{(-)}(\sinh 2\tau + 2\tau) + \frac{\gamma_{(+)}}{\Delta}\tilde{\Gamma}_{(+)}(\sinh 2\tau - 2\tau)}{4|\kappa|}\right). \end{aligned} \tag{3.38}$$

From these formulas one can see that the noise contribution can be neglected if $\Delta \gg \langle\gamma\rangle$ provided the parametric gain is high enough: $\tau \geq 1$. For a weak amplification $\tau \ll 1$ the condition for a large signal to noise ratio is more stringent: $\Delta \gg \langle\gamma\rangle/\tau$. The behavior of the parametric gain τ per monolayer as a function of the detuning and the pump field intensity is illustrated in Figs. 3.3 and 3.4. If this condition is not satisfied or if one of the states 2, 3, or 4 acquires a large

population, then in the steady state the noise is always comparable to or greater than the signal. In this case, the entangled photons can be generated only in the pulsed regime during the time of the order of a few relaxation times $1/\gamma$. This is usually the case in resonant schemes of entanglement in atomic vapors[101][102].

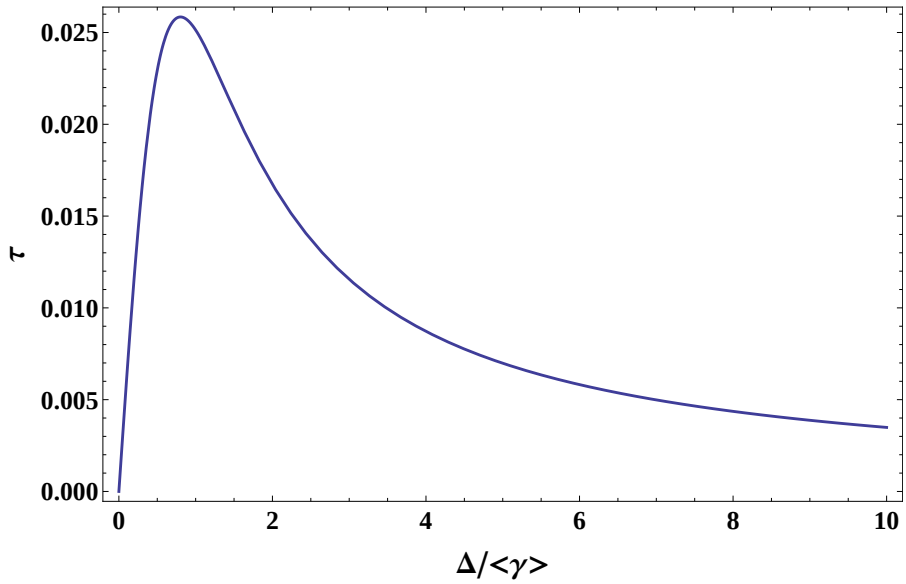

Figure 3.3: Parametric gain τ per monolayer of graphene as a function of normalized detuning of the signal fields $\Delta/\langle\gamma\rangle$ for the pump field intensity $|\Omega_p| = 0.1\langle\gamma\rangle$.

The above analytic results were derived in the limit of $|\Omega_p| \ll \langle\gamma\rangle \ll \Delta$. In the general case the equations can be solved numerically, including the effects of the optical pumping of electrons to excited states and optical saturation. The resulting parametric gain τ per one monolayer of graphene is plotted in Figs. 3.3 and 3.4 as a function of the frequency detuning and the pump intensity. As seen from the figures, the magnitude of τ is around 0.01 for $\Delta \sim 10\gamma \sim 100\Omega_p$. To increase the value of τ for a higher rate of the twin photon generation, one can use a stack of graphene monolayers or a thin layer of graphite. Recent studies have demonstrated that a

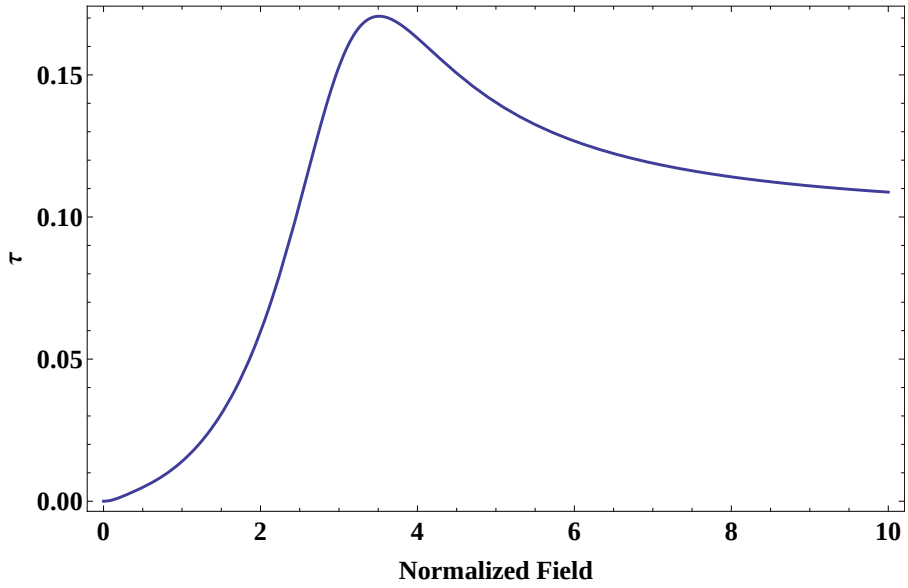

Figure 3.4: Parametric gain τ per monolayer of graphene as a function of normalized strength of the pump field $|\Omega_p|/\langle\gamma\rangle$ for the detuning $\Delta = 10\langle\gamma\rangle$.

graphite layer consisting of $\sim$ 100 monolayers maintains high carrier mobility and graphene-like Landau levels near the H-point of the 3D Brillouin zone of graphite [70, 71]. The optimal thickness is a tradeoff between the pump absorption and the desired output photon flux.

In conclusion, we show that graphene placed in a magnetic field can serve as an efficient, tunable source of polarization-entangled photons in the mid/far-infrared frequency range. The proposed scheme can operate at high temperatures if the magnetic field is high enough to prevent thermal excitations, $k_B T \ll \hbar\omega_c$. A thin layer of graphene can be easily integrated with semiconductor laser chips and optoelectronic circuits to make a compact setup. A similar mechanism of entangled photon generation could exist in other materials which show a massless dispersion, for example topological insulators. We hope that our results will stimulate active experimental research in this area at the intersection of quantum optics, materials science and

information technology.

4. DIFFERENCE FREQUENCY GENERATION OF TERAHERTZ SURFACE PLASMONS*

Graphene exhibits many interesting electronic properties because of its chiral symmetry and gapless linear spectrum of free carriers near the Dirac point. In recent years, graphene has also been recognized as a promising broadband optoelectronic material in the infrared (IR) and terahertz (THz) region, especially when utilizing a surface plasmon resonance [51, 52, 63]. A surface plasmon is a collective mode of coupled charge-density and field oscillations at an interface between a free-carrier system and a dielectric or vacuum. Surface plasmons guided by graphene are expected to have low losses and be highly tunable by gating and doping, making graphene an attractive alternative to metal plasmonics. Surface states in certain topological insulators (TIs) have a massless Dirac-cone electron dispersion at low energies with a slope similar to that in graphene. They provide a potentially even more interesting host medium for surface plasmons due to lower scattering rates of two-dimensional (2D) surface electrons that are topologically protected from scattering on non-magnetic impurities [31]. In particular, Bi_2Se_3 has a large bulk band gap of about 0.3 eV, suitable for THz and mid-infrared plasmonics, and a tunable Fermi level which can be put within the bulk gap [64]. The combination of highly efficient light-matter interaction, relatively long propagation distances, and tight confinement of surface plasmons in graphene and TIs promises interesting applications including compact room-temperature THz sources for imaging, spectroscopy and telecommunications; integrated photonic circuits; THz modulation of telecom

*Reprinted with permission from Efficient Nonlinear Generation of THz Plasmons in Graphene and Topological Insulator by Xianghan Yao, Mikhail Tokman, and Alexey Belyanin, 2014. Phys. Rev. Lett., vol. 112, pp. 055501, Copyright [2014] by the American Physical Society.

signals, and compact THz sensors. Furthermore, optical methods [44] may provide a better access to characterization and manipulation of massless fermion states than transport measurements that are affected by conductivity in the bulk.

4.1 Surface plasmon resonance in 2D Dirac fermion systems

In the absence of an external magnetic field, the linear electric susceptibility of monolayer graphene can be calculated using Keldysh's Green function(Eq. 1.20). One can obtain the same result using the 1st-order solution of density matrix element. Recall that in the absence of magnetic field, the effective Hamiltonian of monolayer graphene near Dirac point is given by

$$\hat{H}_k = \hbar \upsilon_F \begin{pmatrix} 0 & k_x + ik_y \\ k_x - ik_y & 0 \end{pmatrix} = \hbar \upsilon_F \hat{\vec{\sigma}} \cdot \vec{k}; \tag{4.1}$$

with eigenfunction and eigenvalue:

$$\begin{aligned} \psi_{s,\vec{k}}(\vec{r}) &= \frac{1}{\sqrt{2L}} \exp(i\vec{k} \cdot \vec{r}) \begin{pmatrix} s \\ e^{i\theta(\vec{k})} \end{pmatrix}; \\ \varepsilon_{s,\vec{k}} &= s \cdot \hbar \upsilon_F |\vec{k}|, \end{aligned} \tag{4.2}$$

where L^2 is the area of graphene, $\theta(\vec{k})$ is the angle of wave vector $\vec{k}$ in momentum-plane, and s denotes the band($s = +1$ for conduction band, $s = -1$ for valance band). For a given electric field $\vec{E} = \hat{e}E(\omega)e^{iqx - i\omega t}$, the interaction Hamiltonian is simply

$$\hat{H}_{int} = \frac{ie\upsilon_F}{\omega} \hat{\vec{\sigma}} \cdot \vec{E},$$

which is determined by the field and Pauli matrix vector $\vec{\sigma}$ only. Following the derivation of Eq. (2.13), one can write down the transition matrix element for monolayer

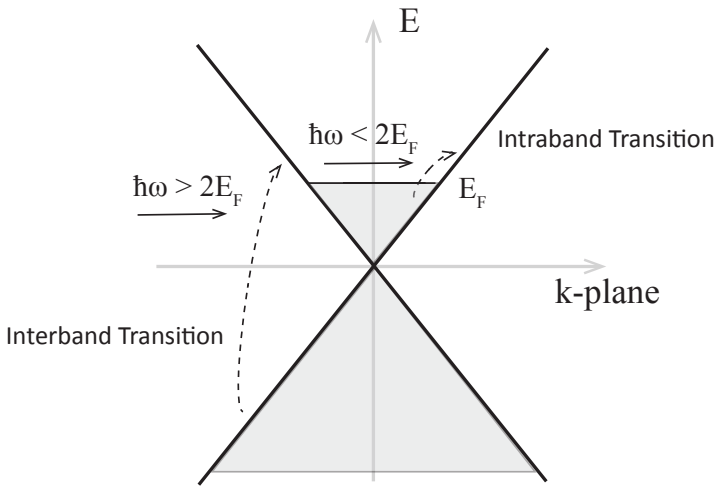

Figure 4.1: Interband transition and intraband transition in doped monolayer graphene.

graphene

$$\langle s,\vec{k}|\hat{H}_{int}|s',\vec{k}'\rangle = \frac{ie}{\omega}\vec{v}_{s\vec{k},s'\vec{k}'}\cdot\vec{E} \equiv \tilde{\vec{\mu}}\cdot\vec{E}, \tag{4.3}$$

where the velocity operator is defined as $\vec{v}_{s\vec{k},s'\vec{k}'} = \langle s,\vec{k}|\upsilon_F\vec{\sigma}|s',\vec{k}'\rangle$. Typically, the in-plane wave vector of a optical field is much smaller than electron wave vector, so that $\vec{k} \approx \vec{k}'$. We can further simplify the velocity operator for inter- and intraband transition (as shown in Fig. 4.1) as:

$$\begin{cases} \vec{v}_{inter} = is\upsilon_F(\sin\theta\hat{x} + \cos\theta\hat{y}); \\ \vec{v}_{intra} = s\upsilon_F(\cos\theta\hat{x} - \sin\theta\hat{y}). \end{cases} \tag{4.4}$$

Similarly, the dipole matrix element is also determined by Pauli matrix only:

$$\vec{\mu}_{sk,s'k'} = e \cdot \langle s, \vec{k}|\vec{r}|s', \vec{k}'\rangle = \frac{i\hbar e}{\varepsilon_{s',k'} - \varepsilon_{s,k}} \langle s, \vec{k}|\upsilon_F \hat{\vec{\sigma}}|s', \vec{k}'\rangle. \tag{4.5}$$

In the limit that the Fermi energy is greater than the plasmon energy ($E_F > \hbar\omega/2$), interband transitions are much less efficient than intraband transitions. We can simplify the calculation by only counting surface polarization resulting from intraband transitions. Combine with the 1st-order solution of density matrix element, we conclude the expression of 2D linear electric susceptibility of graphene

$$\chi_{ij}^{(1)}(\omega) = \sum_{k_1,k_2} \frac{f(k_1) - f(k_2)}{\hbar} \frac{\tilde{\vec{\mu}}_{k_2,k_1}^{j} \vec{\mu}_{k_1,k_2}^{i}}{(\omega_{k_1,k_2} - \omega) - i\gamma}. \tag{4.6}$$

Here $\chi_{xx} = \chi_{yy} = \tilde{\chi}_{\omega,q}$ and $\chi_{xy} = \chi_{yx} = 0$. In the limit of $\omega \gg \upsilon_F q$,

$$\begin{aligned} \tilde{\chi}_{\omega,q} &= \frac{g}{(2\pi)^2} \frac{e^2 \upsilon_F}{\hbar\omega} \int_0^\infty dk \int_0^{2\pi} d\phi \frac{\partial f(k)}{\partial k} k_x \frac{\cos\phi}{-i\gamma + \upsilon_F q \cos\phi - \omega} \\ &= -\frac{g}{(2\pi)^2} \frac{e^2 \upsilon_F}{\hbar\omega} \int_0^\infty f(k) dk \int_0^{2\pi} d\phi \frac{\cos^2\phi}{-i\gamma + \upsilon_F q \cos\phi - \omega}. \end{aligned} \tag{4.7}$$

ω and q are frequency and x-component of the wave vector in a monochromatic wave, ϕ is the angle between the electron momentum and x-axis; γ is the scattering rate which greatly depends on the material and substrate quality. The degeneracy factor g is equal to 4 for graphene. $f(k)$ is the Fermi-Dirac distribution function $1/(e^{(\epsilon - E_F)/kT} + 1)$. The integral in Eq. (4.7) is equal to:

$$\frac{kT}{\hbar\upsilon_F} \ln\left(1 + e^{\frac{2E_F}{kT}}\right) \frac{2\pi(\omega + i\gamma)}{\upsilon_F^2 q^2} \left(1 + \frac{\omega - i\gamma}{\omega + \upsilon_F q + i\gamma} \sqrt{1 + \frac{2\upsilon_F q}{\omega - \upsilon_F q + i\gamma}}\right).$$

At low temperature, $\frac{kT}{\hbar v_F}\ln\left(1+e^{\frac{2E_F}{kT}}\right) \approx \frac{2E_F}{\hbar v_F}$. Placed on an interface between two dielectric media with dielectric constants ϵ_1 and ϵ_2, as shown in the inset to Fig. 1.4, the monolayer graphene supports TM-mode with non-zero E_x, E_z, and B_y field components. Recall field components are solutions of the Helmholtz equation Eq. (1.23) with the relationships given by Eq. (1.24), the TM-mode field has the form:

$$E_x = \mathcal{E}_{\pm}e^{\mp p_{1,2}z}, E_z = \pm i\frac{q}{p_{1,2}}\mathcal{E}_{\pm}e^{\mp p_{1,2}z}, B_y = \mp i\frac{\epsilon_{1,2}\omega}{cp_{1,2}}\mathcal{E}_{\pm}e^{\mp p_{1,2}z}. \tag{4.8}$$

Here $\pm$ denotes the field components in the bulk regions $z > 0$ and $z < 0$, respectively; $p_{1,2} = \sqrt{q^2 - \epsilon_{1,2}\frac{\omega^2}{c^2}}$ determines the inverse confinement length in z-direction. Given the surface current J with frequency ω and in-plane momentum q in x-direction on the monolayer graphene sheet, the fields on both sides satisfy the boundary conditions

$$\begin{aligned}
&\epsilon_1 E_z(+0) - \epsilon_2 E_z(-0) = \frac{4\pi q}{\omega}\left(J - i\omega\tilde{\chi}_{\omega,q}E_x(0)\right), \\
&E_x(+0) - E_x(-0) = 0.
\end{aligned}$$

From here we derive the field amplitude:

$$\mathcal{E}_+ = \mathcal{E}_- = \mathcal{E} = -i\frac{4\pi J}{\omega\left(4\pi\tilde{\chi}_{\omega,q} + \frac{\epsilon_1}{p_1} + \frac{\epsilon_2}{p_2}\right)}. \tag{4.9}$$

Note that the expression in the denominator is the dispersion equation for surface plasmon modes guided by monolayer graphene:

$$D(\omega, q) = 4\pi\tilde{\chi}_{\omega,q} + \frac{\epsilon_1}{p_1} + \frac{\epsilon_2}{p_2} = 0. \tag{4.10}$$

As a result, when ω and q satisfy the plasmon dispersion relation, i.e. $\mathrm{Re}[D(\omega,q)] = 0$, the generated field is greatly enhanced to

$$\mathcal{E} = -\frac{J}{\omega \mathrm{Im}\tilde{\chi}_{\omega,q}} \approx -\frac{4\pi q J}{\gamma(\epsilon_1+\epsilon_2)}. \tag{4.11}$$

Here we used the fact that $D(\omega,q) = 4\pi \mathrm{Im}\tilde{\chi}_{\omega,q} \approx \frac{\gamma}{\omega}\frac{\epsilon_1+\epsilon_2}{q}$ when $\mathrm{Re}D(\omega,q) = 0$.

The double layer geometry of the kind shown in the inset to Fig. 1.5 supports two types of surface plasmon modes[62]: symmetric ω_+ and antisymmetric ω_- (only the field of the symmetric mode is shown in the inset). The symmetric TM mode is robust to many-body effects, which is given by:

$$\begin{aligned}
|z| \le \frac{d}{2} \quad &: \quad E_x = \mathcal{E}_0 \cosh p_2 z; E_z = -i\frac{q}{p_2}\mathcal{E}_0 \sinh p_2 z; B_y = +i\frac{\epsilon_2\omega}{p_2 c}\mathcal{E}_0 \sinh p_2 z. \\
|z| > \frac{d}{2} \quad &: \quad E_x = \mathcal{E}_\pm e^{\mp p_1(z\pm\frac{d}{2})}, E_z = \pm i\frac{q}{p_1}\mathcal{E}_\pm e^{\mp p_1(z\pm\frac{d}{2})}, B_y = \mp i\frac{\epsilon_1\omega}{cp_1}\mathcal{E}_\pm e^{\mp p_1(z\pm\frac{d}{2})}.
\end{aligned} \tag{4.12}$$

Here $\pm$ denotes the field components in the bulk regions $z > \frac{d}{2}$ and $z < -\frac{d}{2}$; 0 denotes the field inside the two surface layers $|z| \le \frac{d}{2}$. Given two identical surface currents on both surfaces, i.e. $Je^{iqx-i\omega t}\delta(z\pm\frac{d}{2})$, we solve the amplitude of the excited symmetric field using a similar method:

$$\begin{aligned}
&\mathcal{E}_+ = \mathcal{E}_- = \mathcal{E}_0 \cosh\left(p_2\frac{d}{2}\right), \\
&\mathcal{E}_0 \cosh\left(p_2\frac{d}{2}\right) = -i\frac{4\pi J}{\omega\left(\frac{\epsilon_1}{p_1} + \frac{\epsilon_2}{p_2}\tanh p_2\frac{d}{2} + 4\pi\tilde{\chi}_{\omega,q}\right)},
\end{aligned} \tag{4.13}$$

where the dispersion equation of the symmetric plasmon mode appears in the denominator. Again, when ω and q satisfy the plasmon dispersion relation, the generated field resonates with the plasmon mode and gets greatly enhanced.

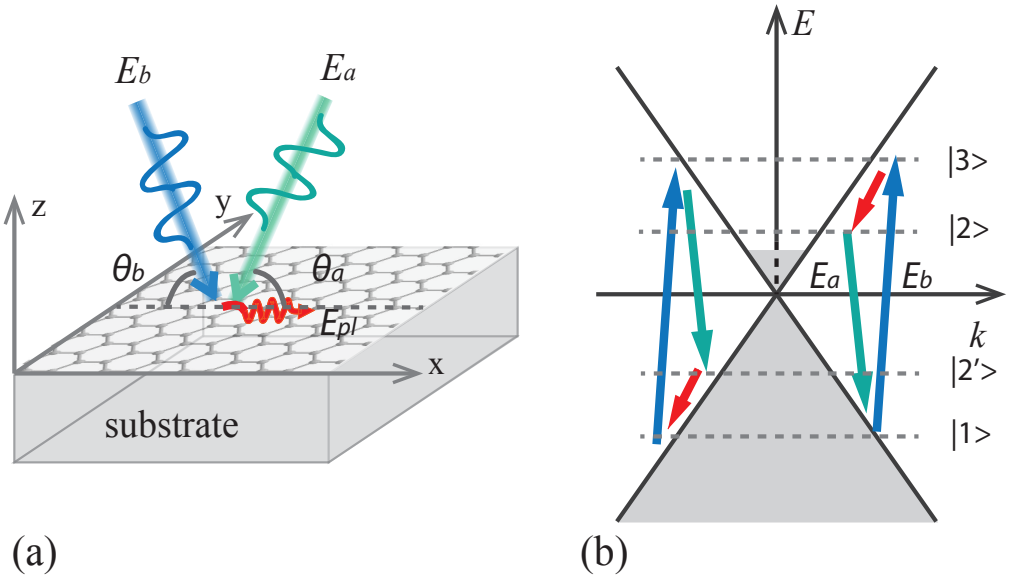

Figure 4.2: (a): Geometry of the DFG process. Two pump fields at frequencies ω_a and ω_b incident at angles θ_a and θ_b on graphene/TI placed on a substrate generate a highly confined surface plasmon field E_{pl} at their difference frequency and in-plane wave vector $q = q_b - q_a$. (b): Elementary three-wave-mixing processes involving two photons and a plasmon coupled to interband and intraband transitions, respectively. Grey shading indicates filled electron states.

Nonlinear optics of massless Dirac fermions has received little attention so far, especially in the THz range where many basic devices and components are lacking. Here we show that the difference frequency generation (DFG) in 2D layers of massless Dirac electrons is an efficient and controllable way of generating surface plasmons over a broad range of frequencies[103]. Second-order nonlinear processes

such as DFG are usually assumed to be forbidden in an isotropic medium such as the plane of a graphene layer. However, the second-order susceptibility $\chi^{(2)}$ becomes non-zero when its spatial dispersion (dependence on photon wave vectors) is taken into account. In our case the anisotropy is induced by the in-plane wave vectors of obliquely incident electromagnetic waves. The proposed experiment scheme is shown in Fig. 4.2(a). This effect is well-known for the DFG of plasma waves in a bulk isotropic classical plasma. Another second-order nonlinear process, second-harmonic generation in graphene has been theoretically studied in [104, 105]. Of course second-order processes are also non-zero for out-of-plane excitations due to anisotropy between in-plane and out-of-plane directions, which is a property of any surface. Here we consider only in-plane excitations which yield a much stronger non-linear effect. We find that the DFG of surface plasmons at the beat frequency of two obliquely incident or in-plane propagating infrared beams shows a surprisingly high efficiency over a broad range of frequencies and is widely tunable by varying an angle of incidence, gating, or doping.

We here study the nonlinear optical excitation of THz surface plasmons, based on difference frequency generation, in graphene material. First, consider two incident mid-infrared pump fields at frequencies ω_a and ω_b linearly polarized in the xz plane in the geometry shown in Fig. 4.2(a).

$$\tilde{E} = E_a e^{iq_a x - i\omega_a t} + E_b e^{iq_b x - i\omega_b t} + c.c.$$

For high pump frequencies a purely intraband contribution to the second-order susceptibility is very small, and the three-wave mixing processes that give the main contribution to the DFG signal at frequency $\omega = \omega_b - \omega_a$ are those in which the pump fields are coupled to the interband transitions and the difference-frequency

field is coupled to the intraband transitions. For a particular triplet of electron k-states $|1\rangle, |2\rangle, |3\rangle$ shown in Fig. 4.2(b), i.e. when the intraband transition is in the conduction band, one can obtain the following set of density matrix equations from density-matrix-formalism:

$$\begin{aligned}
\frac{\partial \sigma_{21}}{\partial t} + \Gamma_{21}\sigma_{21} &= ie_1(\rho_{11} - \rho_{22}) + ie_2^*\sigma_{31} - ie_3\sigma_{32}^*; \\
\frac{\partial \sigma_{31}}{\partial t} + \Gamma_{31}\sigma_{31} &= ie_3(\rho_{11} - \rho_{33}) - ie_1\sigma_{32} + ie_2\sigma_{21}; \\
\frac{\partial \sigma_{32}}{\partial t} + \Gamma_{32}\sigma_{32} &= ie_2(\rho_{22} - \rho_{33}) - ie_1^*\sigma_{31} + ie_3\sigma_{21}^*.
\end{aligned} \tag{4.14}$$

Here we used the rotating wave approximation assuming

$$\begin{aligned}
&\rho_{21,31,32} = \sigma_{21,31,32}e^{-i\omega_{21,31,32}t}, \\
&e_{1,2,3} = \frac{\tilde{\vec{\mu}}_{21,32,31} \cdot \vec{E}_{a,c,b}}{\hbar}, \\
&\Gamma_{21,31,32} = \gamma_{21,31,32} + i(\omega_{21,31,32} - \omega_{a,b,c}).
\end{aligned}$$

A similar set of equations can be written for the case when the intraband transition is in the valence band (i.e. the triplet $|1\rangle, |2'\rangle, |3\rangle$ shown in Fig. 4.2(b).) From the second-order solution of density matrix element, we can derive the 2D second-order nonlinear polarization:

$$\begin{aligned}
\vec{P}^{(2)}(\omega) = &\sum_{1,2,3} \frac{\vec{\mu}_{23}(\tilde{\vec{\mu}}_{31} \cdot \vec{E}_b)(\tilde{\vec{\mu}}_{21}^* \cdot \vec{E}_a^*)/\hbar^2}{\gamma_{32} + i(\omega_{32} - \omega)} \left(\frac{f(\varepsilon_1) - f(\varepsilon_3)}{\gamma_{31} + i(\omega_{31} - \omega_b)} + \frac{f(\varepsilon_1) - f(\varepsilon_2)}{\gamma_{21} - i(\omega_{21} - \omega_a)} \right) \\
+ &\sum_{1,2'3} \frac{-\vec{\mu}_{12'}(\tilde{\vec{\mu}}_{31} \cdot \vec{E}_b)(\tilde{\vec{\mu}}_{32'}^* \cdot \vec{E}_a^*)/\hbar^2}{\gamma_{2'1} + i(\omega_{2'1} - \omega)} \left(\frac{f(\varepsilon_1) - f(\varepsilon_3)}{\gamma_{31} + i(\omega_{31} - \omega_b)} + \frac{f(\varepsilon_{2'}) - f(\varepsilon_3)}{\gamma_{32'} - i(\omega_{32'} - \omega_a)} \right),
\end{aligned} \tag{4.15}$$

where $f(\mathbf{k})$ is the occupation number of a given $\mathbf{k}$-state and $\mathbf{k}_2(\mathbf{k}_{2'})$ and $\mathbf{k}_3$ can

be expressed through $\mathbf{k}_1$ utilizing the selection rules that follow from the matrix elements of the interaction Hamiltonian: $\mathbf{k}_1 + \mathbf{q}_b = \mathbf{k}_3$; $\mathbf{k}_1(\mathbf{k}_{2'}) + \mathbf{q}_a = \mathbf{k}_2(\mathbf{k}_3)$. Here $\vec{v}_{\alpha\beta} = v_F\langle\alpha|\vec{\sigma}|\beta\rangle$ is the matrix element of the velocity operator, $\vec{\mu}_{\alpha\beta} = \dfrac{iev_F}{\omega_{\beta\alpha}}\langle\alpha|\vec{\sigma}|\beta\rangle$ is the transition dipole matrix moment, $\vec{\sigma} = (\hat{\sigma}_x, \hat{\sigma}_y)$ is a 2D Pauli matrix-vector, and $\omega_{\alpha\beta} = (\varepsilon(\mathbf{k}_\alpha) - \varepsilon(\mathbf{k}_\beta))/\hbar$ is the energy difference between electron states $|\alpha\rangle$ and $|\beta\rangle$. $\tilde{\vec{\mu}}_{\alpha\beta}$ is defined as $\frac{iev_F}{\omega}\langle\alpha|\vec{\sigma}|\beta\rangle$, which is the interaction Hamiltonian matrix element. We can then directly write down the corresponding second-order nonlinear susceptibility

$$\begin{aligned}\chi^{(2)}_{ijk} &= \frac{ge^2}{\hbar^2\omega_a\omega_b}\int\frac{d^2\mathbf{k}_1}{(2\pi)^2}\left\{\left[\frac{f(\mathbf{k}_1)-f(\mathbf{k}_3)}{\omega_{31}-\omega_b-i\gamma} + \frac{f(\mathbf{k}_1)-f(\mathbf{k}_2)}{-\omega_{21}+\omega_a-i\gamma}\right]\frac{\mu^i_{32}v^j_{31}v^k_{12}}{\omega_{32}-\omega-i\gamma}\right. \\ &- \left.\left[\frac{f(\mathbf{k}_1)-f(\mathbf{k}_3)}{\omega_{31}-\omega_b-i\gamma} + \frac{f(\mathbf{k}_{2'})-f(\mathbf{k}_3)}{-\omega_{32'}+\omega_a-i\gamma}\right]\frac{\mu^i_{2'1}v^j_{31}v^k_{2'3}}{\omega_{2'1}-\omega-i\gamma}\right\}, \qquad (4.16)\end{aligned}$$

An order of magnitude estimate for $\chi^{(2)}$ can be obtained if we take the limit of a degenerate electron distribution $k_BT \to 0$ and assume that $\omega \gg v_Fq, \gamma$ and $\omega_a \simeq \omega_b \equiv \bar{\omega}$. Then Eq. (4.16) gives

$$\chi^{(2)}_{xxx} \simeq \frac{e^3}{8\pi\hbar^2}\frac{g}{q\bar{\omega}\omega}\left\{\frac{\pi}{2} + \arctan\left(\frac{\bar{\omega}-2v_Fk_F}{\gamma}\right)\right\}, \qquad (4.17)$$

where k_F is the Fermi momentum. This approximate expression matches well the low-temperature dependence of the magnitude of $\chi^{(2)}$ for graphene shown in Fig. 4.3 as a function of the Fermi energy. With increasing Fermi energy, more states in the integral in Eq. (4.16) are fully occupied, which leads to a lower $\chi^{(2)}$. The value of $|\chi^{(2)}| \sim 10^{-6}$ esu is extremely high: if we divide it by a monolayer thickness ~ 0.3 nm to compare with bulk susceptibilities of other nonlinear materials, we obtain $|\chi^{(2)}_{bulk}| \sim 10^{-2}$ m/V, which is four orders of magnitude higher than $|\chi^{(2)}|$ measured at similar wavelengths in asymmetric coupled quantum-well structures[106].

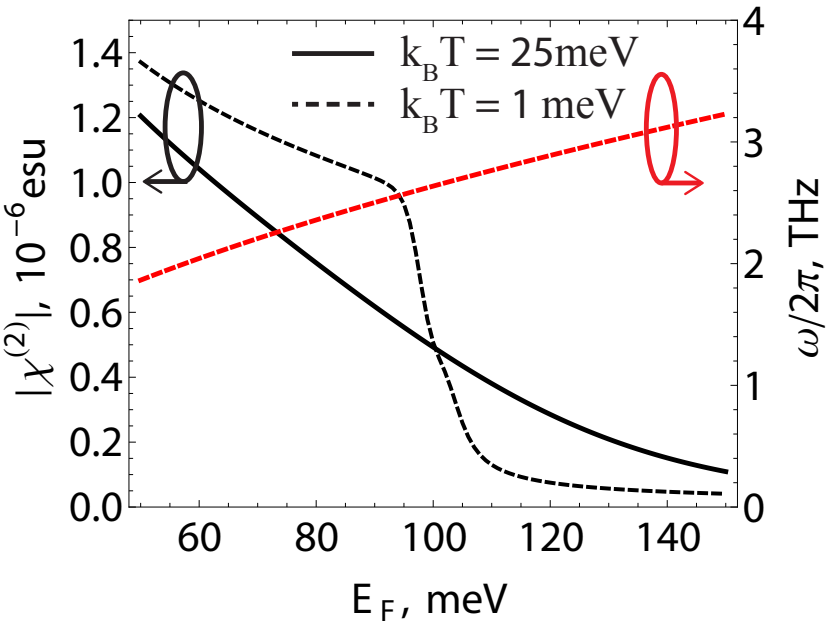

Figure 4.3: Magnitude of the 2D $\chi^{(2)}_{xxx}$ as a function of Fermi energy for a fixed incidence angle $\theta_a = \theta_b = \theta = 60°$ and fixed sum of the incident pump frequencies $\omega_a + \omega_b = 400$ meV. Red line is the generated plasmon frequency which satisfies the phase-matching condition and energy conservation at each E_f.

Note that, unlike the situation in a magnetized graphene with a discrete energy spectrum(Landau levels), here we don't have strong resonant enhancement of the nonlinear susceptibility at interband resonances: it is smeared out by integration over the continuous spectrum of electron momenta, as is clear from Eq. (4.17). Also, the second-order susceptibility is not affected by plasmon resonance; its large value is mainly due to large matrix elements of single-particle transitions. At the same time, the generated difference-frequency field does experience a strong enhancement

at the surface plasmon resonance, i.e. when the momentum and frequency of the generated difference-frequency photons satisfy the plasmon dispersion relation given by Eq. (4.10) or (1.29), depending on the layer geometry.

Indeed, as follows from Maxwell's equations, for a given 2D (surface) polarization $\vec{P} \propto \hat{x}e^{iqx-i\omega t}$ the generated surface plasmon mode has the electric field amplitude

$$E_{pl}(\omega, q) = -\frac{4\pi}{D(\omega, q)}P = -\frac{\chi^{(2)}_{xxx}(E_a)_x(E_b)_x}{\mathrm{Im}\tilde{\chi}_{\omega,q}}. \tag{4.18}$$

Here the second equality is valid when q and ω satisfy the plasmon dispersion equation, in which case the real part of the denominator $D(\omega, q)$ goes to zero and the generated field is greatly enhanced. For example, in monolayer graphene, when $q >> \sqrt{\epsilon_{1,2}}\omega/c$, we obtain

$$\mathrm{Im}\tilde{\chi}(\omega, q) \approx \frac{\gamma}{4\pi\omega}\frac{\epsilon_1 + \epsilon_2}{q}. \tag{4.19}$$

Fig. 4.4 shows the DFG efficiency η as a function of the plasmon frequency, where $\eta = \frac{I_{pl}}{I_a I_b}$ is defined as a ratio of the plasmon field intensity to the product of intensities of the incident pump fields. The generated frequency ω can be tuned by varying the pump frequencies $\omega_{a,b}$ or/and the angles of incidence $\theta_{a,b}$. The efficiency goes to zero at $\theta_{a,b} = 0$ (because $(E_{a,b})_x \propto \sin\theta_{a,b}$) and at $\theta_{a,b} = \pi/2$ when $\chi^{(2)}$ vanishes by symmetry. For mid-infrared pump frequencies, the generated signal can be tuned from 1 THz to several THz while still maintaining a high efficiency. For example, focusing two 1-W mid-infrared beams at wavelengths around 5 μm into the area of 100×100 μm^2 yields about 0.01 W of power in the in-plane propagating THz plasmon mode. Note that the DFG efficiency scales roughly as $1/\gamma^2$ according to

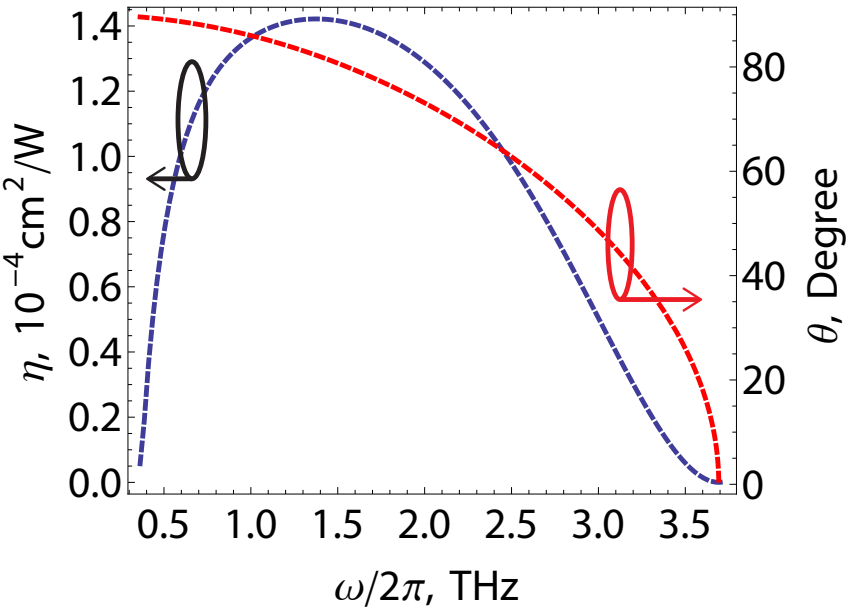

Figure 4.4: The DFG efficiency $\eta = \frac{I_{pl}}{I_a I_b}$ and incidence angle θ as a function of the plasmon frequency under the conditions of frequency and phase matching. The sum of the incident pump frequencies is fixed to $\omega_a + \omega_b = 400$ meV.

Eqs. (4.18),(4.19). The relaxation rate γ is 1 meV for the plots in Figs. 4.3, 4.4.

4.3 DFG in graphene/silicon-heterostructure waveguide

For integrated photonics and optoelectronics applications, it is desirable to avoid open optical paths and integrate all fields into a planar waveguide structure, see e.g. [52][106][107]. The DFG of surface plasmons can also be implemented in the integrated waveguide geometry in which both pump fields propagate as waveguide modes and overlap on the graphene or TI surface. The simplest geometry is a dielectric or semiconductor waveguide with graphene deposited at the interface between the core

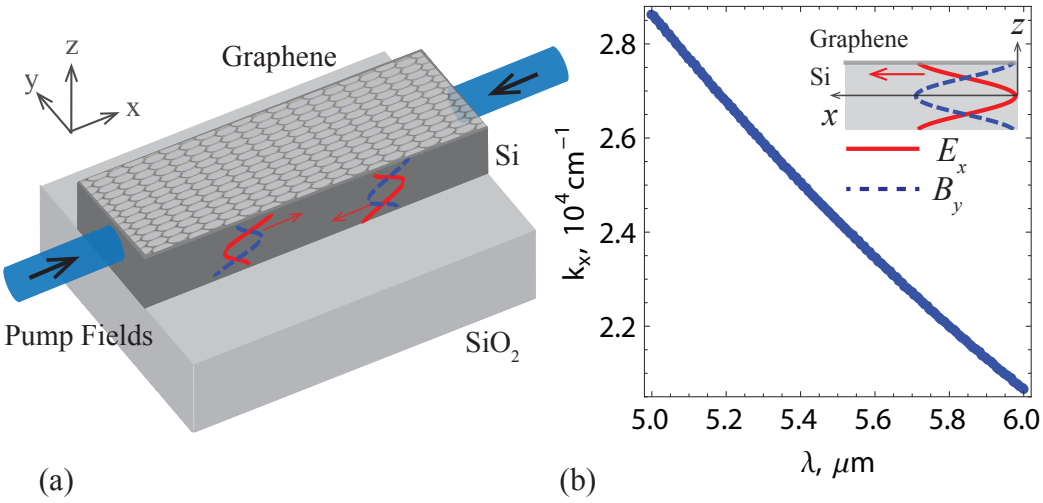

Figure 4.5: (a) Integrated waveguide geometry of DFG of surface plasmons by counter-propagating TM modes. Profiles of B_y and E_x field components are indicated in blue dashed and red lines, respectively. (b) The relation of in-plane momentum and wavelength of the fundamental mode in $1\mu m$-thick graphene/Si waveguide.

and the cladding. Fig. 4.5(a) shows one such example: a Si/SiO_2 waveguide in which the top cladding is air, with graphene deposited on the top. Another example would be a TI film in which the bulk TI material serves as a waveguide core. Consider a waveguide with a core layer of thickness d and dielectric constant ϵ_2 surrounded by cladding materials of lower dielectric constants ϵ_1 and ϵ_3. Let the two pump fields propagate in opposite directions as fundamental TM modes of the waveguide. They can be excited e.g. by z-polarized laser beams. In a TM mode the longitudinal

component of the electric field in the waveguide is

$$B_y = \begin{cases} \mathcal{B}e^{ik_x x}\cos(k_z d/2-\phi)\exp\kappa_3(d/2-z) & z > d/2 \\ \mathcal{B}e^{ik_x x}\cos(k_z z-\phi) & -d/2 < z < d/2 \\ \mathcal{B}e^{ik_x x}\cos(k_z d/2+\phi)\exp\kappa_2(d/2+z) & z < -d/2 \end{cases}$$

$$E_x = \begin{cases} \frac{ic\kappa_3\mathcal{B}}{\omega\epsilon_3}e^{ik_x x}\cos(k_z d/2-\phi)\exp\kappa_3(d/2-z) & z > d/2 \\ \frac{ick_z\mathcal{B}}{\omega\epsilon_1}e^{ik_x x}\sin(k_z z-\phi) & -d/2 < z < d/2 \\ -\frac{ic\kappa_2\mathcal{B}}{\omega\epsilon_2}e^{ik_x x}\cos(k_z d/2+\phi)\exp\kappa_2(d/2+z) & z < -d/2 \end{cases} \tag{4.20}$$

Here $k_z, \kappa_{2,3}$ satisfy $k_z^2+k_x^2=\epsilon_1\frac{\omega^2}{c^2}; -\kappa_2^2+k_x^2=\epsilon_2\frac{\omega^2}{c^2}; -\kappa_3^2+k_x^2=\epsilon_3\frac{\omega^2}{c^2}$. The boundary conditions give the relationship between waveguide mode frequency ω, k_z and ϕ

$$\begin{aligned} \tan k_z d &= \frac{k_z}{\epsilon_1}\left(\frac{\kappa_2}{\epsilon_2}+\frac{\kappa_3}{\epsilon_3}\right)\Big/\left[\left(\frac{k_z}{\epsilon_1}\right)^2-\frac{\kappa_2\kappa_3}{\epsilon_2\epsilon_3}\right]; \\ \tan 2\phi &= \frac{k_z}{\epsilon_1}\left(\frac{\kappa_2}{\epsilon_2}-\frac{\kappa_3}{\epsilon_3}\right)\Big/\left[\left(\frac{k_z}{\epsilon_1}\right)^2+\frac{\kappa_2\kappa_3}{\epsilon_2\epsilon_3}\right]. \end{aligned} \tag{4.21}$$

For example, Fig. 4.5(b) shows the relationship between the wavelength of the waveguide mode and the corresponding in-plane momentum of a $1\mu m$-thick graphene/Si waveguide. $E_x \propto \partial B_y/\partial z$ has a maximum near the interfaces $z = \pm d/2$, where $z = 0$ in the middle of the waveguide core. Strong overlap of the E_x components of the pump fields with a graphene layer is exactly what we need for efficient nonlinear

excitation of a surface plasmon at the difference frequency.

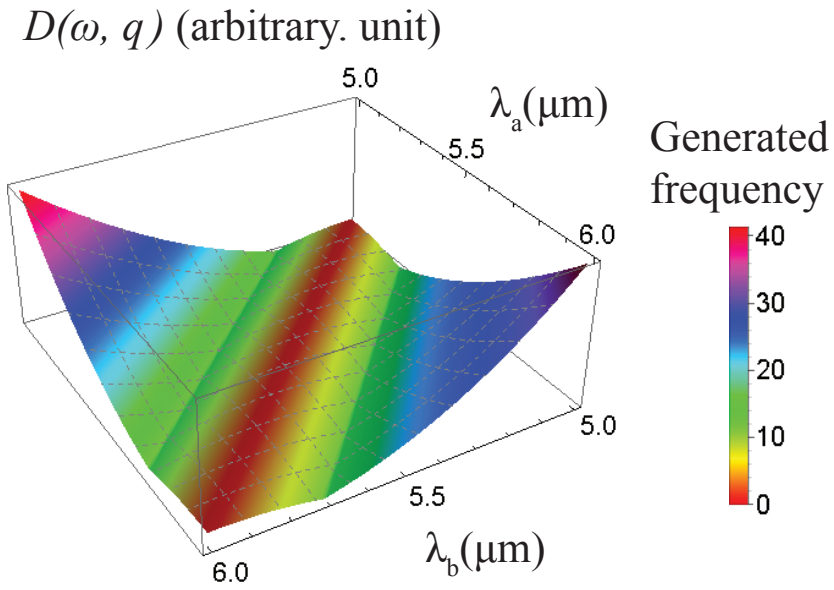

Figure 4.6: $D(\omega, q)$ for the difference frequency signal, with two given fundamental mode in the Mid-IR range, we set Fermi energy 50meV here.

For the E_x-fields in the two pump modes given by $E_a \sim \exp(iq_a x - i\omega_a t)$ and $E_b \sim \exp(-iq_b x - i\omega_b t)$, the second-order nonlinear interaction between the fields generates the 2D nonlinear polarization in graphene at the difference frequency $\omega = \omega_b - \omega_a$ and in-plane momentum $q = q_a + q_b$.

$$E_c(\omega, q) = \frac{-4\pi\chi^{(2)}_{xxx} E_a(\frac{d}{2}) E_b(\frac{d}{2})}{4\pi\tilde{\chi}_{\omega,q} + \epsilon_1/p_1 + \epsilon_3/p_3} \tag{4.22}$$

When ω and q satisfy the surface plasmon dispersion relation (i.e. $D(\omega, q) = 0$, shown in Fig. 4.6), the plasmon field excited by the nonlinear polarization experiences

a strong enhancement (as shown in Fig. 4.7):

$$E_c(\omega, q) = -\frac{\chi^{(2)}_{xxx} E_a(\frac{d}{2}) E_b(\frac{d}{2})}{\mathrm{Im}\tilde{\chi}(\omega, q)}. \tag{4.23}$$

Here we assumed that the pump fields are constant over the vertical confinement

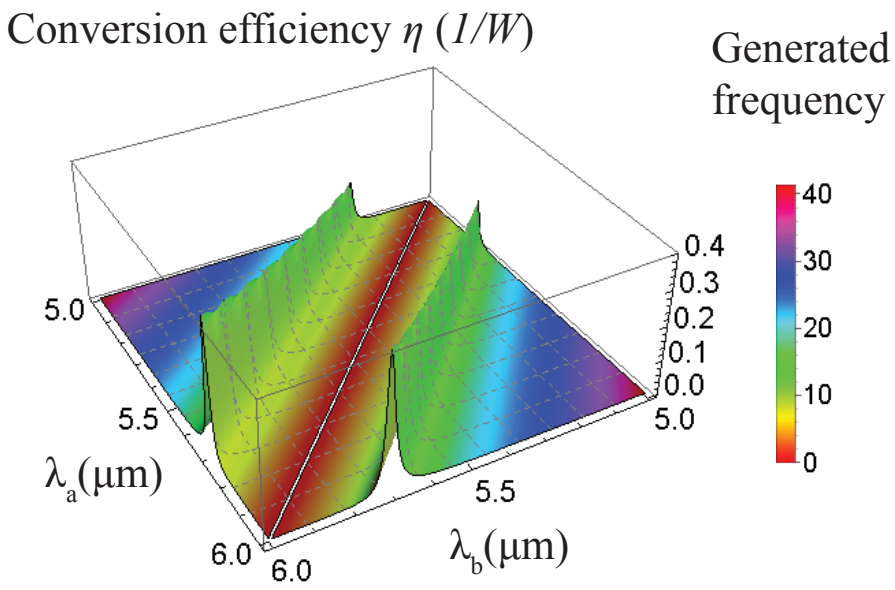

Figure 4.7: Difference frequency generation efficiency for two given fundamental mode in the same wavelength range($5 - 6\mu m$). We can easily observe the peak on the plasmon resonance points.

scale of the plasmon mode ~ 1 μm. In Fig. 4.7 and Fig. 4.8, the DFG efficiency is defined as a ratio of the Poynting flux in the surface plasmon mode to the product of Poynting fluxes of the TM modes of the pump fields. Using mid-IR quantum cascade lasers of a typical power 0.1-1 W as a pump, one can get about 1-10 mW of power in the coherent plasmon mode. We also performed similar calculations for

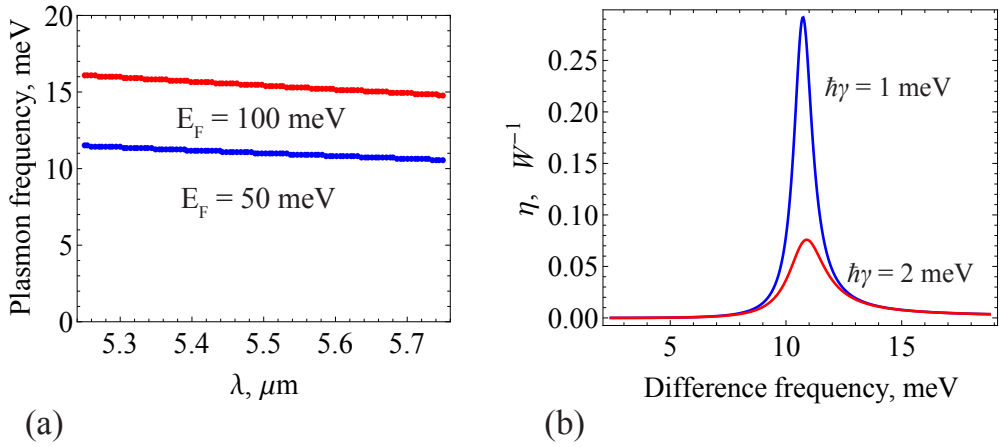

Figure 4.8: (a) Phase-matched plasmon frequency vs. wavelength of the fundamental TM mode for one of the pump fields in a 1-μm thick Si waveguide, for two values of Fermi energy. (b) DFG efficiency of surface plasmons for $E_F = 50$ meV and two values of the relaxation rate.

pump lasers at telecom wavelengths around 1.5 μm. In this case the phase-matched DFG of surface plasmons takes place around plasmon frequency 25-35 meV (for E_F of 50-100 meV) and the conversion efficiency is $\sim 10^{-4} - 10^{-5}$/W (shown in Fig. 4.9).

4.4 DFG in double layer graphene and topological insulator

For a thick slab of topological insulator or a double layer grpahene geometry, i.e. a large separation d between two massless Dirac surface states, the plasmon modes turn into two uncoupled monolayer modes. At the same time, for given identical surface currents $\mathbf{j} = \hat{\mathbf{x}} Re[J \exp(iqx - i\omega t)]$ generated on the two surfaces $z = \pm\frac{d}{2}$ by difference-frequency generation process, the Maxwell's equations admit an interesting solution: a TM mode which is completely confined inside the layer $|z| \leq \frac{d}{2}$, i.e. the electromagnetic field is zero outside the layer. Indeed, Maxwell's equations for a TM

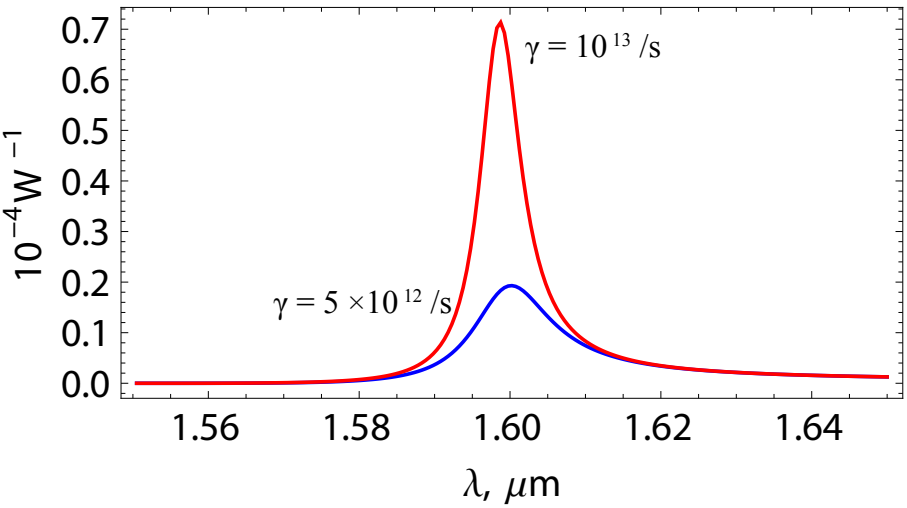

Figure 4.9: Fix one pump field at $1.55\mu m$, the difference frequency generation efficiency is a function of the tunable pump field, which reaches the peak value at plasmon resonance point. The peak efficiency scales as $1/\gamma^2$. Here Fermi energy in graphene is set as $50meV$.

mode in a bulk region with dielectric constant ϵ are:

$$iqE_x = -\frac{\partial E_z}{\partial x}, \quad B_y = -\frac{\omega\epsilon}{qc}E_z.$$

Here E_x satisfies the Helmholtz equation

$$\left(\frac{\partial^2}{\partial z^2} - q^2 + \epsilon\frac{\omega^2}{c^2}\right)E_x = 0.$$

Consider a symmetric solution

$$E_x = E_0 \cos pz, \quad E_z = -i\frac{q}{p}E_0 \sin pz, \quad B_y = i\frac{\epsilon\omega}{pc}E_0 \sin pz,$$

with the transverse wave number $p = \sqrt{\epsilon\frac{\omega^2}{c^2} - q^2} > 0$, i.e. this mode is not a surface mode. For the values of q satisfying

$$\sqrt{\epsilon\frac{\omega^2}{c^2} - q^2}d = N\pi, N = 1, 2, 3, ... \tag{4.24}$$

One can find solutions with zero field outside the layer, i.e. satisfying the boundary condition:

$$E_x(\pm\frac{d}{2}) = 0, \quad B_y(\frac{d}{2}) = \pm\frac{4\pi}{c}J, \quad E_z(\pm\frac{d}{2}) = \pm\frac{4\pi q}{\epsilon\omega}J.$$

The resulting field amplitude is then solved as

$$E_0 = -i\frac{4\pi q}{\epsilon\omega}J. \tag{4.25}$$

The field amplitude E_0 does not have a surface plasmon resonance enhancement $\propto \frac{\omega}{\gamma}$ as compared to the field of surface plasmon mode. However, this symmetric mode can directly propagate into the vacuum or be coupled into dielectric waveguide.

5. OPTICAL RESPONSE OF TOPOLOGICAL INSULATORS

3D topological insulator material (e.g. Bi_2Se_3 and Sb_2Te_3) is characterized by a surface state consisting of a single Dirac cone, where spin and momentum are strongly coupled in the Hamiltonian

$$\mathcal{H}(k) = E_0 - Dk^2 + \hbar v_F(k_y\sigma_x - k_x\sigma_y). \tag{5.1}$$

Here v_F is the Fermi velocity, and $\sigma_{x,y}$ describes the spin. The spin-momentum coupling demonstrates the helical Dirac fermion nature of topological surface state. The time-reversal symmetry protects the surface state from backscattering and ensures its robustness. For low-energy excitations in the terahertz or long-wavelength mid-infrared region below 100 meV, it is safe to only keep the linear momentum term and neglect higher order corrections in the Hamiltonian; see Fig. 5.1. The effective Hamiltonian is then simplified to

$$\mathcal{H}(k) = E_0 + \hbar v_F(k_y\sigma_x - k_x\sigma_y) \tag{5.2}$$

for calculations. In the magnetic field, the effective-mass Hamiltonian is rewritten using Peierls substitution as :

$$\mathcal{H}(\pi) = E_0 + \hbar v_F(\pi_y\sigma_x - \pi_x\sigma_y). \tag{5.3}$$

The external magnetic field breaks the time-reversal symmetry, and quantized the linear bandstructure into non-equidistant surface Landau levels. Due to the Dirac fermion nature of a topological surface state, it is straightforward to study the optical

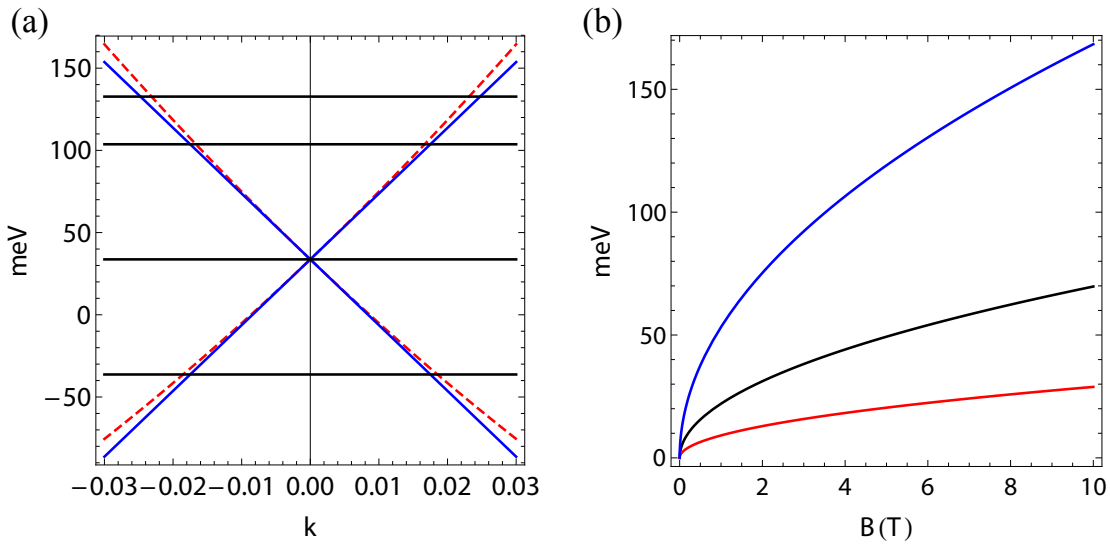

Figure 5.1: (a) Energy bands of the surface states near the Γ point at zero magnetic field (with 2nd order correction shown by dashed line), and energies of Landau levels in a magnetic field of 10 T (horizontal lines). (b) Landau level energies as a function of the magnetic field for Bi_2Se_3.

properties and relevant applications of topological insulator in analogy to the optical applications of graphene. For example, very similar to graphene, the low energy optical absorbance of thin film Bi_2Se_3 is a universal quantity $\pi\alpha/2$[41]. The topological surface state also exhibits a series of mangeto-optical Faraday and Kerr effects[42]. In addition, topological surface state possesses a much longer lifetime due to the topological protection, making topological insulator a promising material for nonlinear signal generation and quantum information. However, up to now, few studies on optical properties of the topological surface states have been reported. In this chapter, we present theoretical estimation for the linear and nonlinear optical response of topological surface states in a external magnetic field. In addition, we notice that the external magnetic field breaks the time-reversal symmetry, and introduces finite off-diagonal elements into the dielectric tensor, making electrons selectively couple to

circularly polarized light with opposite sense. As a result, we believe that topological insulators also exhibit promising applications in the polarization optics.

5.1 Linear optical response

Very similar to graphene, linear optical response of topological insulator in a magnetic field exhibits strong cyclotron resonance features, which mainly come from inter-surface-Landau-level transitions. Transitions between adjacent surface Landau levels in topological insulator fall into mid-infrared to terahertz (THz) range for a magnetic field in the range 0.01-10 Tesla. Consider an incident classical optical field

$$\vec{E} = E(\omega)\exp(-i\omega t)\hat{e}$$

polarized in the x-y plane along vector $\hat{e}$. As usual, we define the left-hand circular polarization vector as $\hat{e}_{LHS} = [\hat{x} - i\hat{y}]/\sqrt{2}$ and the right-hand circular polarization vector $\hat{e}_{RHS} = [\hat{x} + i\hat{y}]/\sqrt{2}$. To include interaction with the optical field, we add its vector potential , $\vec{A}_{opt} = ic\vec{E}/\omega$, to the vector potential of the magnetic field in the generalized momentum operator $\hat{\vec{\pi}}$ in the Hamiltonian. This results in adding the interaction Hamiltonian $\hat{\mathcal{H}}_{int}$ to $\mathcal{H}(\pi)$(Eq. (5.3)), where

$$\hat{\mathcal{H}}_{int} = \upsilon_F(\hat{\vec{\sigma}} \times \frac{e}{c}\vec{A}_{opt})_z \equiv -(\tilde{\vec{\mu}} \times \vec{E}(\omega))_z e^{-i\omega t}, \tag{5.4}$$

with $\tilde{\vec{\mu}}$ defined as $\frac{ie\upsilon_F}{\omega}\vec{\sigma}$. Unlike the interaction Hamiltonian $\mathcal{H}_{int}$ for an electron with a parabolic dispersion, there are no higher order terms such as π^2 near the Dirac point in a topological insulator, so that even for a relatively strong optical field the interaction Hamiltonian is still linear with respect to $\vec{A}_{opt}$. Furthermore, $\mathcal{H}_{int}$ does not contain the momentum operator; it is simply determined by the Pauli matrix vector $\hat{\vec{\sigma}}$. The matrix element of the optical transition between different

surface Landau levels is given by

$$\langle m|\hat{\mathcal{H}}_{int}|n\rangle = \frac{iev_F}{\omega}\langle m|\sigma_x E_y - \sigma_y E_x|n\rangle\,,$$

where $|m\rangle, |n\rangle$ denote surface Landau level with energy index m and n (Eq. 1.18). $\langle m|\hat{\mathcal{H}}_{int}|n\rangle$ is nonzero only when

$$|m| - 1 = |n| \quad or \quad |m| = |n| - 1.$$

As a result, the selection rule for the allowed transitions turns out to be

$$\Delta|n| = \pm 1, \tag{5.5}$$

where n is the energy quantum number. Denoting f and i as the quantum numbers of the final and initial state, we observe that $\hat{e}_{RHS}$ photons are absorbed when $|f| = |i| - 1$ while an absorption of a $\hat{e}_{LHS}$ photon leads to the transition $|f| = |i| + 1$. The resulting selection rule for inter-surface-Landau-level transitions of topological insulator is the same as that for monolayer graphene. Comparing with a typical selection rule in a traditional 2D system, $\Delta n = \pm 1$, the transitions with Δn greater than 1 are allowed in topological insulator surface layer, for example, from $i = -1$ to $f = 2$, which leads to an efficient resonant nonlinear mixing. Mid/far-infrared optical absorption between surface Landau levels of topological insulator has been experimentally observed in real materials[44][45].

In order to calculate the 2D optical polarization using density-matrix formalism, we need to know the dipole moment matrix associated with inter-surface-Landau-

level transitions. To calculate this, we first evaluate the commutator

$$[\vec{r}, \mathcal{H}] = \upsilon_F[\vec{r}, (\hat{\vec{\sigma}} \times \hat{\vec{p}})_z] + \upsilon_F[\vec{r}, (\hat{\sigma} \times \frac{e}{c}\vec{A})_z].$$

The second term on the right-hand side is zero because $\vec{A}$ is a function of $\vec{r}$. So the commutator of $\hat{\vec{r}}$ and the Hamiltonian is

$$[\vec{r}, \mathcal{H}] = \upsilon_F[\vec{r}, \sigma_x\hat{p}_y - \sigma_y\hat{p}_x] = i\hbar\upsilon_F(\sigma_x\hat{y} - \sigma_y\hat{x}).$$

Choosing the eigen states of $\mathcal{H}$ as the basis, we obtain

$$\langle m|[\vec{r}, \mathcal{H}]|n\rangle = \langle m|\vec{r}\mathcal{H}|n\rangle - \langle m|\mathcal{H}\vec{r}|n\rangle = (\varepsilon_n - \varepsilon_m)\langle m|\vec{r}|n\rangle,$$

where ε_n and ε_m are the eigen energies of states $|n\rangle$ and $|m\rangle$. So the dipole matrix element of a closed system is defined as

$$\vec{\mu}_{mn} = e \cdot \langle m|\vec{r}|n\rangle = \frac{i\hbar\upsilon_F e}{\varepsilon_n - \varepsilon_m}\langle m|\sigma_x\hat{y} - \sigma_y\hat{x}|n\rangle. \tag{5.6}$$

Similarly to the matrix elements of the interaction Hamiltonian $\langle m|\hat{\mathcal{H}}_{int}|n\rangle$, the dipole matrix elements are determined by elements of the Pauli matrix $\langle m|\hat{\sigma}|n\rangle$ as well. In particular, $\vec{\mu}_{mn}$ is nonzero when $|m| = |n| \pm 1$.

Recall the first-order (linear) solution of the density matrix element can be calculated from the iteration formula Eq. (2.10) and Eq. (5.4):

$$\rho^{(1)}_{nm} = \int_0^t \frac{-i}{\hbar}[\hat{H}_{int}(t'), \hat{\rho}^{(eq)}]_{nm} \exp\left[(i\omega_{nm} + \gamma_{nm}) \cdot (t' - t)\right]dt', \tag{5.7}$$

where

$$
\begin{aligned}
[\hat{H}_{int}(t'),\hat{\rho}^{(eq)}]_{nm} &= \sum_{v}\left[(\tilde{\vec{\mu}}_{nv}\times\tilde{E}(t'))_z\rho^{(eq)}_{vm}-\rho^{(eq)}_{nv}(\tilde{\vec{\mu}}_{vm}\times\tilde{E}(t'))_z\right] \\
&= \left(\rho^{(eq)}_{mm}-\rho^{(eq)}_{nn}\right)(\tilde{\vec{\mu}}_{nm}\times\tilde{E}(t'))_z.
\end{aligned}
$$

This yields the 2D first-order polarization in the form

$$
\begin{aligned}
\tilde{P}^{(1)}(\omega) &= N\mathrm{tr}\left(\hat{\rho}^{(1)}\hat{\mu}\right) \\
&= N\sum_{nm}\frac{\rho^{(eq)}_{mm}-\rho^{(eq)}_{nn}}{\hbar}\cdot\frac{\left(\tilde{\vec{\mu}}_{nm}\times\hat{e}\right)_z\vec{\mu}_{mn}}{(\omega_{nm}-\omega)-i\gamma_{nm}}E(\omega)\exp\left(-i\omega t\right). \qquad (5.8)
\end{aligned}
$$

Here we have defined

$$
\tilde{\vec{\mu}}\equiv\frac{iev_F}{\omega}\vec{\sigma},\quad \langle m|\tilde{\vec{\mu}}|n\rangle\equiv\frac{iev_F}{\omega}\langle m|\vec{\sigma}|n\rangle;
$$

N is the 2D (sheet) electron density, which equals to $g\cdot N_\Phi = g/(2\pi l_c^2)$. Here $g=1$ for a single topological surface layer, and $g=g_s=2$ for a ultrathin topological insulator film. The corresponding linear susceptibility tensor is then given by:

$$
\chi^{(1)}_{ij}(\omega)=N\sum_{nm}\frac{\rho^{(eq)}_{mm}-\rho^{(eq)}_{nn}}{\hbar}\frac{\epsilon_{ki'j}\tilde{\vec{\mu}}^{i'}_{nm}\vec{\mu}^{i}_{mn}}{(\omega_{nm}-\omega)-i\gamma_{nm}} \qquad (5.9)
$$

For a left-hand circularly polarized optical field, the circular polarization vector $\hat{e}$ is $\hat{e}_{LHS}=[\hat{x}-i\hat{y}]/\sqrt{2}$, and the term $\left(\tilde{\vec{\mu}}_{nm}\times\hat{e}\right)_z$ in the above expression is nonzero only when $|n|=|m|-1$. On the other hand, for a right-hand circularly polarized optical field the term is nonzero only when $|m|=|n|-1$. This corresponds to the polarization selection rules that were already derived above. We here explicitly give the linear

optical susceptibility for left/right-hand circularly polarized optical field:

$$\begin{aligned}\chi^{(1)}(\omega,\hat{e}_{LHS}) &= \sum_{|n|=|m|-1}\frac{-gC_m^2C_n^2e^2\upsilon_F^2}{\pi l_c^2\hbar\omega\omega_{nm}}\cdot\frac{\rho_{mm}^{(eq)}-\rho_{nn}^{(eq)}}{\omega_{nm}-\omega-i\gamma_{nm}}\\ \chi^{(1)}(\omega,\hat{e}_{RHS}) &= \sum_{|m|=|n|-1}\frac{-gC_m^2C_n^2e^2\upsilon_F^2}{\pi l_c^2\hbar\omega\omega_{nm}}\cdot\frac{\rho_{mm}^{(eq)}-\rho_{nn}^{(eq)}}{\omega_{nm}-\omega-i\gamma_{nm}}\end{aligned} \tag{5.10}$$

Different from the constant high-frequency absorbance of topological insulator at zero magnetic field[41], the absorption coefficient in a high magnetic field shows a series of peaks due to inter-surface-Landau level transitions, as shown in Fig. 5.2. From the standard expression for a weak absorption

$$\alpha \simeq \frac{4\pi\omega}{c}\mathrm{Im}[\chi^{(1)}(\omega)], \tag{5.11}$$

combining with Eq. (5.10), we can write down the absorption coefficient of a 2D topological surface layer for left/right-hand circularly polarized light :

$$\begin{aligned}\alpha(\omega,\hat{e}_{LHS}) &= \sum_{|n|=|m|-1}\frac{-4gC_m^2C_n^2e^2\upsilon_F^2\gamma_{nm}}{l_c^2\hbar c\omega_{nm}}\cdot\frac{\rho_{mm}^{(eq)}-\rho_{nn}^{(eq)}}{(\omega_{nm}-\omega)^2+\gamma_{nm}^2}\\ \alpha(\omega,\hat{e}_{RHS}) &= \sum_{|m|=|n|-1}\frac{-4gC_m^2C_n^2e^2\upsilon_F^2\gamma_{nm}}{l_c^2\hbar c\omega_{nm}}\cdot\frac{\rho_{mm}^{(eq)}-\rho_{nn}^{(eq)}}{(\omega_{nm}-\omega)^2+\gamma_{nm}^2}\end{aligned} \tag{5.12}$$

The Faraday rotation angle can be calculated in a similar way. In the limit $\frac{\omega_c e^2}{\gamma\hbar c} \ll 1$, the standard formula for Faraday rotation holds:

$$\Delta\theta \simeq \frac{4\pi\omega}{c}\mathrm{Re}[\chi^{(1)}(\omega)]. \tag{5.13}$$

The Faraday rotation angle for left/right-hand circularly polarized optical field is

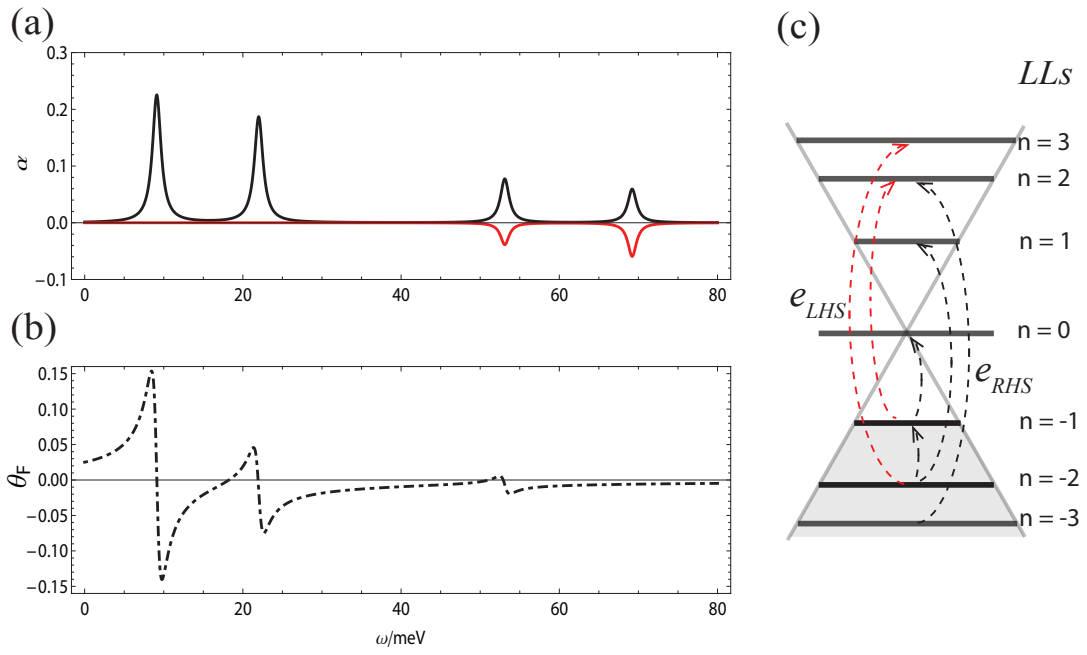

Figure 5.2: 1T magnetic field, half-filled surface LL n=-1. (a) absorption coefficient. The upper half is $\hat{e}_{RHS}$ photon absorbance, and the other half corresponds to $\hat{e}_{LHS}$ photon absorbance; (b) Faraday rotation angle. Here γ is chosen as $10^{12}s^{-1}$.

then given by:

$$\begin{aligned}\Delta\theta(\omega,\hat{e}_{LHS}) &= \sum_{|n|=|m|-1}\frac{-4gC_m^2C_n^2e^2v_F^2}{l_c^2\hbar c\omega_{nm}}\cdot\frac{(\rho_{mm}^{(eq)}-\rho_{nn}^{(eq)})(\omega_{nm}-\omega)}{(\omega_{nm}-\omega)^2+\gamma_{nm}^2}\\ \Delta\theta(\omega,\hat{e}_{RHS}) &= \sum_{|m|=|n|-1}\frac{-4gC_m^2C_n^2e^2v_F^2}{l_c^2\hbar c\omega_{nm}}\cdot\frac{(\rho_{mm}^{(eq)}-\rho_{nn}^{(eq)})(\omega_{nm}-\omega)}{(\omega_{nm}-\omega)^2+\gamma_{nm}^2}\end{aligned}\tag{5.14}$$

Note that the standard formula for weak absorption and Faraday rotation is accurate only when $\frac{\omega_c e^2}{\gamma\hbar c}\ll 1$. And they can only be applied to estimate absorbance and Faraday rotation angle for a single surface layer of 3D topological insulator or a ultrathin topological insulator film, where the thickness is much smaller than the

wavelength of the incident field.

5.2 Polarization optics of topological insulators

The external magnetic field breaks the time-reversal symmetry of topological surface state, and introduces finite off-diagonal elements into the dielectric tensor. As a result, topological insulator selectively responds to circularly polarized light with opposite sense. The ultrahigh surface mobility of topological insulator further enhances the classical Faraday effect. These interesting properties make topological insulator a promising material to build circular polarizers.

Time-reversal symmetry of topological insulator is broken in a global magnetic field, but the surface Landau states still possess a much longer lifetime than the bulk states, which is demonstrated in recent experiments[108][109][110]. This phenomenon can be explained by the helical nature of topological surface states, which persists in a perpendicular magnetic field. Recall the wavefunctions of surface Landau level in the Landau gauge, they are 1D plane waves along y direction whose central x positions linearly depend on k_y as $x = l_c^2 k_y$. So these 1D modes with opposite momentum are spatially separated on the surface layer. Such a protection mechanism also exists in the 2D quantum Hall electron systems. However, in topological insulator, the surface Landau levels are further protected by the helical nature of the surface states, which limits the scattering channel due to impurities and disorder[110]. As a result, the lifetime of surface Landau states is mainly affected by the electron-electron interaction, which is in the order of 10^{-1} ps[110]. The corresponding mean free path is around 80 nm.

Beyond the limit $\frac{\omega_c}{\gamma}\frac{e^2}{\hbar c} \ll 1$, we can no longer use the standard formulas (Eqs. 5.11, 5.13) to describe the light-matter interaction. We here need to solve Maxwell's equations strictly together with polarization-induced surface current $\vec{j}_\perp =$

$-i\omega\tilde{\chi}_\omega\vec{E}_\perp$. Here $\vec{E}_\perp$ is the in-plane electric field, and $\tilde{\chi}_\omega$ is the linear susceptibility tensor. When the incident field resonates with an allowed inter-surface-Landau-level transition ($\omega \approx \omega_{nm}$), the cyclotron resonance features are mainly dominated by this particular transition. We thus write the linear optical susceptibility as:

$$\chi^{(1)}_{ij}(\omega) = N\frac{\rho^{(eq)}_{mm} - \rho^{(eq)}_{nn}}{2\hbar}\left\{\frac{\epsilon_{ki'j}\tilde{\vec{\mu}}^{i'}_{nm}\vec{\mu}^{i}_{mn}}{\omega_{nm} - \omega - i\gamma} + \frac{\epsilon_{ki'j}\tilde{\vec{\mu}}^{i'}_{mn}\vec{\mu}^{i}_{nm}}{\omega_{nm} + \omega + i\gamma}\right\} \tag{5.15}$$

The resulting linear susceptibility tensor is in a gyrotropic form:

$$\tilde{\chi} = \begin{bmatrix} \chi_{xx} & \chi_{xy} \\ \chi_{yx} & \chi_{yy} \end{bmatrix} = \begin{bmatrix} \chi_\perp & -ig \\ ig & \chi_\perp \end{bmatrix}, \tag{5.16}$$

where $\chi_\perp$ and g are calculated from Eq. (5.9) directly:

$$\begin{aligned} \chi_\perp &= \frac{\Omega^2_{nm}}{\omega^2_{nm} - (\omega + i\gamma)^2}; \\ g &= s \cdot \frac{\omega + i\gamma}{\omega_{nm}}\frac{\Omega^2_{nm}}{\omega^2_{nm} - (\omega + i\gamma)^2}, \end{aligned} \tag{5.17}$$

with

$$\Omega^2_{nm} = \frac{C^2_m C^2_n(\rho^{(eq)}_{mm} - \rho^{(eq)}_{nn})Ne^2\upsilon^2_F}{\hbar\omega},$$

$$s = \begin{cases} +1, & |n| = |m| - 1 \\ -1, & |m| = |n| - 1 \end{cases}.$$

Let the electromagnetic wave with in-plane electric field $\tilde{E}^i = \tilde{E}^i_x\hat{x} + \tilde{E}^i_y\hat{y}$ incident from $z < 0$ onto the surface layer of topological insulator, the field components of the incident wave are in the form:

$$\tilde{E}^i_x = V_0 e^{ipz}, \tilde{E}^i_z = -\tan\theta V_0 e^{ipz}, \tilde{B}^i_y = \cos\theta^{-1} V_0 e^{ipz};$$

$$\tilde{E}_y^i = W_0 e^{ipz}, \tilde{B}_x^i = -\cos\theta W_0 e^{ipz}, \tilde{B}_z^i = \sin\theta W_0 e^{ipz}.$$

The corresponding transmitted field (denoted with superscript t) and reflected field (denoted with superscript r) are:

$$\tilde{E}_x^t = V_+ e^{+ipz}, \tilde{E}_z^t = -\tan\theta V_+ e^{+ipz}, \tilde{B}_y^t = +\cos\theta^{-1} V_+ e^{+ipz};$$
$$\tilde{E}_y^t = W_+ e^{+ipz}, \tilde{B}_x^t = -\cos\theta W_+ e^{+ipz}, \tilde{B}_z^t = \sin\theta W_+ e^{+ipz}.$$

$$\tilde{E}_x^r = V_- e^{-ipz}, \tilde{E}_z^r = +\tan\theta V_- e^{-ipz}, \tilde{B}_y^r = -\cos\theta^{-1} V_- e^{-ipz};$$
$$\tilde{E}_y^r = W_- e^{-ipz}, \tilde{B}_x^r = +\cos\theta W_- e^{-ipz}, \tilde{B}_z^r = \sin\theta W_- e^{-ipz}.$$

Here $V_{0,\pm}$ and $W_{0,\pm}$ are unknown amplitudes. Plug the above expressions into Maxwell's equations and apply boundary conditions on the surface $z = 0$:

$$\begin{aligned}
&\tilde{E}_z(+0) - \tilde{E}_z(-0) = 4\pi\rho_\perp; \\
&\tilde{E}_x(+0) = \tilde{E}_x(-0), \quad \tilde{E}_y(+0) = \tilde{E}_y(-0); \\
&\tilde{B}_z(+0) = \tilde{B}_z(-0); \\
&\tilde{B}_x(+0) - \tilde{B}_x(-0) = \frac{4\pi j_y}{c}, \quad \tilde{B}_y(+0) - \tilde{B}_y(-0) = -\frac{4\pi j_x}{c}.
\end{aligned} \tag{5.18}$$

We obtain:

$$\begin{aligned}
&V_+ = V_0 + V_-; \\
&W_+ = W_0 + W_-; \\
&V_+ - (V_0 - V_-) = i\frac{4\pi\omega}{\cos\theta c}(\chi_{xx} V_+ + \chi_{xy} W_+); \\
&W_+ - (W_0 - W_-) = i\frac{4\pi\omega}{\cos\theta c}(\chi_{yy} W_+ + \chi_{yx} V_+).
\end{aligned}$$

Define the in-plane electric field vector $\tilde{\mathcal{E}}_\perp$ and polarization coefficient K as:

$$\tilde{\mathcal{E}}_\perp = \begin{pmatrix} \tilde{E}_y \\ \tilde{E}_x \end{pmatrix}; K = \frac{\tilde{E}_y}{\tilde{E}_x}.$$

The in-plane electric component of transmitted optical field is then derived as:

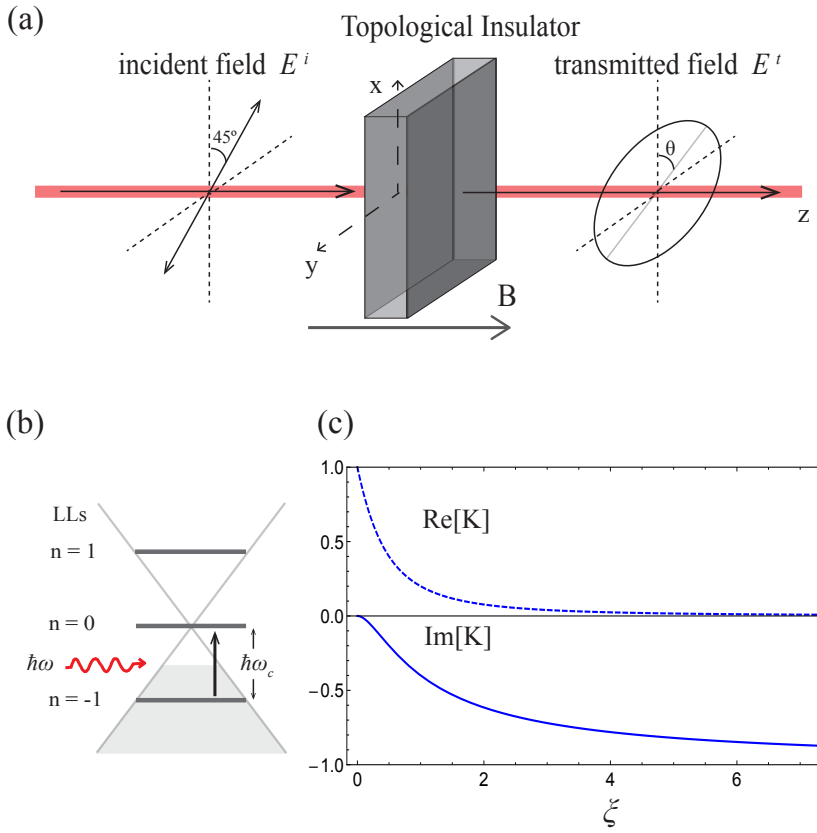

Figure 5.3: (a)A proposed experiment geometry: the incident field is linearly polarized with orientation angle $\frac{\pi}{4}$. (b)The corresponding inter-surface-Landau-level transition scheme for incident frequency $\omega \approx \omega_c$. Here Fermi level is placed between surface Landau levels -1 and 0, so photons are coupled with inter-surface-Landau-level transition $-1 \to 0$. (c)Polarization coefficient(K) of the transmitted optical field, as a function of ξ. The slab thickness is chosen as 0.01λ in the plot.

$$\begin{pmatrix} \tilde{E}_y^t \\ \tilde{E}_x^t \end{pmatrix}_{z=0+} = \frac{1}{(1-\kappa\chi_{xx})^2 + (\kappa\chi_{xy})^2} \begin{bmatrix} 1-\kappa\chi_{xx} & \kappa\chi_{yx} \\ \kappa\chi_{xy} & 1-\kappa\chi_{yy} \end{bmatrix} \begin{pmatrix} \tilde{E}_y^i \\ \tilde{E}_x^i \end{pmatrix}_{z=0-}, \tag{5.19}$$

where $\kappa \equiv i\frac{2\pi\omega}{\cos\theta c}$. The corresponding transmission matrix and polarization coefficient of the transmitted wave are

$$T = \frac{\begin{bmatrix} 1-\kappa\chi_{xx} & \kappa\chi_{yx} \\ \kappa\chi_{xy} & 1-\kappa\chi_{yy} \end{bmatrix}}{(1-\kappa\chi_{xx})^2 + (\kappa\chi_{xy})^2},$$

$$K^t = \frac{K(1-\kappa\chi_{xx}) + \kappa\chi_{yx}}{\kappa\chi_{xy}K + (1-\kappa\chi_{yy})}. \tag{5.20}$$

On the surface plane $z = 0$, the in-plane electric field components of the incident, reflected and transmitted fields satisfy the boundary conditions:

$$\begin{cases} \tilde{E}_x^t(z=0) = \tilde{E}_x^i(z=0) + \tilde{E}_x^r(z=0); \\ \tilde{E}_y^t(z=0) = \tilde{E}_y^i(z=0) + \tilde{E}_y^r(z=0). \end{cases} \tag{5.21}$$

So the in-plane electric vector of the reflected field is in the form of

$$\begin{pmatrix} \tilde{E}_y^r \\ \tilde{E}_x^r \end{pmatrix}_{z=0-} = \begin{pmatrix} \tilde{E}_y^t \\ \tilde{E}_x^t \end{pmatrix}_{z=0+} - \begin{pmatrix} \tilde{E}_y^i \\ \tilde{E}_x^i \end{pmatrix}_{z=0-} = (T-I) \cdot \begin{pmatrix} \tilde{E}_y^i \\ \tilde{E}_x^i \end{pmatrix}_{z=0-} \tag{5.22}$$

The corresponding reflection matrix of the in-plane electric field can then be written as

$$R = T - I. \tag{5.23}$$

As a result, beyond the limit that $\frac{\omega_c}{\gamma}\frac{e^2}{\hbar c} \ll 1$, even one single surface layer of 3D topological insulator possesses a strong reflection to the field component that resonates

with an allowed inter-surface-Landau-level transition.

For the TI slab geometry(Fig. 5.3(a)), with localized surface state on the top and bottom surfaces, one has to take multiple optical reflections between the two surface layers into account, especially when the slab thickness d is comparable to the optical wavelength. Consider the optical field normally incident from $z < -d/2$ onto the slab, one can similarly derive the transmission matrix for the bottom and top surfaces respectively:

$$\begin{aligned} T_1 &= \frac{2\begin{bmatrix} n+1-2\kappa\chi_\perp & 2\kappa ig \\ -2\kappa ig & n+1-2\kappa\chi_\perp \end{bmatrix}}{(n+1-2\kappa\chi_\perp)^2-(2\kappa g)^2} \\ T_2 &= \frac{2\begin{bmatrix} n^2+n-2n\kappa\chi_\perp & 2n\kappa ig \\ -2n\kappa ig & n^2+n-2n\kappa\chi_\perp \end{bmatrix}}{(n+1-2\kappa\chi_\perp)^2-(2\kappa g)^2}. \end{aligned} \tag{5.24}$$

Here n is the high-frequency refractive index of bulk topological insulator. The transmission and reflection matrix on each surface layer follow the simple relation $T_{1,2} = R_{1,2}+I$, derived from the boundary conditions on both surfaces. Take multiple reflections between the two surfaces into account:

$$\begin{aligned} \tilde{\mathcal{E}}^t_\perp(d/2) &= T_2PT_1\cdot\tilde{\mathcal{E}}^i_\perp + T_2PR_2PR_2PT_1\cdot\tilde{\mathcal{E}}^i_\perp + ... \\ &= T_2\left(P+P^3R_2R_2+P^5R_2R_2R_2R_2+...\right)T_1\cdot\tilde{\mathcal{E}}^i_\perp \\ &= T_2P\left(I-P^2R_2R_2\right)^{-1}T_1\cdot\tilde{\mathcal{E}}^i_\perp(-d/2). \end{aligned}$$

The final transmitted in-plane electric field is

$$\begin{pmatrix} \tilde{E}_y^t \\ \tilde{E}_x^t \end{pmatrix}_{z=\frac{d}{2}+} = e^{i\frac{n\omega d}{c}} T_2 \left(I - e^{i\frac{2n\omega d}{c}} R_2 R_2 \right)^{-1} T_1 \begin{pmatrix} \tilde{E}_y^i \\ \tilde{E}_x^i \end{pmatrix}_{z=\frac{-d}{2}-} . \tag{5.25}$$

One can also apply this technics to study the polarization optics of double-layer

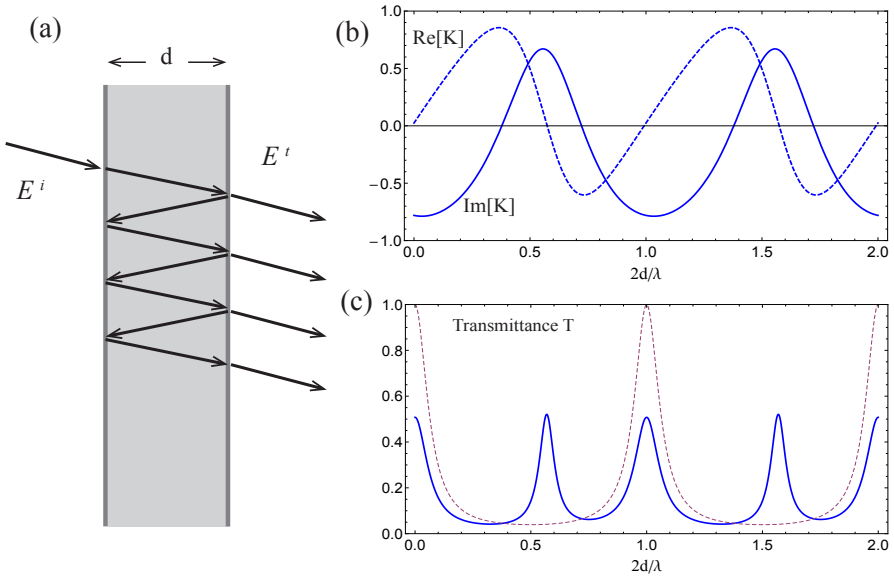

Figure 5.4: (a)Multiple reflections between the double-layer geometry(e.g. topological insulator slab, double-layer TI thin-film). (b)The real and imaginary part of the polarization coefficient (K) of the transmitted optical field as a function of topological insulator slab thickness d. (c)Transmittance T as a function of slab thickness d, the dashed line is for a pure dielectric slab. Here $\xi = 4$ in both plots.

graphene and TI thin-film by revising the linear susceptibility tensor. Due to the nature of helical Dirac fermions, the lifetime $1/\gamma$ of the topological surface states is much longer compared to the bulk states and the similar 2D Dirac fermion states in graphene, which greatly enhances the cyclotron resonance feature of the linear

optical response of topological surface layer. As a result, the slab geometry exhibits strong reflection of the incident field component that resonates with the inter-surface-Landau-level transition. For example, given a linearly polarized optical field $\vec{E} \sim (\hat{x} + \hat{y}) \exp(-i\omega t)$ incident onto doped topological insulator slab (Fermi energy is set between surface Landau level -1 and 0), when $\omega \approx \omega_c$, the right-hand circular polarized component resonates with the inter-surface-Landau-level transition $-1 \to 0$. It leads to a strong reflection of the right-hand circularly polarized component of the incident field. The resulting polarization coefficient (K^t) of the transmitted field is plotted in Fig. 5.3(c) as a function of the dimensionless quantity

$$\xi = g \cdot \frac{\omega_c}{4\gamma} \frac{e^2}{\hbar c},$$

where $g = 1$ for a topological insulator slab, and $g = 2$ for a double-layer TI thin-film, which is two topological insulator thin-films separated by a dielectric layer. When the scattering rate is small enough and ξ becomes big, only the left-hand circularly polarized component ($\sim \hat{x} - i\hat{y}$) of the incident field transmits. In addition, one can always enhance the magneto-optical properties by stacking multiple interlayer-decoupled TI thin-films[111], which further increases the surface degeneracy factor g. So we believe such a geometry based on topological surface layers possesses promising application as a polarizer.

Such a double-layer geometry with surface polarization also exhibits optical properties of a Fabry-Perot cavity. In Fig. 5.4 we show both the transmittance and polarization coefficient of the transmitted optical field as a function of the slab thickness d. We observe that when the thickness d is around $n \cdot \frac{\lambda}{2}, n = 0, 1, 2, ...$, the topological insulator slab possess strong reflection to the resonance part of the incident field. Different from a pure dielectric Fabry-Perot cavity, the topological-insulator-based

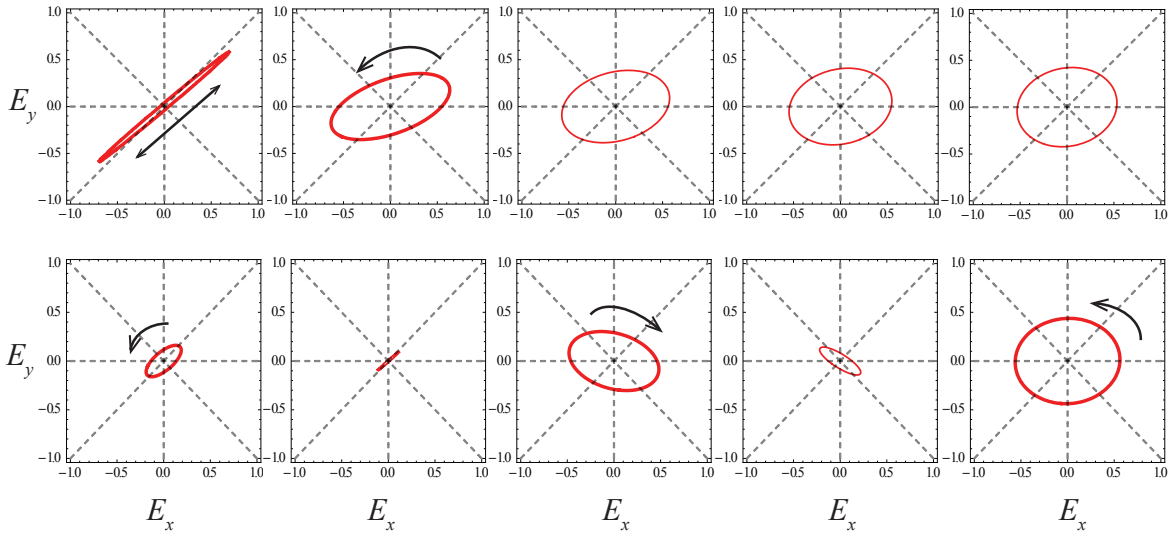

Figure 5.5: Polarization ellipse of the transmitted field. First row: from left to right, $\xi = 0.1, 1, 2, 3, 4$; d is fixed at 0.01λ. Second row: from left to right, $d = 0.1\lambda, 0.2\lambda, 0.3\lambda, 0.4\lambda, 0.5\lambda$; ξ is fixed at 4.

double-layer geometry also possesses a transmittance peak between $n\lambda$ and $(n+\frac{1}{2})\lambda$ due to the strong surface polarization, as shown in Fig. 5.4(b).

The corresponding polarization ellipse of the transmitted field is derived as

$$\left(\frac{E_y^t}{|E_y^t|}\right)^2 - 2\frac{E_y^t}{|E_y^t|}\frac{E_x^t}{|E_x^t|}\cos\delta + \left(\frac{E_x^t}{|E_x^t|}\right)^2 = \sin^2\delta, \tag{5.26}$$

where $E_y^t = \tilde{E}_y^t|_{z=\frac{d}{2}}$, $E_x^t = \tilde{E}_x^t|_{z=\frac{d}{2}}$, and δ is the phase difference between E_y^t and E_x^t. We can also rewrite the ellipse equation in terms of in-plane polarization coefficient K and transmittance T.

$$|K|^2(E_x^t)^2 - 2\mathrm{Re}[K]E_x^tE_y^t + (E_y^t)^2 = \frac{\mathrm{Im}^2[K]}{|K|^2+1}T. \tag{5.27}$$

We here list the ellipses of the transmitted field for different ξ and thickness d in

Fig. 5.5. The first row clearly shows that the transmitted optical field gradually transformed to circularly polarized light when ξ increases. The second row shows the transmitted fields at different thickness. The corresponding orientation angle θ

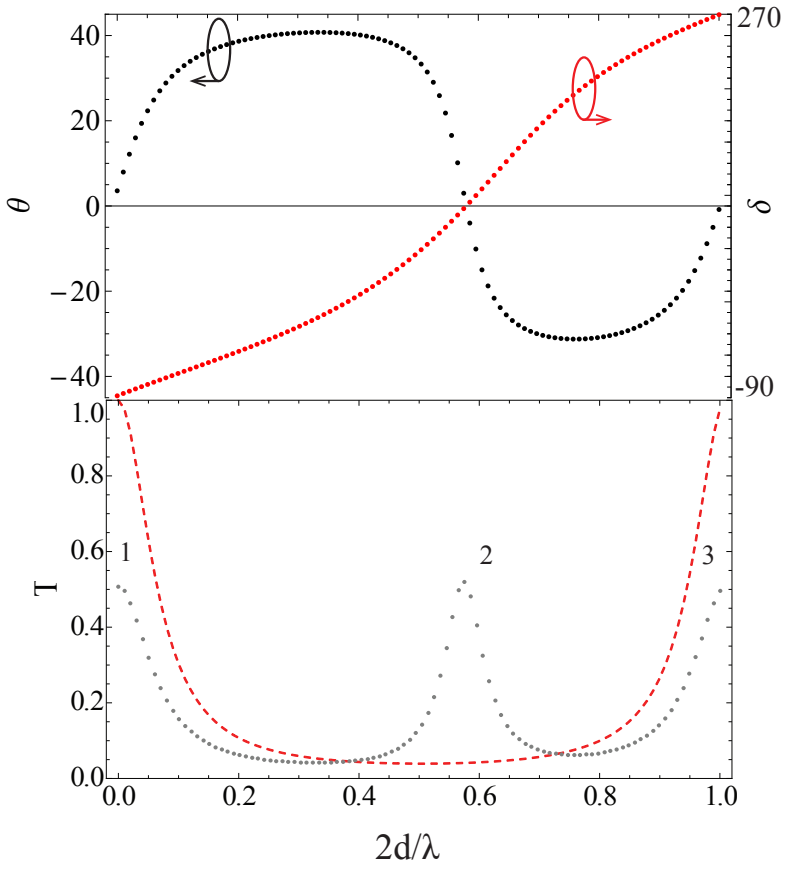

Figure 5.6: Orientation angle θ and phase-difference δ between E_y^t and E_x^t.

of the polarization ellipse is solved as

$$\tan 2\theta = \frac{2|E_x^t||E_y^t|}{|E_x^t|^2 - |E_y^t|^2} \cos\delta, \tag{5.28}$$

where θ is the angle measured from x-axis. Phase difference δ and orientation angle θ are more meaningful to explain the polarization optics of topological insulator slab as well as its Fabry-Perot properties. As shown in Fig. 5.6, we plot θ and δ as a function of d for the same physics picture described in Fig. 5.3. In each period ($n\lambda \leq d \leq (n+\frac{1}{2})\lambda$), TI slab exhibits three transmittance peaks. At each peak, the orientation angle θ is 0. The phase difference δ at peak 1 and 3 are $-\frac{\pi}{2}$, while the phase difference at peak 2 is $\frac{\pi}{2}$. In other words, when d is around $n\cdot\frac{\lambda}{2}$, the polarization component that resonates with the inter-surface-Landau-level transition exhibits a strong reflection, and only the field component with the opposite sense of polarization is able to transmit. However, interestingly, due to the strong surface polarization and the cavity property of a double-layer geometry, the transmitted field at peak 2 possesses an opposite polarization as compared to those at peak 1 and peak 3 (refer to the polarization ellipses shown in Fig. 5.5).

5.3 Nonlinear optical properties

Originating form the quasi-particle like energy dispersion near the Γ point and the unique optical selection rule, a topological insulator film has nonlinear optical properties similar to that of monolayer graphene. The nonlinear optical behavior of a thin film can be calculated following the master equations.

Bulk hole doping can manipulate Fermi level of a topological insulator below the Dirac point, which makes 4-wave-mixing between different surface Landau level possible. Here we choose a close system consists of LLs -1, 0, 1 and 2. The corresponding

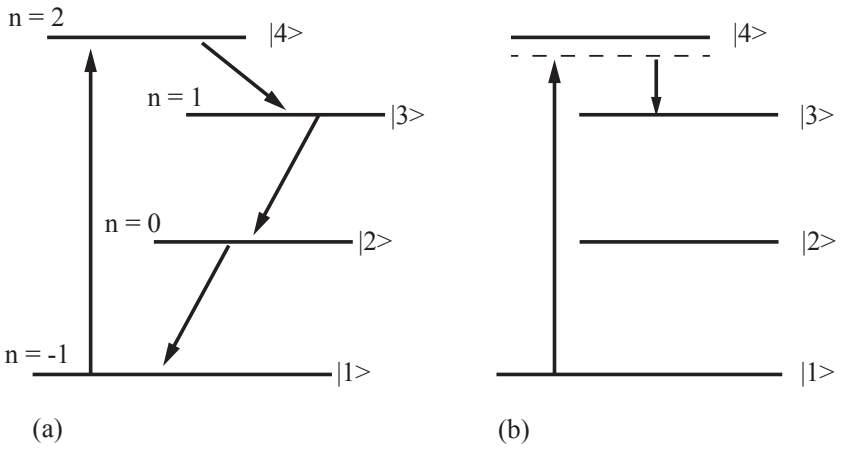

Figure 5.7: four wave mixing and stimulated raman scattering.

eigenfunctions are:

$$
\begin{aligned}
|1\rangle &= \frac{1}{\sqrt{2L}} \exp(-ik_{y_1} y) \begin{pmatrix} -i\phi_0 \\ \phi_1 \end{pmatrix}; \\
|2\rangle &= \frac{1}{\sqrt{L}} \exp(-ik_{y_2} y) \begin{pmatrix} 0 \\ -i\phi_0 \end{pmatrix}; \\
|3\rangle &= \frac{1}{\sqrt{2L}} \exp(-ik_{y_3} y) \begin{pmatrix} i\phi_0 \\ \phi_1 \end{pmatrix}; \\
|4\rangle &= \frac{1}{\sqrt{2L}} \exp(-ik_{y_4} y) \begin{pmatrix} -\phi_1 \\ i\phi_2 \end{pmatrix}. \qquad (5.29)
\end{aligned}
$$

The dipole moment matrix of the 4-level-system is given by

$$\vec{\mu} = \frac{el_c}{2}\begin{bmatrix} 0 & \hat{x}-i\hat{y} & 0 & \frac{\hat{x}+i\hat{y}}{2+\sqrt{2}} \\ \hat{x}+i\hat{y} & 0 & \hat{x}+i\hat{y} & 0 \\ 0 & \hat{x}-i\hat{y} & 0 & \frac{\hat{x}+i\hat{y}}{2-\sqrt{2}} \\ \frac{\hat{x}-i\hat{y}}{2+\sqrt{2}} & 0 & \frac{\hat{x}-i\hat{y}}{2-\sqrt{2}} & 0 \end{bmatrix} \tag{5.30}$$

Consider a strong bichromatic normally incident field

$$\vec{E} = \vec{E}_1 \exp(-i\omega_1 t) + \vec{E}_2 \exp(-i\omega_2 t) + c.c.$$

with ω_1 resonant with transition from $n = -1$ to $n = 2$ and ω_2 resonant with transition between $n = 0$ and $n = \pm 1$, where $\vec{E}_1$ has left circular polarization and $\vec{E}_2$ has linear polarization. As a result, the 4-wave-mixing interaction generates a right-circularly polarized signal field $\vec{E}_3$ with frequency $\omega_3 = \omega_1 - 2\omega_2$, as shown in Fig. 5.7. The resulting third-order nonlinear susceptibility corresponding to the characterized 4-wave-mixing is

$$\begin{aligned} \chi^{(3)}(\omega_3) &= \frac{N\mu_{43}\tilde{\mu}_{41}\tilde{\mu}^*_{32}\tilde{\mu}^*_{21}}{(i\hbar)^3\Gamma_{43}}\left(\frac{\rho_{22}-\rho_{33}}{\Gamma^*_{31}\Gamma^*_{32}} + \frac{\rho_{22}-\rho_{11}}{\Gamma^*_{31}\Gamma^*_{21}}\right. \\ &- \left.\frac{\rho_{11}-\rho_{44}}{\Gamma_{42}\Gamma_{41}} + \frac{\rho_{22}-\rho_{11}}{\Gamma_{42}\Gamma^*_{21}}\right), \end{aligned} \tag{5.31}$$

with

$$\tilde{\mu}_{mn} = \langle m|\tilde{\vec{\mu}}|n\rangle = \frac{iev_F}{\omega}\langle m|\vec{\sigma}|n\rangle, \quad \Gamma_{mn} = \gamma_{mn} + i(\omega_{mn} - \omega).$$

Here N is aerial density of states on each surface LL; $\tilde{\mu}_{mn}$ coincides with dipole moment $\vec{\mu}_{mn}$ for resonance transition; Γ_{mn} is the complex dephasing factor between surface LL m and n. For resonant incidence, the dephasing factors become real num-

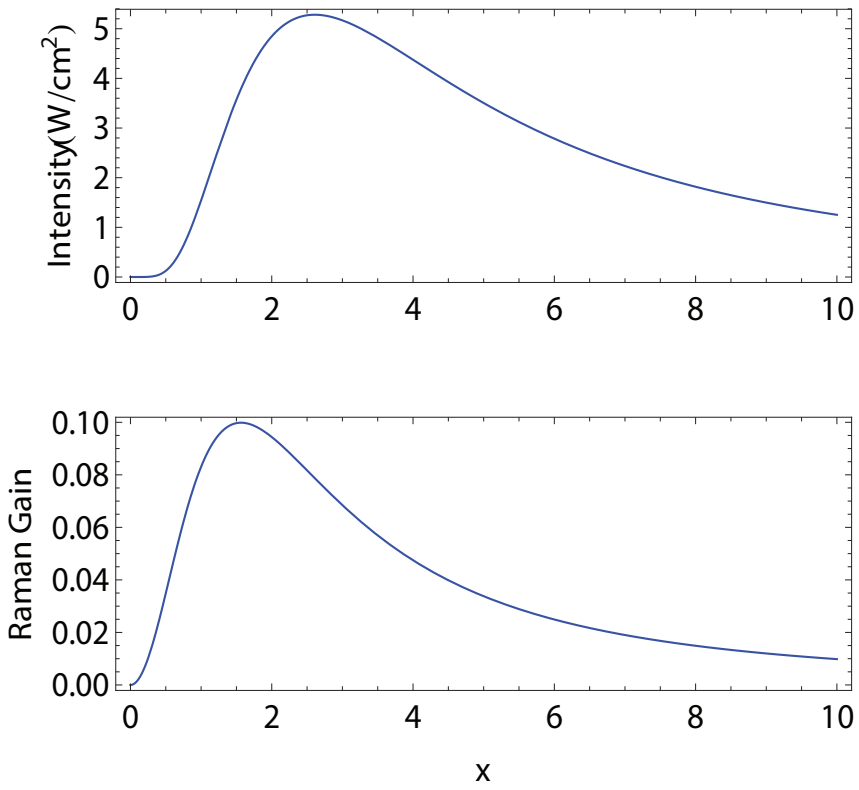

Figure 5.8: 3rd order nonlinear signal intensity and stokes raman gain. B = 1T, $\gamma = 10^{12}s^{-1}$.

bers, and we further assume all the detuning rates are the same $\Gamma_{ij} \sim \gamma = 10^{12}s^{-1}$ in the following calculation. For weak incidence, the equivalent 2D third order susceptibility for the thin film is $10^{-5}(1/B(T))$esu. When incident fields increase in intensity, the population on each level is strongly dependent on the incident intensity. As a result, third order susceptibility dramatically drops after the 4 level system gets saturated. The electric field of the generated signal can be solved together with Maxwell's equations. Neglecting the depletion of pump fields, the relation between

signal field and optical polarization is

$$\frac{\partial \vec{E}}{\partial z} = i \cdot \frac{2\pi\omega}{c} \cdot \vec{P}. \tag{5.32}$$

The resulting signal field is then given by

$$E_3 = \frac{2\pi i\omega_3}{c}\chi^{(3)}E_1(E_2^*)^2.$$

The stimulated Raman Stokes scattering of pump field E_1 into the field E_3 can also be calculated using density matrix formalism. The small signal solution of E_3 has the form $E_0 e^{gz}$, the Raman gain of the generated signal field, taking power-broadening and population inversion into account, is given by

$$\begin{aligned} g &= \frac{2\pi\omega_3 N\mu_{43}\tilde{\mu}_{43}}{\hbar c\Gamma_{43}}\left(n_{43} - \frac{|\Omega_{41}|^2}{\Gamma_{31}^*\Gamma_{41}^*}n_{41}\right) \\ &\times 1/\left(1 + |\Omega_{41}|^2/(\Gamma_{43}\Gamma_{31}^*)\right), \end{aligned} \tag{5.33}$$

Where Ω_{mn} is the corresponding Rabi frequency. The signal gain of the whole 10nm thin film can be integrated along its propagation direction. For a 10nm thick topological insulator film, the signal field is strong enhanced by stokes Raman scattering near the 2 surfaces, and the total gain of the whole film is $10^{-2} \sim 10^{-1}$ when magnetic field is 1T. The maximum gain can be realized when incident field is of the order of saturation value, and quickly drops when beyond saturation, which is clearly shown in Fig. 5.8.

6. SUMMARY

In this dissertation, we established a fully quantum mechanical density matrix formalism to study both linear and nonlinear optics in a system of massless Dirac fermions.

We presented detailed theoretical studies of the linear and nonlinear optical response of monolayer graphene in a strong magnetic field, including megneto-absorption, Faraday rotation, four-wave-mixing process and stimulated Raman scattering. We theoretically demonstrated that monolayer graphene in a strong magnetic field possesses a very high infrared optical nonlinearity due to unique properties of quantized Landau levels near the Dirac point. The nonlinearity is expected to be ultrafast, enabling reponse to THz modulation. These properties of monolayer graphene may have important implications for coherent nonlinear generation and detection in the mid-infrared and THz range. One should expect to encounter similar unusual nonlinear optical properties in 3D topological insulator materials.

Based on the highly efficient four-wave mixing process in the 2D Dirac fermion systems, we further proposed a new mechanism of generating entangled photons. We theoretical demonstrated that the extremely strong nonlinearity of graphene in combination with its peculiar properties of the Landau levels open new ways for generation of the nonclassical light states, in particular polarization-entangled photons. This parametric mechanism could also be used to control the quantum state of electrons in topological surface states.

We also found that THz surface plasmons in graphene and topological insulators can be generated with high efficiency through second-order nonlinear frequency mixing of two obliquely incident or in-plane propagating mid-IR beams over a broad

range of frequencies and angles of incidence. This process can be used for compact integrated schemes of nonlinear generation, detection and modulation of the THz light in these materials or for the manipulation of electron states by optical means.

REFERENCES

[1] Geim A K and Novoselov K S 2007 *Nature Mater.* 6, 183-191

[2] Novoselov K S et al. 2005 *Proc. Natl Acad. Sci. USA* 102, 10451-10453

[3] Berger C et al. 2004 *J. Phys. Chem. B* 108, 19912-19916

[4] Sutter P W, Flege J I and Sutter E A 2008 *Nature Mater.* 7, 406-411

[5] Emtsev K V et al. 2009 *Nature Mater.* 7, 406-411

[6] Li X, Wang X, Zhang L, Lee S and Dai H 2008 *Science* 319, 1229-1232

[7] Hernandez Y et al. 2008 *Nature Nanotech.* 3, 563-568

[8] Lotya M et al. 2008 *J. Am. Chem. Soc.* 131, 3611-3620

[9] Valles C et al. 2008 *J. Am. Chem. Soc.* 130, 15802-15804

[10] Karu A E and Beer M 1966 *J. Appl. Phys.* 37, 2179-2181

[11] Obraztsov A N, Obraztsova E A, Tyurnina A V and Zolotukhin A A 2007 *Carbon* 45, 2017-2021

[12] Kim K S et al. 2007 *Nature* 457, 706-710

[13] Reina A et al. 2009 *Nano. Lett.* 9, 30-35

[14] Castro Neto A H, Guinea F, Peres N M R, Novoselov K S and Geim A K 2009 *Rev. Mod. Phys.* 81, 109162

[15] Wallace P R 1947 *Phys. Rev.* 7, 622

[16] Katsnelson M I 2006 *Phys. Rev. B* 74, 201401

[17] Katsnelson M I and Novoselov K S 2007 *Solid State Commun.* 143, 3

[18] Novoselov K S et al. 2005 *Nature* 438, 197

[19] Zhang Y, Tan T W, Stormer H L and Kim P 2005 *Nature* 438, 201

[20] Novoselov K S et al. 2007 *Science* 315, 1379

[21] Novoselov K S et al. 2004 *Science* 306, 666

[22] Nair R R et al. 2008 *Science* 320, 1308

[23] Stoehr R J, Kolesov R, Pflaum J and Wrachtrup J 2010 *Phys. Rev. B* 82, 121408

[24] Liu C H, Mak K F, Shan J and Heinz T F 2010 *Phys. Rev. Lett.* 105, 127404

[25] Hasan T et al. 2009 *Adv. Mater.* 21, 3874-3899

[26] Sun Z et al. 2010 *ACS Nano* 4, 803-810

[27] Bonaccorso F, Sun Z, Hasan T and Ferrari A C 2010 *Nature Photon.* 10, 1038

[28] Bae S et al. 2010 *Nature Nanotech.* 4, 574-578

[29] Xia F N et al 2009 *Nano Lett.* 9, 1039-1044

[30] Xia F N, Mueller T, Lin Y M, Valdes-Garcia A and Avouris P 2009 *Nature Nanotech.* 4, 839-843

[31] Hasan M Z andKane C L 2010 *Rev. Mod. Phys.* 82, 3045-3067

[32] Kane C L and Mele E J 2005 *Phys. Rev. Lett.* 95, 226801

[33] Kane C L and Mele E J 2005 *Phys. Rev. Lett.* 95, 146802

[34] Fu L and Kane C L 2007 *Phys. Rev. B* 76, 045302

[35] Bernevig B A, Hughes T A and Zhang S C 2006 *science* 314, 1757

[36] Xia Y et al. 2009 *Nature Phys.* 5, 398

[37] Chen Y L et al. 2009 *Science* 325, 178

[38] Hsieh D et al. 2009 *Phys. Rev. Lett.* 103, 146401

[39] Liu C X, Qi X L, Zhang H J, Dai X, Fang Z and Zhang S C 2010 *Phys. Rev. B* 82, 045122

[40] Zhang H J, Liu C X, Qi X L, Dai X, Fang Z and Zhang S C 2009 *Nat. Phys.* 5, 438

[41] Zhang X, Wang J and Zhang S C 2010 *Phys. Rev. B* 82, 245107

[42] Tse W-K and MacDonald A H 2010 *Phys. Rev. B* 82, 161104(R)

[43] Sobota J A et al. 2012 *Phys. Rev. Lett.* 108, 117403

[44] Schafgans A A, Post K W, Taskin A A, Ando Yoichi, Qi X L, Chapler B C and Basov D N 2012 *Phys. Rev. B* 85, 195440

[45] Xue Q K et al. 2010 *Phys. Rev. Lett.* 105, 076801

[46] Shan W Y, Lu H Z and Shen S Q 2010 *New Journal of Physics* 12, 043048

[47] Lu H Z, Shan W Y, Yao W, Niu Q and Shen S Q 2010 *Phys. Rev. B* 81, 115407

[48] Yen T J et al. 2004 *Science* 303, 1494-1496

[49] Pendry J B, Holden A J, Stewart W J and Youngs I 1996 Phys. Rev. Lett. 76, 4773-4776

[50] Chen H T et al. 2006 *Nature* 444, 597-600

[51] Grigorenko A N, Polini M and Novoselov K S 2012 *Nature Phot.* 6, 749

[52] Tredicucci A and Vitiello M 2014 *IEEE Sel. Topics Quant. El.* 20, 8500109

[53] Jablan M, Buljan H and Soljacic M 2009 *Phys. Rev. B* 80, 245435

[54] Efimkin D K, Lozovik Y E and Sokolik A A 2012 *Nanoscale Research Lett.* 7, 163

[55] Allen S J, Tsui D C and Logan R A 1977 *Phys. Rev. Lett.* 38, 980-983

[56] Batke E, Heitmann D and Tu C W 1986 *Phys. Rev. B* 34, 6951-6960

[57] Ashkan Vakil and Engheta N 2011 Preprint at http://arXiv.org/abs/1101.3585

[58] Rana F 2008 *IEEE Trans Nanotechnol.* 7 91-99

[59] Ryzhii M and Ryzhii V 2007 *Jpn. J. Appl. Phys.* 2 46, L151-153

[60] Abergel D S L and Fal'ko V I 2007 *Phys. Rev. B* 75, 155430

[61] Hwang E H, Sensarma R and Das Sarma S 2010 *Phys. Rev. B* 82, 195406

[62] Hwang E H and Das Sarma S 2009 *Phys. Rev. B* 80, 205405

[63] L. Ju, B. Geng, J. Horng, C. Girit, M. Martin, et al. Nature Nanotechn. 6, 630 (2011).

[64] Zhang Y et al. 2010 *Nature Phys.* 6, 584

[65] Profumo R E V, Asgari R, Polini M and MacDonald A H 2012 *Phys. Rev. B* 85, 085443

[66] Sadowski M L, Martinez G, Potemski M, Berger C and de Heer W A 2006 *Phys. Rev. Lett.* 97, 266405

[67] Yao X and Belyanin A 2012 *Phys. Rev. Lett.* 108, 255503

[68] Yao X and Belyanin A 2013 *J. Phys.: Condens. Matter* 25, 054203

[69] Booshehri L G et al. 2012 *Phys. Rev. B* 85, 205407

[70] Orlita M et al. 2008 *Phys. Rev. Lett.* 101, 267601

[71] Orlita M et al. 2009 *Phys. Rev. Lett.* 102, 166401

[72] Crassee I et al. 2011 *Nature Phys.* 7, 48

[73] Ando T 2005 *J. Phys. Soc. Jpn.* 74, 777

[74] Zheng Y and Ando T 2002 *Phys. Rev. B* 65, 245420

[75] Ando T 2007 *J. Phys. Soc. Jpn.* 76, 024712

[76] Jiang Z, Henriksen E A, Tung L C, Wang Y, Schwartz M E, Han M Y, Kim P and Stormer H L 2007 *Phys. Rev. Lett.* 98, 197403

[77] Mikhailov S A and Ziegler K 2008 *J. Phys.:Condens. Matter* 20, 384204

[78] Mikhailov S A 2009 *Phys. Rev. B* 79, 241309(R)

[79] Hendry E, Hale P J, Moger J, Savchenko A K and Mikhailov S A 2010 *Phys. Rev. Lett.* 105, 097401

[80] Gurnick M K and De Temple T A 1983 *IEEE J. Quantum Electron.* 19, 791

[81] Sirtori C, Capasso F, Sivco D, Chu S N G and Cho A Y 1991 *Appl. Phys. Lett.* 59, 2302 (1991).

[82] Owschimikow N, Gmachl C, Belyanin A, Kocharovsky V, Sivco D L, Colombelli R, Capasso F and Cho A Y 2003 *Phys. Rev. Lett.* 90, 043902

[83] Malis O, Belyanin A, Sivco D L, Chen J, Sergent A M, Gmachl C and Cho A Y 2004 *Electron. Lett.* 40, 1586

[84] Mosely T S, Belyanin A, Gmachl C, Sivco D L, Peabody M L and Cho A Y 2004 *Optics Express* 12, 2972

[85] Troccoli M, Belyanin A, Capasso F, Cubukcu E, Sivco D L and Cho A Y 2005 *Nature*, 433, 845

[86] Belyanin A, Capasso F, and Troccoli M, Raman injection and inversionless intersubband lasers, Chapter 6, in: *Intersubband Transitions in Quantum Structures*, ed. by R. Paiella, 2006 McGraw-Hill, 181-236

[87] Kocharovskaya O, Rostovtsev Yu V and Imamoglu A 1998 *Phys. Rev. A* 58, 649654

[88] Liu H C et al. 2001 *Appl. Phys. Lett.* 78, 3580 (2001).

[89] Scheinert M, Sigg H, Tsujino S, Giovannini M and Faist J 2007 *Appl. Phys. Lett.* 91, 131108

[90] Kwiat P G, Mattle K, Weinfurter H, Zeilinger A, Sergienko A V and Shih Y 1995 *Phys. Rev. Lett.* 75, 4337

[91] Yin J, Ren J, Lu H, Cao Y, Yong H, et al. 2012 *Nature* 488, 185

[92] Fan J, Migdall A and Wang L 2007 *Opt. Photon. News* March 2007, 26-33

[93] Stevenson R M, Young R J, Atkinson P, Cooper K, Ritchie D A and Shields A J 2006 *Nature* 439, 179-182

[94] Mohan A, Felici M, Gallo P, Dwir B, Rudra A, et al. 2010 *Nature Phot.* 4, 302

[95] Dousse A, Suffczynski J, Beveratos A, Krebs O, Lemaitre A, et al. 2010 *Nature* 466, 217

[96] Tokman M, Yao X, and Belyanin A 2013 *Phys. Rev. Lett.* 110, 077404

[97] Landau L D and Lifshitz E M 1980 *Statistical Physics, Part 1.* Butterworth-Heinemann, Oxford

[98] Rytov S M, Kravtsov, Yu A and Tatarskii V I 1989 *Principles of Statistical Radiophysics 3: Elements of random fields,* Springer-Verlag, Berlin

[99] Fain V M and Khanin Ya I 1969 *Quantum electronics, Vol. 1.* The MIT Press, Cambridge, MA

[100] Lukin M D et al. 1997 *Phys. Rev. Lett.* 79, 2959

[101] Xiong H, Scully M O and Zubairy M S 2005 *Phys. Rev. Lett.* 94, 023601

[102] Qamar S, Al-Amri M and Zubairy M S 2009 *Phys. Rev. A* 79, 013831

[103] Yao X, Tokman M, and Belyanin A 2014 *Phys. Rev. Lett.* 112, 055501

[104] Mikhailov S A 2011 *Phys. Rev. B* 84, 045432

[105] Glazov M M 2011 *JETP Lett.* 93, 366

[106] Belkin M, Capasso F, Belyanin A, Sivco D L, Cho A Y, Oakley D C, Vineis C J, and Turner G W 2007 *Nature Photonics* 1, 288

[107] Wang X, Cheng Z, Hu K, Tsang H K, and Xu J B 2013 *Nature Phot.* 7, 888

[108] Hanaguri T, Igarashi K, Kawamura M, Takagi H and Sasagawa T 2010 *Phys. Rev. B* 82, 081305

[109] Cheng P et al. 2010 *Phys. Rev. Lett.* 105, 076801

[110] Jiang Y et al. 2012 *Phys. Rev. Lett.* 108, 016401

[111] Goyal V, Teweldebrhan D and Balandin A A 2010 *Appl. Phys. Lett.* 97, 133117